Gas-Solid Surface Interaction with Reactive and Less Reactive Gases: A Near Ambient Pressure Photoelectron Spectroscopy Study

Thesis Submitted to

Academy of Scientific and Innovative Research

For the Award of the Degree of

Doctor of Philosophy in Chemical Science

by

Manoj Kumar Ghosalya

AcSIR Reg. No: 10CC13A26014

Under the Guidance of

Dr. Chinnakonda S. Gopinath

Catalysis Division

CSIR- National Chemical Laboratory

Pune, India.

सीएसआयआर–राष्ट्रीय रासायनिक प्रयोगशाला
(वैज्ञानिक तथा औद्योगिक अनुसंधान परिषद)
डॉ. होमी भाभा मार्ग, पुणे – 411 008. भारत
CSIR-NATIONAL CHEMICAL LABORATORY
(Council of Scientific & Industrial Research)
Dr. Homi Bhabha Road, Pune - 411 008, India

डॉ. चिन्नाकोंडा एस. गोपीनाथ
अध्यक्ष एवं मुख्य वैज्ञानिक
उत्प्रेरक एवं अकार्बनिक रसायन प्रभाग
एवं प्राध्यापक, एसीएसआईआर

Dr. Chinnakonda S. Gopinath
Chairman & Chief Scientist,
Catalysis & Inorganic Chemistry Division
& Professor at AcSIR

CERTIFICATE

This is to certify that the work incorporated in this Ph.D. thesis entitled ***Gas-Solid Surface Interaction with Reactive and Less Reactive Gases: A Near Ambient Pressure Photoelectron Spectroscopy Study*** submitted by **Mr. Manoj Kumar Ghosalya** to the Academy of Scientific and Innovative Research (AcSIR) in fulfilment of the requirements for the award of the Degree of ***Doctor of Philosophy*** in ***Chemical Sciences***, embodies original research work under my supervision. I further certify that this work has not been submitted to any other University or Institution in part or full for the award of any degree or diploma. Research material obtained from other sources has been duly acknowledged in the thesis. Any text, illustration, table etc., used in the thesis from other sources, have been duly cited and acknowledged.

Manoj Kumar Ghosalya
(Student)
Date : November 12, 2018

C. S. Gopinath 12/11/2018

Dr. Chinnakonda S. Gopinath
Research Supervisor
Chief Scientist
Catalysis Division
CSIR-NCL, Pune

Tel. : 91-20-2590 2009 / 2590 2043
Fax : 91-20-2590 2633

E-mail : cs.gopinath@ncl.res.in
Web : www.ncl-india.org
http://nclwebapps.ncl.res.in/csgopinath/

CERTIFICATE

I, Mr. Manoj Kumar Ghosalya, hereby declare that the work incorporated in the thesis entitled ***"Gas-Solid Surface Interaction with Reactive and Less Reactive Gases: A Near Ambient Pressure Photoelectron Spectroscopy Study"*** submitted by me to Academy of Scientific and Innovative Research (AcSIR), in fulfilment of the requirements for the award of the Degree of ***Doctor of Philosophy*** in ***Chemical Sciences***, is the result of investigation carried out by me in Catalysis Division, CSIR- National Chemical Laboratory, Pune under the supervision of Dr. Chinnakonda S. Gopinath and has not been submitted to this or any other Institution for the award of any other degree or Diploma. Any text, illustration, table etc., used in the thesis from other sources, have been duly cited and acknowledged

Date-12/11/2018

Manoj Kumar Ghosalya
Research Student,
Catalysis Division
CSIR- National Chemical Laboratory,
Pune

Dedicated To My Parents

Acknowledgements

I wish my life be like this throughout, full of joy, excitement and the bunch of interesting people around. I got to know the different facets of cultures and thought processes along with the scientific, social and personal developments and all this from the individuals close to me. The acknowledgement is not something about to write or say, rather is about to live by, still am trying to express my gratitude in the form of words for the personalities who were involved in my transformation from a Master in Chemistry to a Ph.D. Research Scholar.

The most important individual who has guided me through the most challenging yet very enthralling phases of my doctorate is my teacher, Dr. C. S. Gopinath. I consider myself to be extremely fortunate to have him as my research guide. He has a great influence in my scientific and personal accomplishments. The concepts like work presentation and Thursday evening seminars provided me the opportunities to discuss and learn a number of catalysis and photoelectron spectroscopy problems. His constant encouragement to keep perform all the time, more importantly when the thing were little chaotic, has always been a source of motivation to work consistently. His knowledge of the subject and experience has been the foundation of my research carrier; without his supervision and constant help this thesis would not have been possible and he will be the source of excitement to look for the new ideas, forever.

I would like to sincerely thank my doctoral advisory committee members Drs. Guruswamy Kumaraswamy, Debashree Ghosh, C. P. Vinod, and M. Karthikeyan for their constant help and support.

I am grateful to UGC, for awarding the research fellowship and Prof. A. K. Nangia, Director, and Dr. S. Pal, Former Director. CSIR- National Chemical Laboratory for providing me the infrastructure and advanced research facilities, and to submit this works in the form of a thesis for the PhD degree. I am also thankful to the Academy of Scientific and Innovative Research (AcSIR) for giving me a chance to reach one of the milestones in my life.

I express my heartfelt thanks to Drs. D Srinivas, (former chairman, catalysis division) and A. P. Singh (former Chairman, Catalysis Division), and Dr. C. S. Gopinath (Chairman, Catalysis Division) for their extended support and providing the divisional facility. I would also like to offer my sincere admiration to Drs. C. P. Vinod, T. Raja, for their enthusiastic

encouragement and support. I thank all the technical staff of CSIR-NCL for their assistance on various occasions. I am also thankful to Mr. Purushothaman and Mr. Madhu for their kind help. I am also thankful to technical team, PREVAC, Poland for their technical help provided from time to time. Special thanks to my teacher(s) who guided me in my school and graduation because of whom I learnt a lot.

I owe the expression of gratitude towards my lab-mates, Drs. Edwin S. Gnanakumar, Naresh, Sadhu Kolekar, Ashwin A. Melvin, Sanjay Negi,. Kanak Roy, Devaraji, Anjani Dubey, Kshirodra Patra, Rajambal, Pradnya A. Bharad, Ruchi Jain, Mr. Prabhakar Reddy, Mr. Nitin Mhamane, Mr. Ravi Ranjan, Mr. Himanshu Vajpai, Mr. Indrajeet Chauhan, Ms. Kranti Salgaonkar, Ms. Shreya, Ms. Bela, Mr. Madhusudan for introducing me to the research aspects of science through lot of discussions. I have learned a number of catalysis and spectroscopy concepts, both experimental as well theoretical, either in the group meetings or in general in the lab. I will enjoy the unforgettable lab trips we have gone together. It is a great privilege to express my gratitude to Dr. Kanak Roy. He is the person who has been instrumental in my research carrier and taught me the NAPPES system handling and operation.

Apart from the scientific work, there is a life called friends, the most beautiful gift of my life in Pune. It is the friends like Drs. Vijay, Amit, Sandeep, and Kavita Gupta the reason for I want to stay here, forever. These four are the meaning of friendship for me and I am going to miss each of them. I will cherish all those beautiful moments I have spent with my friends, Dr. Dharmesh, Bhanu Pratap, Dr. Pradeep, Dr. Anup, Dr. Sandip, Dr Swechchha, Ulhas, Dr. Bhawana, Dr. Vinita, Dr. Preeti Jain and many others, throughout my life.

My heartfelt thanks and appreciation to my parents for their unending support and sacrifices they have made in raising me to this level. I would also specially thanks to my wife Kavita Gared for her love and care that she had showered upon me in each and every moment of life. I want to acknowledge my brother Mr. Sandeep Choudhary and Sisters, Ms. Sushila and Urmila, for their love and care.

Manoj K. Ghosalya

Contents

List of Abbreviations

UHV	Ultra-High Vacuum
MBI	Molecular Beam Instrument
NAPPES	Near-Ambient Pressure Photoelectron Spectroscopy
NEXAFS	Near Edge X-ray Absorption Fine Structure
NAP-XPS	Near-Ambient Pressure X-ray Photoelectron Spectroscopy
NAP-UPS	Near-Ambient Pressure Ultraviolet Photoelectron Spectroscopy
STM	Scanning Tunneling Microscopy
TPD	Temperature Programmed Desorption
BE	Binding Energy
KE	Kinetic Energy
UV	Ultra-Violet
QMS	Quadrupole Mass Spectrometer
VB	Valence Band
RT	Room Temperature
ELR	Electrostatic lens region
EEA	Electron Energy Analyzer
FWHM	Full Width Half Maximum
1,3-BD	1,3-Butadiene
ODH	Oxidative Dehydrogenation
IMFP	Inelastic Mean Free Path

List of Symbols

θ_O	Oxygen Coverage
ϕ	Work Function
h	Plank Constant
υ	Frequency
E_F	Fermi Energy
σ	Photoionization Cross Section

List of Figure

Preface

Chapter 1 and 2, a brief introduction role of surface science, photoelectron spectroscopy and gas solid interaction in catalysis has been given. Photoelectron spectroscopy is a versatile technique that can be advantageously used for characterization of a number of surface properties of the solid surface and interfaces, like chemical composition, oxidation state, element mapping, solid-gas interactions etc. Conventionally, the photoelectron spectroscopy is an ultra-high vacuum technique. However, the photoelectrons cannot reach the detector due to inelastic collision with gas-phase molecules at high-pressure ($>10^{-5}$ mbar) conditions. This obstacle has been overcome in the development of photoelectron spectrometers which can function at near ambient pressures. A new term ambient pressure (AP) or near ambient pressure (NAP) or high pressure (HP) has been introduced with photoelectron spectroscopy (PES) to distinguish it from the traditional UHV set ups. The NAP-PES can operate at near ambient pressure, by using the sophisticated electron energy analyzer and differentially pumped electro static lenses. Thus the NAP-PES, can bridge the "pressure gap" between the real world and ideal surface science studies. This thesis mainly focused on different studies to bridge the pressure gap between a real-world condition where the actual surface reaction happens and ideal surface science condition.

All experiments are carried out in a custom built laboratory ambient pressure photoelectron spectrophotometer unit installed in our laboratory at CSIR-National Chemical Laboratory, Pune. The system is equipped with the differentially pumped Scienta R3000HP analyzer. Two sets of differential pumping are available in the electrostatic lens regime (ELR), and the third one is available in the electron energy analyzer (EEA). The distance between sample surface and aperture (of the cone, R = 0.4 mm) attached to ELR was maintained at 1.2 mm for all of the experiments reported. The main advantage with this design is a fast decrease in pressure with a steep pressure gradient from the aperture to the EEA. It is to be underscored that the first differential pumping records 2×10^{-4} mbar when the analysis chamber is at 1 mbar. This helps to minimize the inelastic scattering of low KE electrons. Further, R3000HP employs the advanced concept of electron converging with an aperture free ELR. In contrast to the conventional ELR, electrostatic voltages in the R3000HP model analyzer are applied in such a way that they converge all the electrons. The system also equipped Al-Mg dual anode, Al- monochromatic X-ray source, differentially pumped

discharge lamp to generate He I and He II UV radiation source The polycrystalline foils (Ni, Co, Si, Ag, Au, 99.999 pure) which are used in the experiments are purchased from MaTeck, Germany. These foils are cleaned by the several cycles of Ar sputtering and annealing in UHV up to 1000 K. A series of sputter-anneal cycles produced clean metal foil surfaces which is confirmed by the XPS as well as UVPES.

In chapter 3a, Silver valence band was probed by PES at near ambient pressure of oxygen (up to 0.2 mbar) with He I radiation. Three distinct regimes have been identified in silver-oxygen interaction between 300 and 500 K, which are, (a) oxygen chemisorption between ambient and 390 K, (b) O-diffusion into the subsurface layers of Ag from 390 to 450 K, and (c) formation of metastable oxide on the silver surface above 450 K; the latter two regimes are dynamic in nature.. The trend in oxygen coverage on Ag 390 K and above 475 K is similar, but it decreases to the lowest in between 390 and 450 K, in the presence of large excess of molecular oxygen. Interaction with oxygen changes the work function of Ag from 4.95 (≤390 K) to 5.30 eV (400-450 K), and then to 5.7 eV (≥450 K). It is attributed to oxygen diffusion into the subsurface layers of Ag between 400 and 450 K and plays a key role for ethylene epoxidation reaction on Ag surfaces. Subsurface oxygen influences in two significant ways; it converts the Ag surface from metallic to electron deficient in nature, and facilitates the formation of space charge layer above the Ag surface. Oxygen when adsorbed on this electron deficient Ag surface, acts as electrophilic oxygen. The electrophilic oxygen can insert into the C=C double bond of an alkene, and hence forms an epoxide. Above 450 K, oxygen binds strongly and acts as nucleophilic oxygen. The nucleophilic oxygen favors complete combustion of alkene to carbon dioxide. Changes in the Ag-oxygen system are dynamic. The metallic surface reappears if oxygen supply is removed above 400 K. This emphasizes in situ and operando investigations are essential to understand the active structure of a catalyst.

In chapter 3b, we have synthesized 5 wt % Fe_2O_3/support (support=Al_2O_3, CeO_2, MgO, ZSM-5 and Nb_2O_5) catalysts by wet impregnation method. The synthesized catalysts subjected to different physico- chemical characterization techniques to understand the structure and morphology of the catalysts. These catalysts were screened for butane oxidative dehydrogenation (ODH) reaction in fixed bed reactor at different temperature between (450°C to 600°C) with varying butane: oxygen ratio (1:1, 1:0.5 and 1:0.25). Among all these catalyst

Fe_2O_3/Al_2O_3 shows best activity in terms of 1,3-butadiene yield (higher selectivity towards 1,3-butadiene) at all different temperatures. In order to understand the active site of the compared the results with another average catalyst i.e., Fe_2O_3/Nb_2O_5. The catalyst was screened at 0.2 mbar pressure (Argon: Butane: Oxygen is 2:1:0.5 respectively) under in situ condition from 298 to 500 K. We have concluded that the Fe on the Al_2O_3 support reduced to Fe^{+2} from Fe^{+3}, whereas Fe on the Nb_2O_5 support remains in Fe^{+3} states and the reduced Fe^{+2} is responsible for the higher selectivity towards 1,3-butadiene

Chapter 4 shows Valence band and core level photoelectron spectral measurements at near-ambient pressures (up to 0.5 mbar) were made in the presence of molecular oxygen to explore the various stages of silicon oxidation. Dangling bonds feature observed in NAP-UPS on clean Si-surfaces decreases due to adsorption of molecular oxygen between ambient temperature and up to 400 K at 0.1 mbar O_2 pressure. The adsorption of oxygen on dangling bonds seems to be localized as islands and the same reflects as heterogeneous surface and responsible for the broadening in the oxygen gas phase vibrational features. This is further supported by an increase in the work function and can be correlated with the presence of Höfer (molecular) precursor. When the temperature increased to 500 K, molecular precursor species dissociates to –Si=O species and further supported by the change in the work function as well as by the oxidized silicon species from Si 2p core level. At 600 K the –Si=O species dissociates to form a uniform 2D oxide layer on the silicon surface, which is characterized by the sharp vibration features of gas-phase oxygen molecules. This layer is also quite stable up 800 K and without any further oxidation in bulk. However, when the temperature increased to 850 K at 0.2 mbar oxygen pressure, bulk Si oxidation begins and the work function increases drastically by 1 eV. An angle-dependent Si 2p core level spectra recorded map out the presence of all possible oxidation states (elemental Si^0 to Si^{4+}) from bulk to the surface. A continuous change in work function and electronic states observed due to gas-solid (O_2-Si) interaction indicates the implications of heterogeneous catalysis and electrochemistry.

In chapter 5 the gas phase vibrational spectra of reactive and inert gases have been studied by the in situ ultraviolet photoelectron spectroscopy up to 0.3 mbar. Results obtained is divided into two parts and discussed. In the first part, we have studied the molecular photoelectron spectra of monoatomic Argon gas and some homonuclear diatomic molecular gases like H_2, O_2, and N_2 by using NAPUPS and the effect of pressure on their energy

position. In this study, we have demonstrated that NAPUPS can be an essential tool to determine the gaseous composition and their electronic configuration. In the second part, we have studied the influence of surface nature on the binding energy position and pattern of the vibrational features of Nitrogen and Argon gas. It has been observed that with changing the electronic nature of the surface, the binding energy of vibrational spectra also changes which reflects the change in the work function of the material. Further, if the solid surface undergoes any chemical/electronic changes due to gas-solid interaction, such as oxidation, the work function of the surface changes again and underscores the identification of in-situ changes. Therefore, the change in the binding energy of the gas phase can be used to determine the actual work function change of material during the chemical reaction.

List of Publications (From PhD Thesis)

1. Ghosalya, M. K.; Jain, R.; Reddy, K. P.; Gopinath, C. S., Silicon Oxidation by NAPPES: From Dangling Bonds to Oxygen Islands to 2D SiO x Layer to the Onset of Bulk SiO2 Formation. *The J. Phys. Chem. C* 2018, *122*, 4331-4338.

2. Ghosalya, M. K.; Reddy, K. P.; Jain, R.; Roy, K.; Gopinath, C. S., Subtle Interaction between Ag and O_2: A Near Ambient Pressure UV Photoelectron Spectroscopy (NAP-UPS) Investigations. *J. Chem. Sci.* 2018, 130, 30

3. Ghosalya,M. K.; Reddy, K. P.; Mhamane, N. B.; Gopinath, C. S., Gas-Solid Interactions with Reactive and Not-So-Reactive Gas Molecules: Near Ambient Pressure Ultraviolet Photoelectron Spectral Studies**.** *Submitted to J. Phys. Chem.*

List of Publications (From Collaboration)

4. Reddy, K. P.; Mhamane, N. B.; Ghosalya, M. K.; Gopinath, C. S., Mapping Valence Band and Interface Electronic Structure Changes during Oxidation of Mo to MoO_3 via MoO_2 and MoO_3 Reduction to MoO_2: A NAPPES Study. *J. Phys. Chem.* **2018**.

5. Reddy, K. P.; Jain, R.; Ghosalya, M. K.; Gopinath, C. S., Metallic Cobalt to Spinel Co_3O_4 Electronic Structure Evolution by Near-Ambient Pressure Photoelectron Spectroscopy. *J. Phys. Chem. C* 2017, *121*, 21472-21481

6. Jain, R.; Reddy, K. P.; Ghosalya, M. K.; Gopinath, C. S., Water Mediated Deactivation of Co_3O_4 Naonrods Catalyst for CO Oxidation and Resumption of Activity at and Above 373 K: Electronic Structural Aspects by NAPPES. *J. Phys. Chem. C* 2017, *121*, 20296-20305.

7. Das, S.; Bhattacharjee, G.; Satpati, B.; Kumar, M.; Deka, S.; Ghosalya, M. K.; Gopinath, C. S.; Bala, T., Deposition of Au nanoparticles inside porous CeO_2 nanocubes using Langmuir–Blodgett technique. *New J. Chem*., 2018 42, 1379-138

8. Dalapati, R.; Sakthivel, B.; Ghosalya, M. K.; Dhakshinamoorthy, A.; Biswas, S., A cerium-based metal–organic framework having inherent oxidase-like activity applicable for colorimetric sensing of biothiols and aerobic oxidation of thiols. *CrystEngComm* 2017, *19*, 5915-5925.

9. Das, S.; Bordoloi, A.; Ghosalya, M. K.; Gopinath, C. S.; Bala, T., Facile synthesis of Al_2O_3-Pt nanocomposite and its catalytic activity. *Mater. Res. Exp.* 2017, *4*, 115002

10. Roy, K.; Jain, R.; Ghosalya, M. K.; Reddy, K. P.; Gopinath, C. S., Three-way catalytic converter reactions aspects at near-ambient temperatures on modified Pd-surfaces *C R Chim.* 2016, *19* (10), 1363-1369

11. Jain, R.; Dubey, A.; Ghosalya, M. K.; Gopinath, C. S., Gas–solid interaction of H 2–Ce 0.95 Zr 0.05 O 2: new insights into surface participation in heterogeneous catalysis. *Catal. Sci. Tech.* 2016, *6*, 1746-1756

12. Das, S.; Satpati, B.; Chauhan, H.; Deka, S.; Ghosalya, M. K.; Gopinath, C. S.; Bala, T., Seeding of Au on CdSe/CdS nanoplates using Langmuir–Blodgett technique. *RSC Adv* 2016, *6* (18), 14658-14665

Chapter 1

Introduction

1.1 Surface Science in Recent Times

Surface science is perhaps one of the most interdisciplinary area of modern science. The surface and interface can be defined as the boundary between a material and its environment and the surface influence the environment; in turn, environment also influences the surface and induces electronic, physical and/or chemical changes. The surface science and related fundamental studies played a very important role in developing advanced technologies, to produce valuable chemical/fuel and help to improve the application process. The surface atoms have different electronic and chemical environment than the atoms from the bulk. As a consequence of this different nature, the surface exhibits the distinct physical and chemical properties than the rest of bulk matter. These properties make the surface ideal medium for the chemical, physical and biological process. The modern surface science is about understanding the surface chemical process at the molecular level and possibly regulates them. Importance of surface science in modern science has been recognized in the last few decades and simultaneously various surface science techniques have been developed, and that led to the advancement in understanding of surface phenomena under various conditions, particularly at or closer to the application conditions. It is to be emphasized that the last 2-3 decades witnessed quite an impressive growth in surface analytical techniques that works at near-ambient pressure, ambient pressure (or even high pressure) conditions. These enabled researchers world-wide to explore the surface dependent phenomena at realistic conditions or closer to that. This was not possible with conventional high vacuum techniques, such as photoelectron spectroscopy, just two decades ago. The understanding of the surface chemistry at the molecular level under working condition of the material provides the foundation for the development of many industrial technologies including heterogeneous catalysis for fuels and chemicals,[2] advanced semiconductor devices[3,] and biomedical devices.[4] In this perspective, several applications of surface chemistry is expected to have a tremendous economic impact on our society. The technological advancement, in turn, necessitates the further development of new surface characterization technique with higher spatial, temporal and energy resolution. Over the time there is a lot of advancement has taken place in the surface science studies and developed new *in situ* spectroscopy and microscopy techniques that help to explore the

material at atomic and molecular level structure, electronic and compositional and thermodynamic properties of surfaces. These advancements are represented in Figure 1.1.

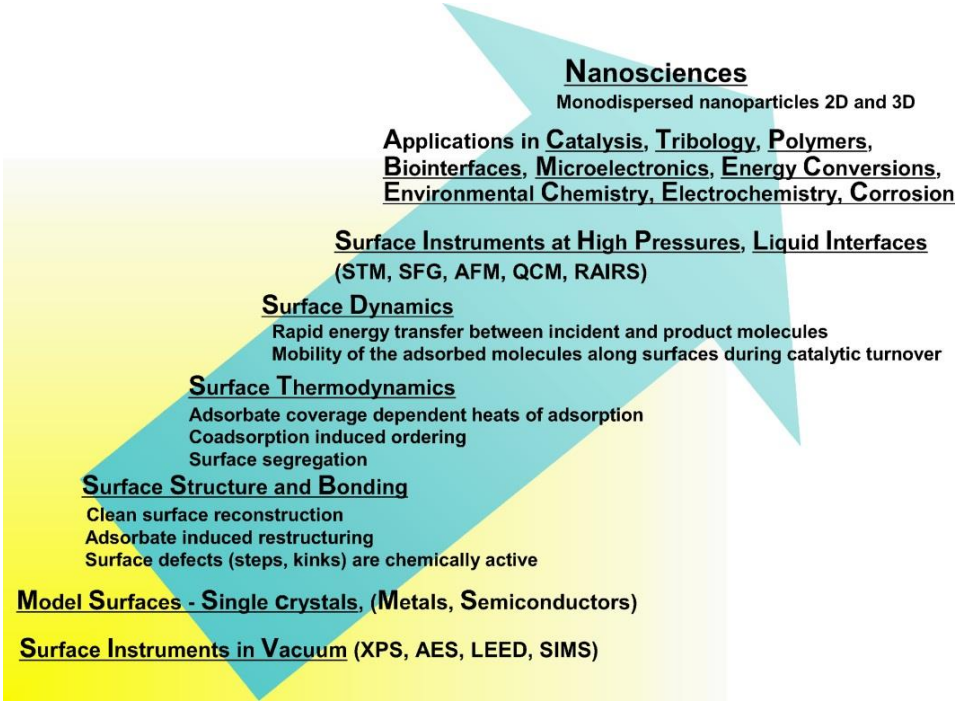

Figure 1.1: Evolution of the surface science of catalysis from single crystals to metal nanoparticles under elevated pressure (From reference 1; Copyright permission obtained from the American Institute of Physics)

1.2 Heterogeneous Catalysis and Surface Science

Catalysis, especially heterogeneous catalysis plays an extremely important role in global production of several valuable chemicals. Generally catalysts are necessarily involved at some point in the production of 80% of manmade chemicals, and the majority of these chemicals are produced by the heterogeneous catalysis route.[5] This contribute directly or indirectly to around 35 % of world GDP.[5] The heterogeneous catalyst has many intrinsic advantages over its homogeneous counterpart like low cost, high stability, recyclability and low toxicity. They are also easy to synthesize, handle, recover from the reaction mixture, and reuse. The heterogeneous catalytic reactions take place on the surface of a solid catalyst, and many surface chemical processes occur during the catalytic reaction like adsorption of reactant(s), surface diffusion, and reaction between adsorbed species and desorption of product(s).

Figure 1.2 gives a schematic representation of various processes associated in a gas-solid catalytic reaction. The main goal of heterogeneous catalysis research is to understand these elementary processes at the molecular level and their relations with the catalyst composition and electronic structures; by acquiring this knowledge one can go to the next step is to design a better catalyst of improved activity and selectivity. Before the 1960's the catalysis, especially heterogeneous catalysis, was considered as either an "art" or "black box magic". The surface science has played a pivotal role in the development, production and the fundamental understanding of valuable catalyst systems.

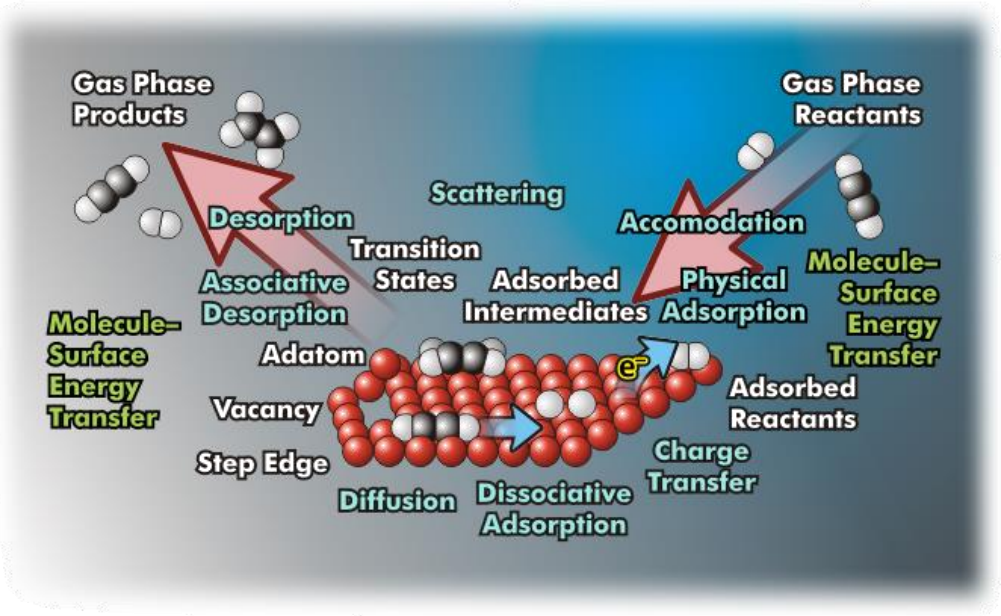

Figure 1.2: Various surface chemical phenomena during a heterogeneous catalytic reaction. (From Ref 6; Copyright permission obtained from BNL)

Over the past several decades, a molecular level understanding of surface properties and adsorbate structures has been made on many model catalysts by developing a handful of surface sensitive techniques. In 2007, Surface chemist Gerhard Ertl was awarded the Nobel Prize in Chemistry for his scientific contributions to understand the chemical process on a solid surface. Notably, Ertl decisively contributed to the rate limiting step in ammonia synthesis and the non-linear kinetics observed for CO oxidation kinetics on Pt supported zeolites. He also developed necessary surface analytical methods such as photoelectron

emission microscopy (PEEM), which was not present in seventies, to visualize the non-linear kinetics due to surface structural changes.

In many cases, the surface scientists have shown very good correlations between model and industrial catalyst samples. The ammonia production is the best-known example for model correlation between model and industrial catalyst system.[7] However, the correlation between surface science studies and "real world" catalysis is not always satisfactorily established. Conventional approach of exploring the catalysis on pure metal or single crystal surfaces with sophisticated high vacuum techniques often failed to explain the changes occurring on the real-world catalyst materials under real-world conditions. This is mainly due to a "disconnect" between the surface science approach operating under ideal conditions, and the real-world catalysis happening under drastically different conditions of high pressure on complex real-world catalysts. The major challenge of catalysis research is the prior designs of catalyst for a reaction which can give high selectivity and reactivity for a particular product.[8] This challenge opens a window for heterogeneous catalysis research in many aspects. These aspects mainly divided into two parts, theoretical and experimental aspects. The theoretical aspects are founded on the electron density function or electronic wave function calculations.[9] These aspects mainly deal with the electronic and mechanical bulk properties of the catalyst. The experimental aspects are based on the various approaches like preparation techniques, mechanistic-kinetic elucidation, activity-selectivity testing, etc. These aspects are integrated too many factors to understand the catalytic reactions and cycles.

There are such a large number of processes occur on the catalyst surface (as explained in Figure 1.2) under the reaction conditions, which makes the surface analysis very much complex. Adsorption of reactants followed by dissociation, diffusion of reactants, products formation and finally desorption of products. During these processes there could be many other steps involved such as, charge transfer between adsorbates and with catalyst surface, non-regular sites (such as edge or corner sites) can react differently, spill-over and reverse spill-over process and possibility of any poisoning due to impurities. The complicity or more precisely the structural and chemical complicity is the dilemma of catalysis research. However, these complications provide the great opportunity for better understanding of

catalytic material behavior. There are two major hurdles in correlating the results obtained from controlled surface science experiments and industrial catalyst samples under real-world catalysis conditions. The first is the surface science experiments, which required atomically clean surface and the second is ultra-high vacuum (UHV) condition to avoid the momentum and energy loss of probe atom/ion/electron. Then the question that emerges is on how to handle the complicity of reaction process? To handle this complicity, historical approach suggested by Langmuir in 1922 could be adopted.[10] This approach is described in his words: "Most finely divided catalyst must have the structure of great complexity. In order to simplify our theoretical consideration of reaction at the surface, let us confine our attention to the plane surface. If the principle, in this case, is well understood, it should be possible to extend the theory to the case of porous bodies. In general, we should look upon the surface consisting of a checker board". Since 1960, the metal single crystals are used for surface science studies to correlate with model catalyst and real-world catalysis process. The extrapolation of an experimental result obtained from this approach is successfully able to explain the significant number of heterogeneous catalytic process giving the hope that someday the entire heterogeneous catalytic process can be explained by this approach. The ammonia synthesis system is a classic example for the success of this approach.[7] The 70 years of research on ammonia synthesis finally led to the conclusion that the chemisorption of N_2 into atomic nitrogen over the Fe catalyst surface is the rate determining step[7] and developed a kinetic theory that precisely predicted the catalytic reaction rate.[11] Unfortunately, there are many catalytic process[12-16] which are less known from the molecular point of view. It doesn't mean that this strategy is failing. It is because of the structural and chemical complexity of a heterogeneous catalyst system is poorly understood.

The major hurdle in understanding structure-reactivity is the dynamic nature of surface and bulk. Here, dynamic nature indicates, but not limited to, geometry of the surface, electronic state of active center, composition etc. Thus the catalytic activity and selectivity are controlled by the metal support interaction, geometry and electronic state of the active center, promoters, poison, catalyst preparation method, etc. It is very necessary to include all these

factors for proposing a kinetic theory or reaction mechanism model for the catalysis reaction. The definite single crystal surfaces are used in the classical surface science studies and the single collision, scattering of the molecule, adsorption-desorption are prominent phenomena on these crystal surfaces. Whereas, in real word catalysis condition, single metal or more than one metal or their oxide catalyst are supported on various support materials, therefore, the restructuring of catalyst, diffusion, heat or mass transfer, multiple adsorptions are the prominent phenomena in the industrial catalyst (explained in Figure 1.2). Thus, there is a serious "disconnect" between the classical surface science studies and real-world catalysis with respect to the material. This disconnection between these two extreme is known as the "material gap." The material gap arises because of many factors[16] which are shown in Figure 1.3. There are several efforts have been made globally to bridge the material gap. The industrial catalysts are mainly metal or their oxides supported on the high surface area materials which are directly not suitable for surface science studies. Gunter et al. proposed the concept of flat model support catalyst system which is the replacement of porous material and suitable for UHV surface science studies.[18] Nano metal particle can be deposited by suitable vacuum method. However, this model cannot be employed for high temperature studies. Another solution is the spin coating which is proposed by the Kuipers et al.[19] Saib et al., [20] employed spin-coating technique successfully for generating metal-supported thin films for exploring many details of reactions ranging from ethylene polymerization to Fischer–Tropsch synthesis. Sol–gel dip coating method employed by Brinker et al.[21] is another useful way for making quality thin films for reproducing catalytically relevant surfaces. However, number of problems is yet to be answered satisfactorily; importantly the correlation between surface properties measured on thin films under ideal conditions and catalysis on corresponding powder materials and measured at ambient pressure and high temperatures. Dubey et al. successfully prepared porous ceria-zirconia thin film and addressed the fundamental aspects such as adsorption, diffusion, and other elementary reaction steps, heat and mass transfer by using MBI and NAP-PES (Figure 1.4).[22-26] Specialty of this series of reports lies in generating porosity of the material within the thin films and addressing the diffusion into the pores. This is achieved while maintaining the high quality surface, but

prepared by simple wet-chemical methods. Dubey et al. also demonstrated a correlation between surface science parameters measured, such as oxygen storage capacity, sticking coefficient to that of the bulk kinetics measured for CO oxidation on ceria-zirconia surfaces. It is also to be mentioned that diffusion of oxygen atoms into the bulk of the thin film occurs; while this can be measured (to quantify oxygen storage capacity), the same also complicates the analysis and underscores the dynamics that occur under measurement conditions. Importance of this particular study is the simulation of actual reaction conditions that occur under surface science measurement conditions, and hence its total relevance to the heterogeneous catalysis. More such studies are required to address the complicated issues in heterogeneous catalysis from surface science point of view.

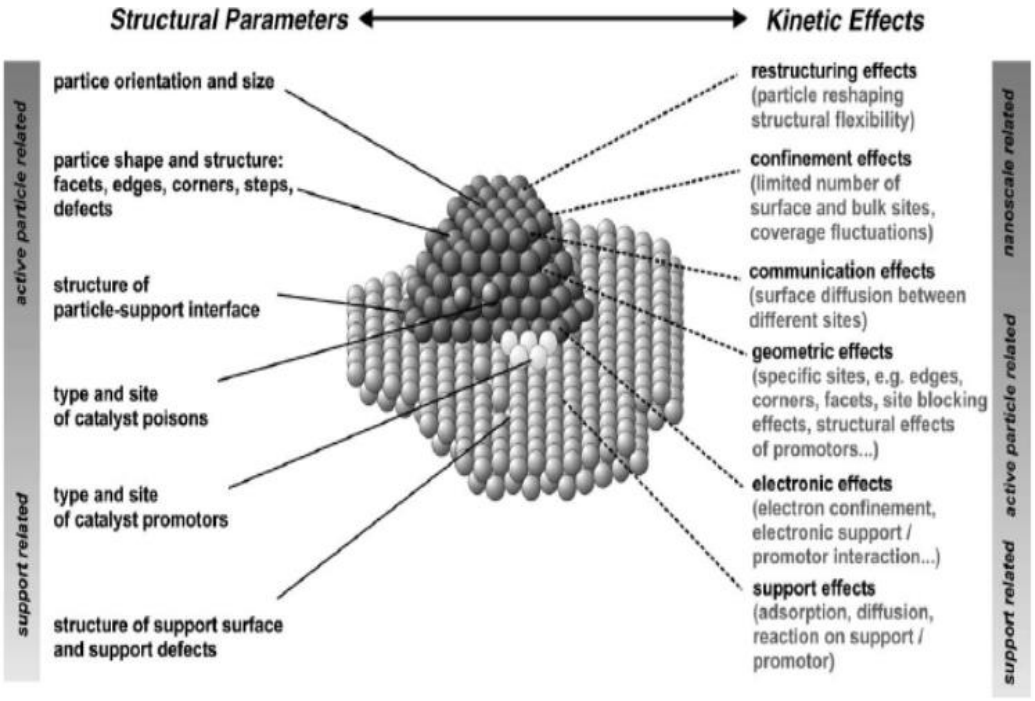

Figure 1.3: Structural parameter and kinetic effect on the supported metal catalyst (from reference 17; copyright permission obtained from Elsevier publishers.)

The other aspect which comes in between surface science and practical catalysis is the significant to large difference in their pressure regimes. Most of the surface science techniques use electrons, photons, or ion beams as probes or detection tool, which need high vacuum conditions. Therefore, many important surface sensitive techniques are operational

under ultra-high vacuum (UHV) conditions. UHV condition is essential to obtain information from a very clean or atomically clean surface of catalyst material. However, this stands far from the thermodynamic chemical equilibrium condition. It seems the system is locked in an adiabatic condition, and can hardly simulate the changes in chemical potential and surface space charge which occur due to the presence of reactants in a practical situation

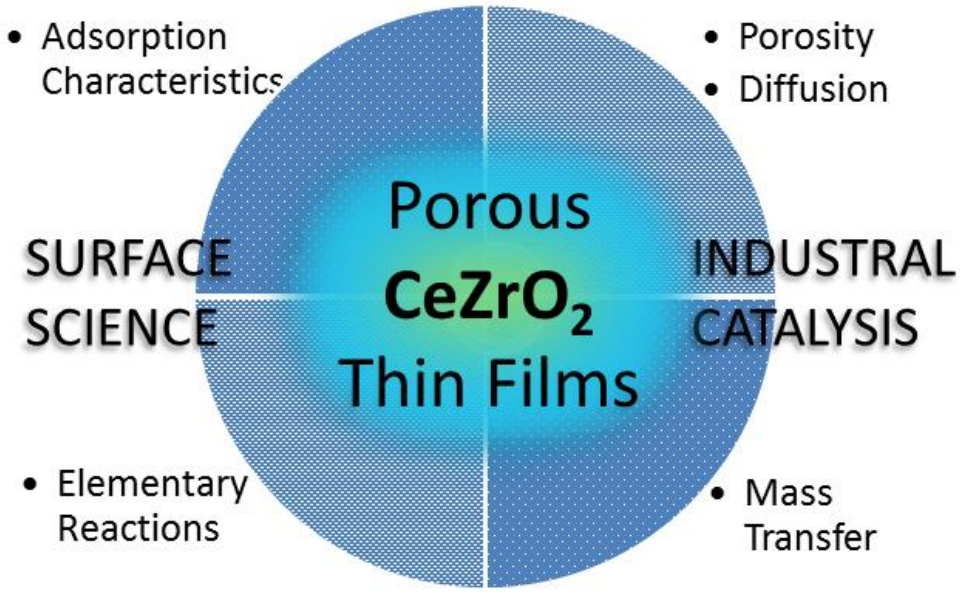

Figure 1.4: Porous thin films is the possible solution to uncover the various processes involved in heterogeneous catalysis under operando conditions and investigated by surface science methods (from reference 22; copyright permission obtained from Taylor & Francis publishers.)

Especially, ambient or high pressure employed in many industrial catalysis conditions lead to many changes, such as weakly adsorbed reactants, spill-over of reactant(s) from active to support material or the reverse, are difficult to simulate under high vacuum conditions. This huge difference in operating conditions is termed as "pressure gap' in heterogeneous catalysis (Figure 1.5). In the last few decades a number of surface sensitive techniques have been developed which could be operated under elevated pressure regimes, among them are near-ambient pressure photoelectron spectroscopy (NAPPES), sum-frequency generation (SFG), neutral-impact collision ion scattering spectroscopy (NICISS), high pressure scanning-

-tunneling microscopy, environmental scanning electron microscopy, near edge X-ray absorption fine structure (NEXAFS), meta-stable impact electron spectroscopy (MIES) etc. Among them, NAP-PES is a versatile technique that can be advantageously used for characterization of a number of surface properties of the solid surface and interfaces, like chemical composition, oxidation state, element mapping, gas-solid interactions, etc. under near-operando conditions. Many new results are being reported in the last decade on several aspects of heterogeneous catalysis. Notably, systematic surface modification of palladium to palladium with oxygen in the subs-surfaces and demonstration of the same for ambient temperature CO oxidation, copper/cobalt/molybdenum oxidation to corresponding oxides, hydrogen reduction of ceria-zirconia surfaces, CO oxidation on Co_3O_4 nanorod surfaces and the influence of water vapor on such surfaces.[26-33] Following these works, our group reported on interaction of molecular oxygen with silver surfaces under technically relevant conditions and the results are described in chapter 3A.

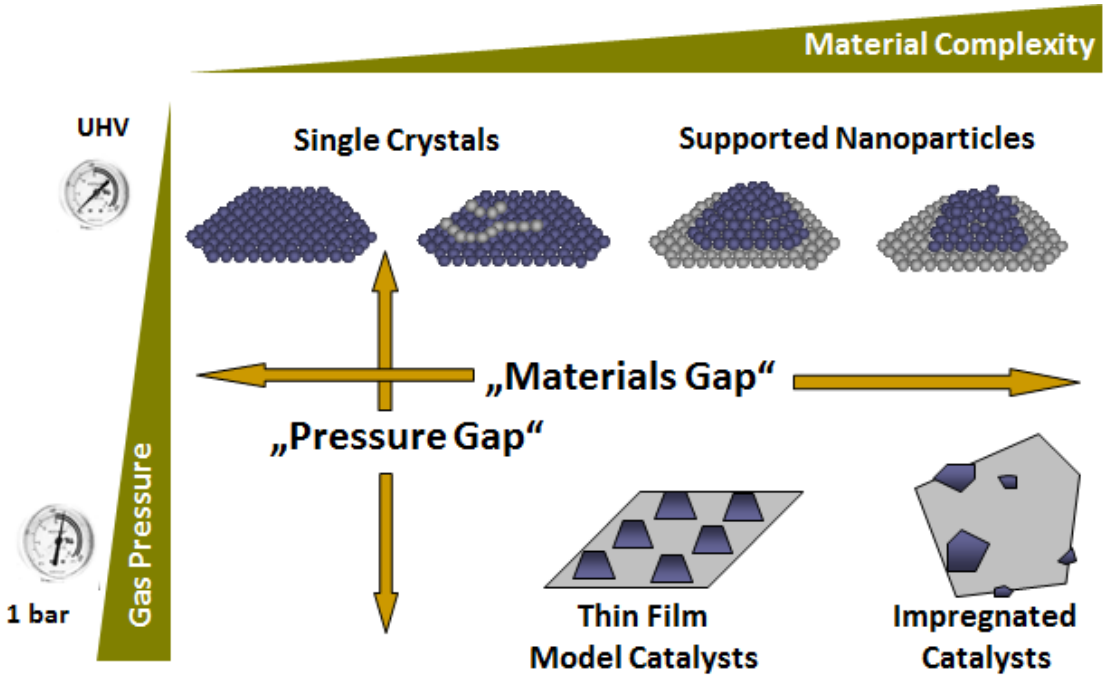

Figure 1.5: The graphical representation of the pressure gap and material gap existing between classical surface science measurement studies and industrial heterogeneous catalysis conditions (from reference 34, copyright permission obtained from University of Innsbruck)

In chapter 3 part A, we have studied the Ag-O_2 interactions by and near-ambient pressure X-ray photoelectron spectroscopy (NAP-XPS) and near-ambient pressure ultraviolet photoelectron spectroscopy (NAP-UPS). The Ag-O_2 interactions, which are the center-stage of Ag-catalyzed partial oxidation reactions, especially for ethylene to ethylene oxide (EtO). Ethylene to EtO conversion takes place on metallic silver catalyst without formation of any bulk silver oxide, and this is an interesting example of a kinetically controlled selective oxidation reaction. However, carbon dioxide formation is thermodynamically more favorable on the silver catalyst. There is no doubt that Ag – O interaction is the critical factor to control the selectivity of EtO.[35-37]

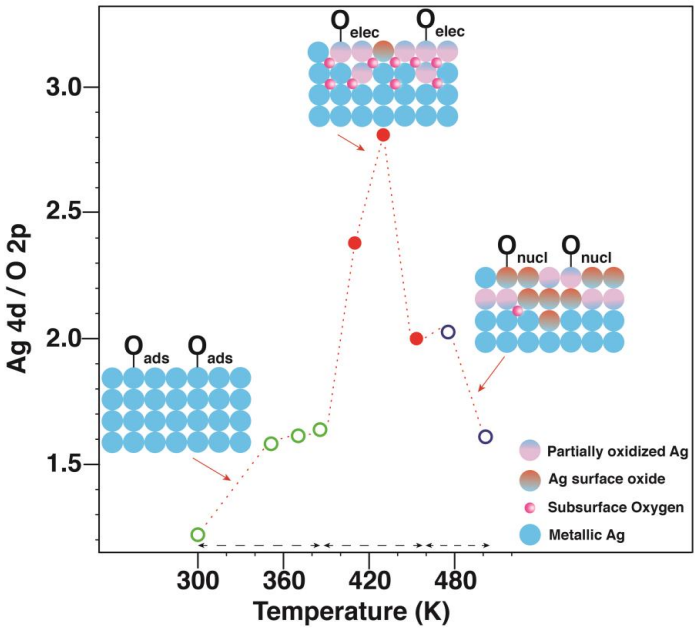

Figure 1.6: Surface electronic changes that occur on silver surfaces due to its interaction with oxygen between 300 and 500 K. Note the maximum change observed for Ag 4d/O 2p between 400 and 450 K is in good correlation with that of maximum epoxidation catalytic activity observed on industrial Ag/Al_2O_3.

For the last 50 years, this reaction was explored by the theoretical and experimental method to understand the Ag – O interaction and different models have been proposed; however, the mechanism still remains heavily debated. In this work, silver valence band was probed by photoelectron spectroscopy at near ambient pressure of molecular oxygen (up to 0.2 mbar) with He I excitation as photon source. Three distinct silver-oxygen interactions

regimes have been identified between 300 and 500 K (Figure 1.6), namely, (a) oxygen chemisorption between ambient and 390 K, (b) O-diffusion into the subsurface layers of Ag between 390 to 450 K, and (c) formation of metastable oxide on Ag surface above 450 K; the latter two regimes are dynamic in nature. The trend in oxygen coverage (θ_O) observed on the Ag surface below 350 and above 475 K is comparable; however, it is the lowest between 390 and 450 K, but in the presence of large excess gas-phase O_2, highlights the unique nature of the Ag+O_2 interaction. Interaction with oxygen changes the work function (ϕ) of Ag from 4.95 ($\leq$390 K) to 5.30 eV (390-450 K), and then to 5.7 eV ($\geq$450 K). The present study suggests that O-atom diffusion into the Ag subsurface plays the key factor for epoxidation. Subsurface oxygen plays the major role in selective epoxidation by two ways; it changes the nature of Ag surface to be electron deficient in nature and creates a space charge region above the Ag surface. O-atoms that adsorb on electron deficient Ag surface act as electrophilic oxygen, which gets inserted into electron-rich alkene to form an epoxide. Above 450 K, oxygen binds strongly to the Ag surface and acts as nucleophilic oxygen. The nucleophilic oxygen favors complete combustion of alkene to carbon dioxide. The metallic surface reappears when O_2 supply is removed above 400 K. Present study emphasizes the necessity of *in situ* and operando investigations to understand the active nature of any catalyst.

In chapter 3 part B, we have synthesized 5 wt % Fe_2O_3/support (support=Al_2O_3, CeO_2, MgO, ZSM-5 and Nb_2O_5) catalysts by wet impregnation method. The synthesized catalysts are subjected to different physicochemical characterization techniques to understand the structure and morphology of the catalysts. These catalysts were screened for butane ODH reaction in fixed bed reactor at different temperatures between (523 K to 873 K with varying butane: oxygen ratio (1:1, 1:0.5 and 1:0.25)). Among all these catalysts Fe_2O_3/Al_2O_3 catalyst shows the best activity in terms of 1,3-butadiene yield (higher selectivity towards 1,3-butadiene) at temperature evaluated. In order to understand the superior nature of the active site of the Fe_2O_3/Al_2O_3 catalyst, properties of not-so-active catalyst, i.e., Fe_2O_3/Nb_2O_5 was compared by performing *in-situ* XPS analysis under simulated reaction conditions. The NAP-XPS spectra of Fe_2O_3/Al_2O_3 and Fe_2O_3/Nb_2O_5 are carried out at 0.1 mbar pressure of butane: oxygen: argon (2:1:3) between 300 to 873 K. It has been observed at room temperature the Fe

is present in Fe_2O_3 phase on both support. From the temperature dependent NAP-XPS studies carried out on both catalysts at different temperatures it is observed that there is no change in the oxidation state of Fe catalyst on the Nb_2O_5 catalyst, i.e. there is no or minimum interaction between Fe and Nb_2O_5. Whereas, Fe is reduced to Fe^{+2} state on Al_2O_3 support, and there is a possibility of iron carbide formation is indicated. These result confirmed that Fe^{+2} is the active species for high selectivity for 1, 3- butadiene which is stabilized by the Al_2O_3 support.

1.3 Gas-Solid Interaction: The Fundamental phenomenon of heterogeneous catalysis and Electronic Structure modification

The chemical reactions on the surfaces are very important for many areas of science and technology. Especially, the gas-solid interaction is the foundation of various surface dependent applications like, heterogeneous catalysis, electrochemistry, sensors, semiconductor etc. For the first time, Hugo et al. discovered the association of kinetic oscillation of CO oxidation reaction on supported Pt catalyst[39, 40] and this is also first reaction which is studied by using surface science approach on well-defined single crystal Pt (110) surface under low pressure condition.[41] Now, this reaction mechanism is well established[42,43] and it proceed with following elementary reaction steps:-

$$CO + *CO_{ad}$$

$$O_2 + 2* \rightarrow 2\ O_{ad}$$

$$O_{ad} + CO_{ad} \rightarrow CO_2 + 2*$$

Here * denotes the vacant adsorption site

According to the reaction mechanism the pre-adsorbed CO strongly inhibit the dissociative adsorption of molecular oxygen. Therefore, high temperature is required (>400 K) during the steady state flow condition to continuous desorption of CO adsorbates to create the free adsorption sites; otherwise, CO would completely block the surface sites, consequently, there won't be any catalytic reaction. Gopinath et al. have shown the effect of Pd surface modification on CO oxidation reaction at room temperatures.[33] Pd surface is

modified by the oxygen diffusion in to subsurface. The oxygen diffusion to sub-surface region, modified the electronic nature of Pd catalyst, consequently, the CO poisoning of Pd surface was partially reduced. Hence, the reaction temperature is shifted to 350 K from high temperature (>400 K).[44] Derouin et al.[45] also studied the similar kind of sub surface modification of silver to explain the selectivity towards the ethylene epoxide in to a narrow temperature window (400 to 500 K). By using the combination of surface science techniques, such as STM, LEED and TPD, that in between 400 and 500 K subsurface oxide is formed. When the subsurface oxide is formed the silver surface is dramatically reconstructed to striped structure at the cost of all other surface structure shown in Figure 1.7. Interestingly, the subsurface oxygen formation is hindered above 500 K. The temperature dependence of subsurface oxygen formation might be the key factor for the industrial catalyst for the high selectivity towards ethylene epoxidation around 450 K rather than CO_2 formation.

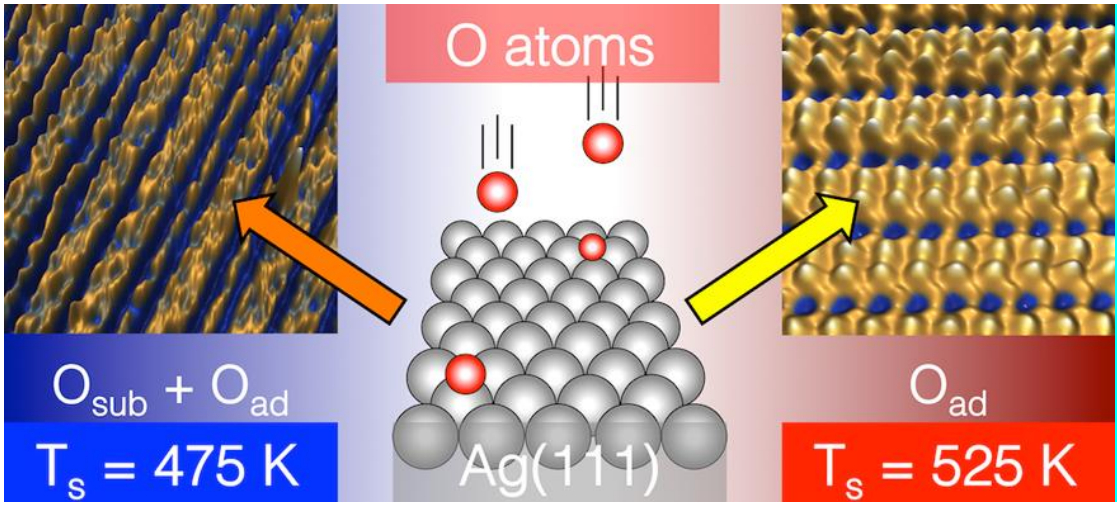

Figure: 1.7 Thermally selective formation of subsurface oxygen in Ag(111) and consequent surface structure (from reference 45, copyright permission obtained from ACS publication)

Since the middle of 19th century the concepts of semiconductor physics are used to explain the working mode of selectivity of oxidation catalyst, especially alkane and alkene oxidation.[46-49] According to semiconductor theory, the charge created due to the fermi potential difference between catalyst and redox potential of adsorbate molecule is the driving force for the charge transfer between bulk surface to adsorbate interface.[49] The height of

surface barrier, which charge carrier have to overcome between surface and bulk, could have a significant impact on the activation of adsorbed species as well as selectivity of catalyst. Eichelbaum et al. applied the NAP-XPS to address this fundamental issue.[50] The selective oxidation of n-butane to maleic anhydride reaction was studied on the moderately selective $MoVTeNbO_x$ (M1 phase), highly selective vanadyl pyrophosphate catalyst, and total oxidation catalyst V_2O_5. It has been observed that the highly selective vanadyl pyrophosphate catalyst act as a semiconductor gas sensor and shows the dynamic charge transfer between bulk and the surface, consequently, it shows gas phase dependent response of ϕ. Whereas the total oxidation catalyst V_2O_5 does not show any ϕ changes due to reactant adsorption. It was suggested that the surface potential barrier is the descriptor of selectivity to maleic anhydride. However the surface reaction of metal surface and semiconductor surface are very different. On the metallic surface, the surface reaction has been explained by using the sticking coefficient for the adsorbing molecule on the surface, surface adsorption and diffusion of adsorbate, clustering by attractive interactions between adsorbates. Whereas on the semiconductor surface, the bonding is largely covalent in nature and surface electronic states have a tendency to be spatially localized. The sticking coefficient of semiconductor surface is very weak,[51,52] and chemical species also have a tendency to adsorb on the preferential site because of the spatially localized electronic site.[53] The adsorption rate also decreases with decreasing the availability of preferential adsorption site on the semiconductor surface.[54] In addition to this, the surface diffusion on the semiconductor surface is also insignificant because of the spatially localized electronic site which reduces the surface mobility of the adsorbed species. Therefore the models which are used to explain for metal and adsorbate interaction are unable to explain the molecular reaction on the semiconductor surfaces. All these complications make the semiconductor surface difficult to understand a priori, how the molecular adsorption takes place on a specific site of virgin surface and the completion of process on the whole surface. Many technologically important surface reactions proceed through various surface processes such as, epitaxial layer growth, dopant incorporation, patterning of semiconductor surfaces by self-assembly. These processes have vital implications for the structural and electronic properties, and therefore the -

performance, of semiconductor devices, especially, nanostructured devices that need high native management over surface properties. The recent investigations have featured the significance of particular specific surface sites and local reaction to absorbable species in surface reaction on semiconductor surfaces.

In this direction, in chapter 4, NAP-UPS and NAP-XPS studied of Silicon is carried out in the presence of molecular oxygen at near ambient pressure (up to 0.5 mbar and 900 K) to understand the various steps involved in the initial oxidation of silicon surface and towards silica formation. Initially, the oxygen adsorbs on the dangling bond sites which can be measured by the decrease in the intensity of the dangling bond in NAP-UPS spectra. The adsorption of oxygen on the dangling bonds is localized because of that the topography of the Si surface becomes heterogeneous in nature, which is responsible for the broadening in the oxygen gas phase vibrational spectra. According to literature reports,[55, 56] the initially adsorbed oxygen is molecular in nature, which is also known as Höfer precursor. Initial strong increase in the ϕ can be correlated with the presence of Höfer precursor and this state is stable up to 400 K. When the temperature increases to 500 K, this species dissociates to –Si=O species which can be confirmed by the decrease in the ϕ as well as by the NAP-XPS. At 600 K the –Si=O species dissociates and form a uniform 2D oxide layer on the silicon surface. This layer is also quite stable up to 800 K, and there is not much change observed in NAP-UPS as well as NAP-XPS. However, when the temperature increases up to 850 K at 0.2 mbar oxygen pressure, bulk Si oxidation begins to take place and the ϕ increase to 1 eV which is confirmed by the secondary electron cut off in UPS spectra as well as a shift in gas phase vibrational spectra. To find out the composition of the Si surface, the angle-resolved spectra is also carried out and found that Si did not completely oxidize to Si^{+4}. Other species like Si^{+1}, Si^{+2}, Si^{+3} also present from bulk to the surface.

In chapter 5, the gas phase vibrational spectra of reactive and inert gases have been studied by (NAP-UPS) up to 0.3 mbar. Results obtained is divided into two parts and discussed. In the first part, we have studied the photoelectron spectrum of monoatomic Argon gas and some homonuclear diatomic molecules like H_2, O_2, and N_2 by using NAP-UPS and the effect of pressure on their energy position. The atomic/molecular gas phase spectrum is essential to study the atmospheric and exo-atmospheric gas-phase composition. In this study, we have demonstrated that NAP-UPS could be an essential tool to determine the -

intermolecular interaction. In the second part, we have studied the influence of solid surface nature on the binding energy (BE) position and pattern of the vibrational features of nitrogen and the first shallow levels ($3p_{3/2}$ and $3p_{1/2}$) of Argon. It has been observed that with change in the (electronic) nature of the surface, the BE of the above states also changes and reflects the change in the ϕ of the material. It is to be underscored that Ar is an inert gas and nitrogen is the most stable molecule, and the above changes observed underscores that they can be employed as probe atom/molecule to explore even the minor changes occurring for any reason. Further, if the solid surface undergoes any chemical/electronic changes due to gas-solid interaction, such as oxidation, the ϕ of the surface changes again; this underscores the identification of changes happening under reaction/measurement conditions. Therefore, the change in the BE of the gas phase features can be used to determine even the minor ϕ changes of solid surfaces during the reaction or due to the reaction. These sets of findings have implications to probe the surface changes that occur in any surface dependent phenomena, such as heterogeneous catalysis, electrochemistry.

In the present thesis efforts are directed to explore and understand the fundamental phenomenon of heterogeneous catalysis, which is the gas-solid interaction with different systems. On the way, controlled material making is also addressed by oxidizing Si to SiO_x layers, Ag to modified silver with oxygen in the subsurfaces. Most reactive and most stable molecule/atom was employed to probe the gas-solid interaction with NAPPES technique under relevant conditions for very different surfaces. Some of the critical results, such as changes in surface ϕ, charge transfer between surface and molecules, are addressed in the present thesis. Butane to 1,4-butadiene was explored on a working catalyst and active species are identified from the NAPPES studies.

1.4 References:-

1. Somorjai, G. A.; Park, J. Y., Evolution of the surface science of catalysis from single crystals to metal nanoparticles under pressure. *J. Chem. Phys.* **2008**, *128*, 182504 (1-9)
2. Sinfelt, J. H., Role of surface science in catalysis. *Surf. Sci.* **2002,** *500*, 923-946
3. Ekerdt, J.; Sun, Y.-M.; Szabo, A.; Szulczewski, G.; White, J., Role of surface chemistry in semiconductor thin film processing. *Chem. Rev.* **1996,** *96*, 1499-1518

4. D'Orazio, P., Biosensors in clinical chemistry. *Clin. Chim. Acta.* **2003,** *334*, 41-69.
5. Z. Ma, F. Zeara, Heterogeneous catalysis by metals in Encyclopedia of Inorganic Chemistry. John Wiley, **2006**
6. https://www.bnl.gov/chemistry/programs/Surface_dynamics.asp
7. Ertl, G., Elementary steps in heterogeneous catalysis. *Angew. Chem. Int. Ed.* **1990,** *29*, 1219-1227.
8. McLaughlin, N. M.; Castaldi, M. J., Measurement techniques in catalysis for mechanism development: kinetic, transient and *in situ* methods. *Catalysis* **2009,** *21*, 191-218
9. Nørskov, J. K.; Abild-Pedersen, F.; Studt, F.; Bligaard, T., Density functional theory in surface chemistry and catalysis. *Proc. Natl. Acad. Sci. U. S A.* **2011**, 201006652
10. Zecchina, A.; Califano, S., The Development of Catalysis: A History of Key Processes and Personas in Catalytic Science and Technology. *John Wiley & Sons*: **2017**.
11. Stoltze, P., Surface Science as the Basis for the Understanding of the Catalytic Synthesis of Ammonia. *Phys. Scr.* **1987**, 824.
12. Beaumont, S. K., Recent developments in the application of nanomaterials to understanding molecular level processes in cobalt catalysed Fischer–Tropsch synthesis. *Phys. Chem. Chem. Phys.* **2014**, 5034-5043.
13. Lafarga, D.; Al-Juaied, M. A.; Bondy, C. M.; Varma, A., Ethylene epoxidation on Ag-Cs/α-Al_2O_3 catalyst: Experimental results and strategy for kinetic parameter determination. *Ind. Eng. Chem. Res.* **2000**, *39*, 2148-2156
14. Chen, C. J.; Harris, J. W.; Bhan, A., Kinetics of Ethylene Epoxidation on a Promoted Ag/α-Al_2O_3 Catalyst—The Effects of Product and Chloride Co-Feeds on Rates and Selectivity. *Chem. Eur. J.* **2018** *24*, 12405-12415
15. Khirsariya, P.; Mewada, R. K., Single step oxidation of methane to methanol–towards better understanding. Procedia Engineering **2013**, *51*, 409-415
16. Latimer, A. A.; Kakekhani, A.; Kulkarni, A. R.; Nørskov, J. K., Direct Methane to Methanol: The Selectivity–Conversion Limit and Design Strategies. *ACS Catal.* **2018**, *8*, 6894-6907.
17. Libuda, J.; Freund, H.-J., Molecular beam experiments on model catalysts. *Surf. Sci. Rep.* **2005**, *57*, 157-298.

18. Gunter, P. L.; Niemantsverdriet, J.; Ribeiro, F. H.; Somorjai, G. A., Surface science approach to modeling supported catalysts. *Catal. Rev.* **1997**, *39*, 77-168
19. Kuipers, E.; Laszlo, C.; Wieldraaijer, W., Deposition of nanocrystals on flat supports by spin-coating. *Catal. Lett.* **1993**, *17*, 71-79.
20. Saib, A.; Borgna, A.; Van de Loosdrecht, J.; Van Berge, P.; Niemantsverdriet, J., *In situ* surface oxidation study of a planar $Co/SiO_2/Si$ (100) model catalyst with nanosized cobalt crystallites under model Fischer− Tropsch synthesis conditions. *J. Phys. Chem. B* **2006**, *110*, 8657-8664.
21. Brinker, C. J.; Frye, G.; Hurd, A.; Ashley, C., Fundamentals of sol-gel dip coating. *Thin solid films* **1991,** *201*, 97-108.
22. Dubey, A.; Kolekar, S. K.; Gnanakumar, E. S.; Roy, K.; Vinod, C.; Gopinath, C. S., Porous thin films toward bridging the material gap in heterogeneous catalysis. *Catal. Str. React.* **2016**, *2*, 1-12.
23. Dubey, A.; Kolekar, S. K.; Gopinath, C. S., C− H Activation of Methane to Syngas on $Mn_xCe_{1-x-y}Zr_yO_2$: A Molecular Beam Study. *ChemCatChem* **2016**, *8*, 2296-2306
24. Dubey, A.; Kolekar, S. K.; Gopinath, C. S., C− H Activation of Methane to Formaldehyde on $Ce_{1-x}Zr_xO_2$ Thin Films: A Step to Bridge the Material Gap. *ChemCatChem* **2016**, *8*, 3650-3656.
25. Kolekar, S. K.; Dubey, A.; Date, K. S.; Datar, S.; Gopinath, C. S., An attempt to correlate surface physics with chemical properties: molecular beam and Kelvin probe investigations of $Ce_{1-x}Zr_xO_2$ thin films. *Phys. Chem. Chem. Phys*. **2016**, *18*, 27594-27602.
26. Jain, R.; Dubey, A.; Ghosalya, M. K.; Gopinath, C. S., Gas–solid interaction of H_2–$Ce_{0.95}Zr_{0.05}O_2$: new insights into surface participation in heterogeneous catalysis. *Catal. Sci. Tech*. **2016**, *6*, 1746-1756.
27. Reddy, K. P.; Mhamane, N. B.; Ghosalya, M. K.; Gopinath, C. S., Mapping Valence Band and Interface Electronic Structure Changes during Oxidation of Mo to MoO_3 via MoO_2 and MoO_3 Reduction to MoO_2: A NAPPES Study. *J. Phys. Chem. C* 2018.
28. Jain, R.; Gnanakumar, E. S.; Gopinath, C. S., Mechanistic Aspects of Wet and Dry CO Oxidation on Co_3O_4 Nanorod Surfaces: A NAP-UPS Study. *ACS Omega* 2017, 2, 828-834

29. Roy, K.; Gopinath, C. S., UV photoelectron spectroscopy at near ambient pressures: Mapping valence band electronic structure changes from Cu to CuO. *Anal. Chem*. 2014, 86, 3683-3687
30. Ghosalya, M. K.; Reddy, K. P.; Jain, R.; Roy, K.; Gopinath, C. S., Subtle interaction between Ag and O_2 : a near ambient pressure UV photoelectron spectroscopy (NAP-UPS) investigations. *J. Chem. Sci.* 2018, *130*, 30.
31. Reddy, K. P.; Jain, R.; Ghosalya, M. K.; Gopinath, C. S., Metallic Cobalt to Spinel Co_3O_4 : Electronic Structure Evolution by Near-Ambient Pressure Photoelectron Spectroscopy. *J. Phys. Chem. C* **2017**, *121*, 21472-21481.
32. Jain, R.; Reddy, K. P.; Ghosalya, M. K.; Gopinath, C. S., Water-Mediated Deactivation of Co_3O_4 Naonrods Catalyst for CO Oxidation and Resumption of Activity at and Above 373 K: Electronic Structural Aspects by NAPPES. *J. Phys. Chem. C* **2017**, *121*, 20296-20305.
33. Gopinath, C. S.; Roy, K.; Nagarajan, S., Can We Shift and/or Broaden the Catalysis Regime towards Ambient Temperature? *ChemCatChem* **2015**, *7*, 588-594
34. https://webapp.uibk.ac.at/physchem/nmci/research/topics/thin-film-model-systems
35. Böcklein, S.; Günther, S.; Wintterlin, J., High-Pressure scanning tunneling microscopy of a silver surface during catalytic formation of ethylene oxide. *Angew. Chem. Int. Ed.* **2013**, *125*, 5628-5631.
36. Jones, T. E.; Rocha, T. C.; Knop-Gericke, A.; Stampfl, C.; Schlögl, R.; Piccinin, S., Thermodynamic and spectroscopic properties of oxygen on silver under an oxygen atmosphere. *Phys. Chem. Chem. Phys.* **2015**, *17*, 9288-9312
37. Michaelides, A.; Bocquet, M.-L.; Sautet, P.; Alavi, A.; King, D., Structures and thermodynamic phase transitions for oxygen and silver oxide phases on Ag {(111). *Chem. Phys. Lett.* **2003**, *367*, 344-350.
38. Heine, C.; Eren, B.; Lechner, B. A.; Salmeron, M., A study of the O/Ag (111) system with scanning tunneling microscopy and x-ray photoelectron spectroscopy at ambient pressures. *Surf. Sci.* **2016**, *652*, 51-57
39. Hugo, P., Stability and Time Behavior of Flow Circulation Reactors. *Reports of the Bunsen Society for Physical Chemistry* **1970**, *74*, 121-127.

40. Beusch, H .; Fieguth, P .; Wicke, E., Thermal and Kinetically Induced Instabilities in the Reaction Behavior of Individual Catalyst Grains. *Chem. Engn. Tech.* **1972**, *44*, 445-451.
41. Ertl, G.; Norton, P.; Rüstig, J., Kinetic oscillations in the platinum-catalyzed oxidation of CO. *Phys. Rev. Lett*. **1982**, *49*, 177.
42. Wintterlin, J.; Völkening, S.; Janssens, T.; Zambelli, T.; Ertl, G., Atomic and macroscopic reaction rates of a surface-catalyzed reaction. *Science* **1997**, *278*, 1931-1934.
43. Engel, T.; Ertl, G., Elementary steps in the catalytic oxidation of carbon monoxide on platinum metals. In Advances in Catalysis, Elsevier: **1979**, *28*, 1-78.
44. Ertl, G., Non-Linear Dynamics: Oscillatory Kinetics and Spatio-Temporal Pattern Formation. Handbook of Heterogeneous Catalysis: Online **2008**, 1492-1516.
45. Derouin, J.; Farber, R. G.; Turano, M. E.; Iski, E. V.; Killelea, D. R., Thermally Selective Formation of Subsurface Oxygen in Ag (111) and Consequent Surface Structure. *ACS Catal.* **2016,** *6*, 4640-4646.
46. Boudart, M., Electronic chemical potential in chemisorption and catalysis. *J. Am. Chem. Soc.* **1952**, *74*, 1531-1535.
47. Hansen, N., FF Volkenshtein: The Electronic Theory of Catalysis on Semiconductors. Übersetzung aus dem Russischen von NG Anderson. Pergamon Press, Oxford, London, New York, Paris **1963**. *169*.
48. Haber, J.; Witko, M., Oxidation catalysis—electronic theory revisited. *J. Catal*. **2003**, *216*, 416-424.
49. Morrison, S., Roy The chemical physics of surfaces Plenum Press. New York and London **1977**.
50. Eichelbaum, M.; Hävecker, M.; Heine, C.; Wernbacher, A. M.; Rosowski, F.; Trunschke, A.; Schlögl, R., The electronic factor in alkane oxidation catalysis. *Angew. Chem. Inter. Ed*. **2015**, *54*, 2922-2926.
51. Bratu, P.; Brenig, W.; Gro, A.; Hartmann, M.; Höfer, U.; Kratzer, P.; Russ, R., Reaction dynamics of molecular hydrogen on silicon surfaces. *Phys. Rev. B* **1996**, *54*, 5978-5991.
52. Chaabouni, H.; Bergeron, H.; Baouche, S.; Dulieu, F.; Matar, E.; Congiu, E.; Gavilan, L.; Lemaire, J., Sticking coefficient of hydrogen and deuterium on silicates under interstellar conditions. *Astron. Astrophys.* **2012**, *538*, A128.

53. Joyce, B.; Foxon, C., Adsorption, Desorption and Migration on Semiconductor Surfaces. In Comprehensive Chemical Kinetics, *Elsevier*: **1984**, *19*, 181-289.
54. Carosella, C.; Comas, J., Oxygen sticking coefficients on clean (111) silicon surfaces. *Surf. Sci.* **1969**, *15*, 303-312.
55. Hoshino, T.; Nishioka, Y., Molecular adsorption and dissociative reaction of oxygen on the Si (111) 7× 7 surface. *Phys. Rev*. B 2000, *61*, 4705
56. Silvestre, C.; Shayegan, M., Observation of a metastable precursor for adsorption of oxygen on Si (111) and the activation energy for chemisorption. *Phys. Rev B* 1988, *37*, 10432

Chapter 2

Experimental methods

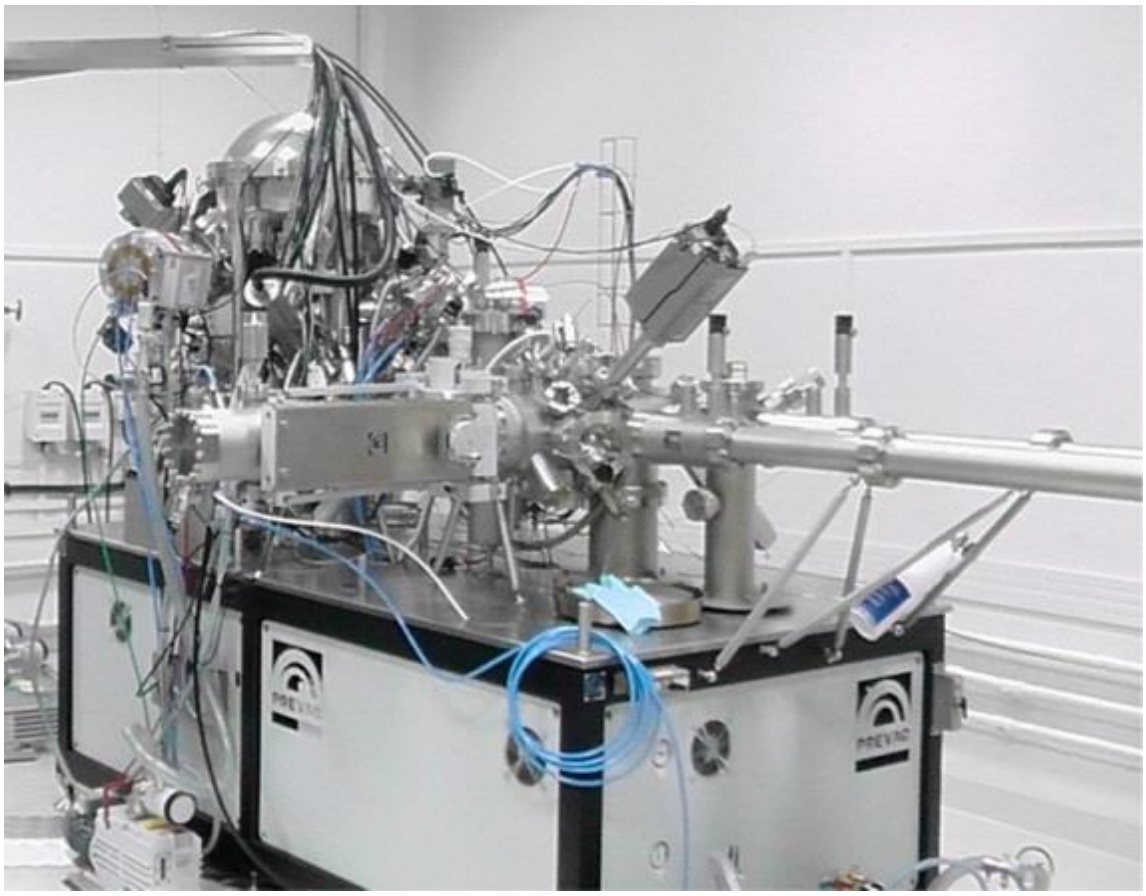

2.1 History, Principle and General Introduction of Photoelectron Spectroscopy

Surface science and heterogeneous catalysis have an immense impact in this technology driven world and has significant contribution in the world GDP. It is a challenging task to develop new materials and processes to remain at the forefront of advanced technology. In the last few decades, surface science emerged as a strong interdisciplinary science and shows a prominent role in the development of new technologies. Parallel to the development of surface science, various surface characterization techniques are also developed, and they contribute to the advancement of surface science knowledge. Among them photoelectron spectroscopy is a versatile technique that can be advantageously used for characterization of a number of surface properties of the solid surface and interfaces, like chemical composition, oxidation state, element mapping, solid-gas interactions etc. The history of photoelectron spectroscopy dates back to the 1950s.[1,2] Based on the work of Kai Siegbahn at Uppsala University, Sweden the high-resolution photoelectron spectrometer was commercialized from the early seventies. Photoelectron spectroscopy works with the principle of the photoelectric effect, which is the emission of photoelectrons from a material when exposed to photons of sufficient energy. The photoelectric effect equation is:

$$h\nu = B.E. + K.E. + \phi \qquad \text{Eq- 2.1}$$

Here, $h\nu$ is the energy of incident photon, $B.E.$ is binding energy required for exciting electron from any occupied level to E_F level in an element, ϕ is the additional energy which is required to eject the electron from E_F, and is known as the work function (ϕ), and K.E. is the kinetic energy of ejected electron which depends on the energy of incident photon. Photoelectron spectroscopy can be divided into two parts based on the radiation source used:

1. X-ray photoelectron spectroscopy (XPS)
2. UV (ultra-violet) photoelectron spectroscopy (UPS / UVPES)

Generally, in a laboratory-based X-ray photoelectron spectroscopy set up, characteristic Al Kα (1486.6 eV) and Mg Kα (1253.4 eV) sources are used as standard X-ray sources, whereas

the source of UV radiation is noble gas discharge lamp, usually a helium discharge lamp. The Helium discharge lamp emits two different energy radiations, namely, He I (21.2 eV) and He II (40.8 eV). Both UV radiations can be obtained by varying the partial pressure of helium.

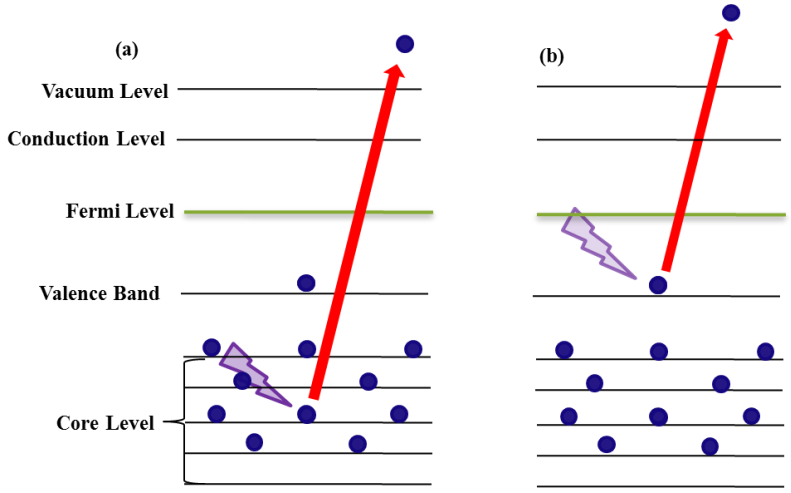

Figure 2.1: Photon-electron interaction with (a) X-ray and (b) UV radiation

XPS gives information about the core levels and valence level of elements, and the penetration depth is also more (approx. 10 nm with 1000 eV X-ray photons); whereas UV photoelectron spectroscopy (UVPES) gives the information about the valence band, and the penetration depth is very less, around 2 nm. Even though UVPES spectra are very complex, compared to the XPS spectra, but they are rich in information; often when the changes are subtle and limited to the top few layers, in phenomena such as heterogeneous catalysis, sensing, UVPES provides more information. Other reason being the different photoionization cross section (σ) for a particular valence orbital; for example, O 2p could be seen more prominently with UPS compared to XPS, due to high (10.67 Mb) and low σ (0.0005 Mb), respectively. By performing both XPS and UVPES, it is also easy to ascertain the origin of the energy level from a particular orbital of specific element. Photoelectron spectroscopy is traditionally an ultra-high vacuum technique. The photoelectron which is ejected from the sample should reach the detector without losing kinetic energy due to inelastic collision with atoms or molecules within the solid or with the residual gas molecules in the UHV environment; due to this it is necessary to maintain the ultra-high vacuum in the photoelectron

spectrometer. At high-pressure, electrons have very short mean free path (λ_e); for example, the mean free path of an electron having 400 eV kin etic energy in 1 mbar O_2 will be approximately 4 mm. So the main obstacle for photoemission at elevated pressures is the attenuation of electrons through inelastic scattering with gas phase molecules. This obstacle has been overcome in the development of photoelectron spectrometers which can function at near ambient pressures. A new term ambient pressure (AP) or near ambient pressure (NAP) or high pressure (HP) has been introduced with photoelectron spectroscopy (PES) to distinguish it from traditional UHV setups. In the last 20 years, NAPPES has emerged as an important investigating tool for many surface related phenomena like electrochemical reactions (Li-O_2 system), environmental chemistry (reaction under humid conditions, dissolved halide to gas reactions), and heterogeneous reactions on catalysts.[3] After the successful development of UHV XPS, the Kai Siegbahn's group shortly developed the NAPPES in early 1970's at Uppsala university.[4,5] Parallel efforts were made and another such system was installed in Cardiff University, UK at the end of 1070's, and used for the investigation of the solid-vapor interface. This system is equipped with several differential pumping stages between the sample chamber and hemispherical analyzer. This NAPPES system was developed by Roberts et al. for the measurement of solid/vapor interface at Cardiff University.[6] The new generation NAPPES is developed by the constant effort by many groups around the globe. Probably, Roberts's group from Cardiff University attempted for the first time and developed a high-pressure XPS analyzer to study the solid –gas interaction up to 1 mbar to bridge pressure gap but with limited success.[7] The major limitation of this system is the low resolution due to the lack of electrostatic lens system. Finally, it was successfully attempted by Salmeron's group at University of California, Berkeley[8] and Schlögl's group, Fritz-Haber Institute; Berlin.[9] These systems are designed for synchrotron radiation equipped differentially pumped electrostatic lenses and analyzer system. These electrostatic lenses increase the collection efficiency of electron counts to analyzer resulting in the high-resolution spectra. Later on several state of-the-art lab-based and synchrotron NAPPES have been developed summarized in Figure 2.2.[10] The basic design and principle of lab-based and synchrotron NAPPES system is similar; the only difference is the radiation source. In the lab-based system the Al or Mg

anode is used as an X-ray source. Whereas, in synchrotron source the charged particles are accelerated perpendicular their velocity, these particle produce the radiation with all energies and required energy radiation is used as X-ray source. There are limited availability of synchrotron sources and demand is very high, therefore several lab-based- NAPPES successfully installed equipped with modern state of the art high-pressure analyzers,[11-18] which are capable of operating up to 30 mbar pressure.[12] Several technical aspects which are very important in APPES are briefly described in the next section.

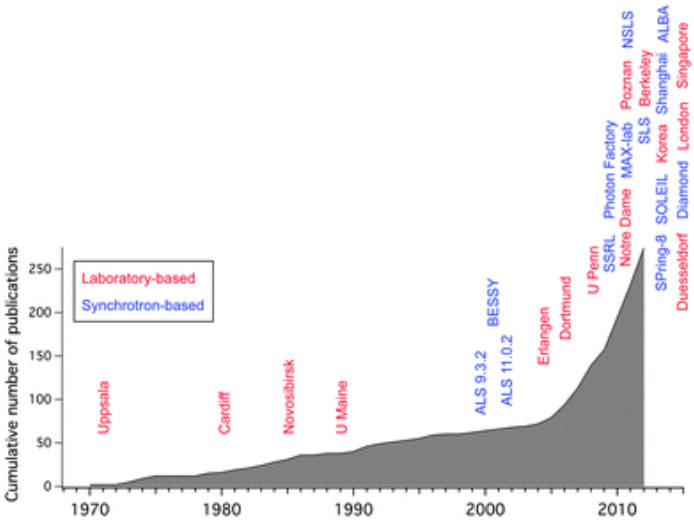

Figure 2.2: Ambient pressure XPS timeline, showing both the cumulative number of publications and the installation of new instruments. Red labels denote laboratory-based systems, and blue labels for synchrotron-based instruments. The dates for the installation of the instruments are approximate and to the best of our knowledge. (from reference 10, copyright permission obtained from RSC publication)

2.2 Development of NAPPES, Challenges and Solution

2.2.1 Electron – Gas Inelastic scattering:

The main challenge of NAPPES is the loss of kinetic energy and scattering of photoelectron because of inelastic and elastic collisions between the electron and gas molecules. The elastic scattering contribution in signal attenuation at electron kinetic energy below 100 eV and inelastic scattering dominate in signal attenuation with electron having high kinetic energy,

> 100 eV. The attenuation of the photoelectron signal follows Beer's law:-

$$I = I_o e^{(-z\sigma(KE)p/kT)} \qquad \text{Eq- 2.2}$$

Here I is the intensity of the signal at pressure p; I_o is the intensity of the signal in UHV; σ(KE) is the electron scattering cross section; and z is the distance traveled by an electron at gas pressure p and T temp. It means the intensity of the signal is inversely proportional to the distance (z) traveled by the electron at pressure p. A minimum distance between the sample surface and the front cone aperture, attached to the electrostatic lens region (or simply electron collection region and attached to differential pumping setup), will help to increase the electron counts (Figure 2.3). Generally, the distance between sample and cone/aperture is >D (D is the diameter of the cone). To minimize the elastic collision probability, cone aperture diameter (D) could be fixed smaller than the X-ray spot size. The smaller size of cone

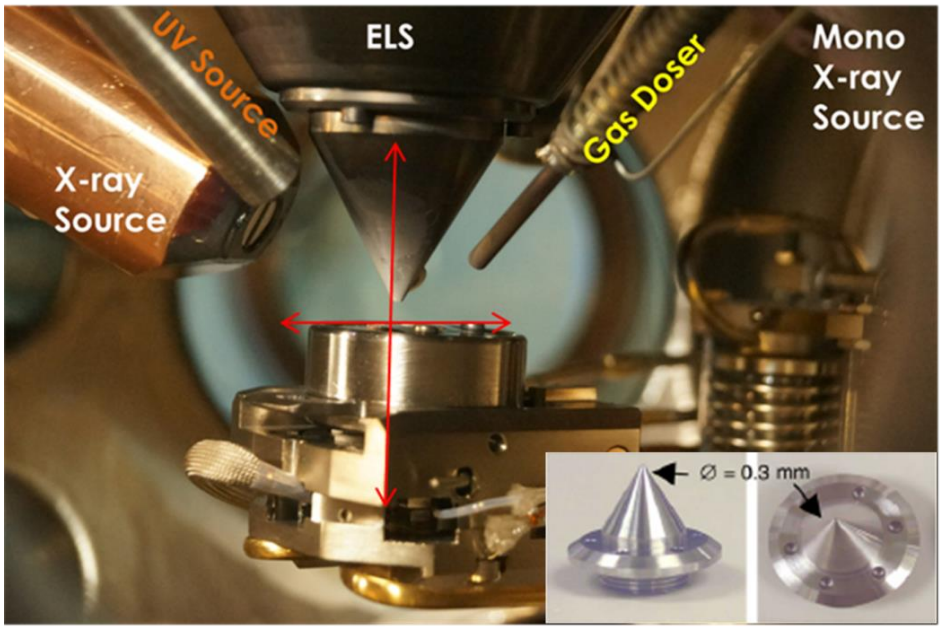

Figure. 2.3: Photograph of the open-reactor design employed in NAPPES unit. The sample holder is stationed on 4-axis manipulate which provide movement of sample holder in x, y, and z direction with 360^o rotation. In inset, the analyser cone image is shown with 0.3 mm diameter. Gas doser can be heated to heat the input gas to minimize the temperature difference between spectral measurement and gas temperatures. (from reference 18, copyright permission obtained from ACS).

aperture is also helpful to improve the differential pumping (explained in the next section), but decreasing the cone diameter will also decrease the electron counts reaching the detector. In fact, a pressure higher than 1 mbar is critically achieved by decreasing the aperture size. The feasible solution for this problem is to increase the X-ray flux in a small area, but it can cause sample damage. Another way to get better electron counts without increasing the cone size or X-ray flux is the use of electrostatic focusing lens in each differential pumping stage (Figure. 2.4). These lenses makes possible the collection of substantially a larger fraction of electrons which were scattered because of diverging nature of their trajectories and small solid angle captured by the apertures separating the pumping stages. These electrostatic lenses are first time used in the NAPPES developed by ALS, Berkeley in 1991-2002.[8]

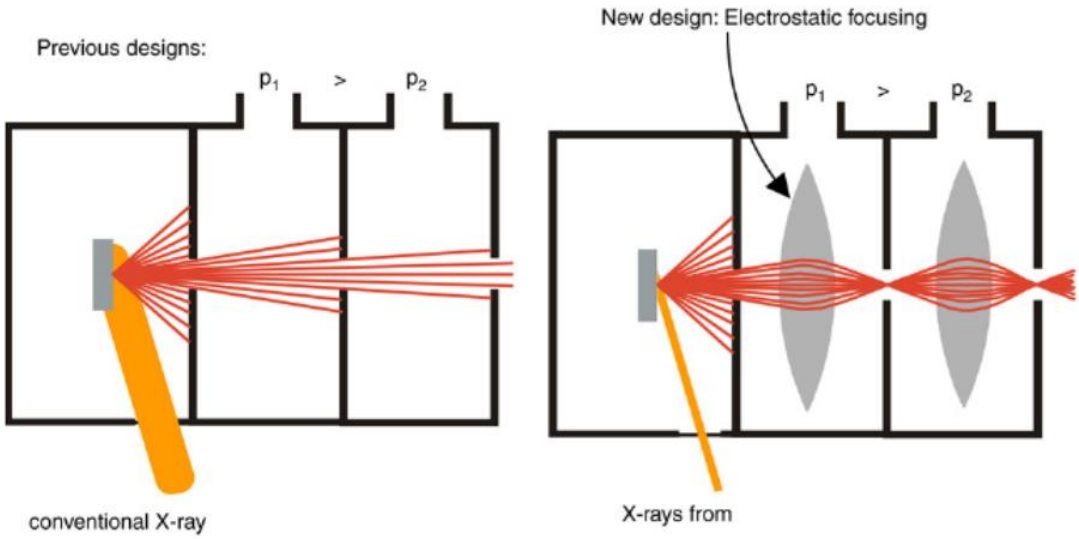

Figure 2.4: Traditional design of differential pumping (left) and modern design of differential pumping with electrostatic lens (Right)

2.2.2 Gas flow, Differential Pumping and Membrane-Based Setup

It has already been mentioned that at high pressure the electrons mean free path is very short and it is also necessary that it is essential to maintain high vacuum towards the electron energy analyzer (< 10^{-7} mbar) during the course of any measurement, which limits the application under ambient pressure. These considerations led to design a multistage pumping

system between sample, electrostatic lens region and the hemispherical electron energy analyzer. Each differential pumping stage is effectively creating a pressure difference of two-three order of magnitude from the earlier pumping state and depending on the type of gas, aperture size and pump capacity. Therefore several differential pumping stages are required if the sample is measured to be in high-pressure condition. A minimum of three differential pumping stages with sufficiently high pumping capacity is considered to maintain an increasingly better vacuum at each stage from sample surface to analyzer. The basic scheme of differential pumping pioneered by the Seighbahn et. al.[4,5] is used in the modern NAPPES system. Where the sample is located in the *in situ* analysis chamber and placed close to the differentially pumped aperture. Since the pressure distribution is not homogenous close to the aperture, the distance between sample and analyzer aperture should always be significantly greater than the diameter of the analyzer aperture. Figure 2.5 shows the schematic representation of variety of differential pumping stages, which are being used in NAPPES system around the globe.[10] When the electron enters the analyzer path it feels higher and higher vacuum through the differential pumping stages. This differential pumping combined with the electrostatic lens improves the signal to noise ratio.

Another way to avoid the gas-electron collision is the membrane. In this approach, the sample is placed in a vacuum sealed membrane. These membranes exhibit electron permeable but liquid-gas impermeable characteristics. These membranes are made by the carbon foils, a graphene sheet, and silicon nitride and mainly used in X-ray absorption spectroscopy and microscopy applications.[19-21] Among them silicon nitride membrane is very popular because of their easier synthesis, handling, very robust and homogenous in composition and thickness. Additionally, the liquid can also flow for liquid reactions in the cell as well the electron can be integrated with silicon chip for electrochemical measurement.[21,22] However, for photoelectron spectroscopy applications, these membranes must be sufficiently transparent for the low kinetic energy electrons and it should withstand high pressure difference. For example, 10 nm thick Si_3N_4 film can maintain the 1 bar pressure and it is permeable for electron having kinetic energy in few keV.[23,24] Therefore, the Si_3N_4 cannot use for soft X-ray spectroscopy where the K.E. of ejected electron is in range of 100-1000 eV. Graphene oxide,

graphene and hexagonal boron nitride show very good transparency for low K. E. electron. The graphene attracted more attention for *insitu* cell in photoelectron spectroscopy because of its mechanical strength and transparency for low kinetic energy electron. A single layer of graphene has shown 50% transparency for electrons with kinetic energy 1070 eV at an emission angle 60^0.[25] There are several reports are available where graphene is used for the fabrication of *insitu* cell for NAPPES.[26] However, all these developments are still at the laboratory levels and robust membranes are yet to be demonstrated for its stability under variety of conditions.

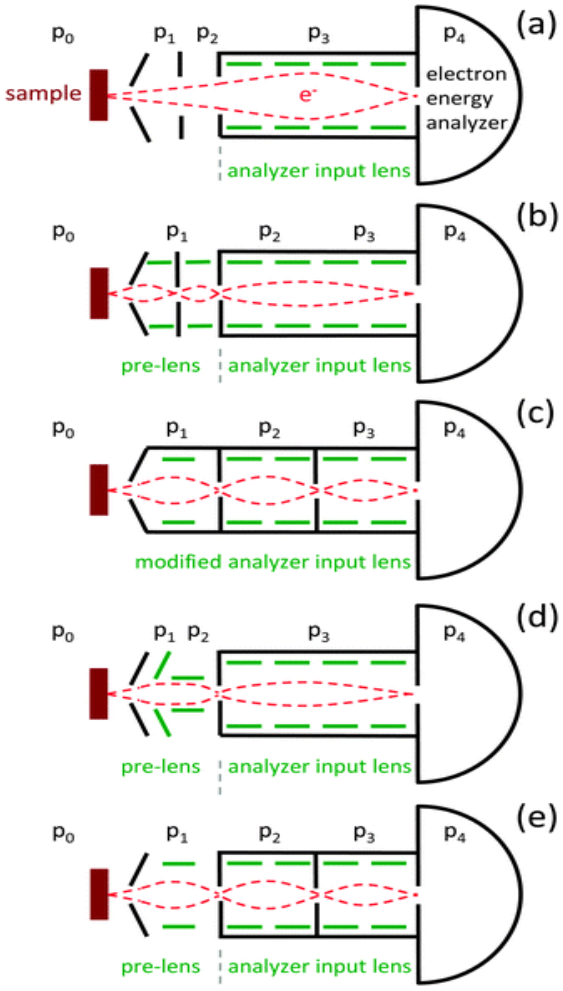

Figure 2.5: The schematic representation of differential pumping stages, which are used in NAPPES system around the globe (from reference 10, copyright permission obtained from RSC publication)

2.2.3 In situ Reaction Chamber

The advancement of differential pumping and photon source also increase the NAPPES user base. In modern science the NAPPES is playing an indispensable role in the chemical, biological and physical sciences. Therefore, it is necessary to precisely control the sample environment (Like, temperature, pressure, composition irradiation with another source like UV, IR etc) according to reaction requirement. Most of the NAPPES system has open reaction chamber as shown in the Figure 2.6(a) and 2.3. These types of reaction chambers have a large volume and large internal wall area. Because of the large area this chamber can accommodate various another radiation source like UV, mass spectrometer, sputter gun etc. and the sample in and out transfer is also very easy. This design also provides the homogenous distribution of gas pressure around the sample. The biggest disadvantage of this design is the quick switch to UHV from elevated pressure. This obstacle is overcome by the different design where a new *insitu* cell is in the vacuum chamber and sealed against it during the exposure of the sample to the gaseous environment as shown in Fig. 2.6 (b). This design

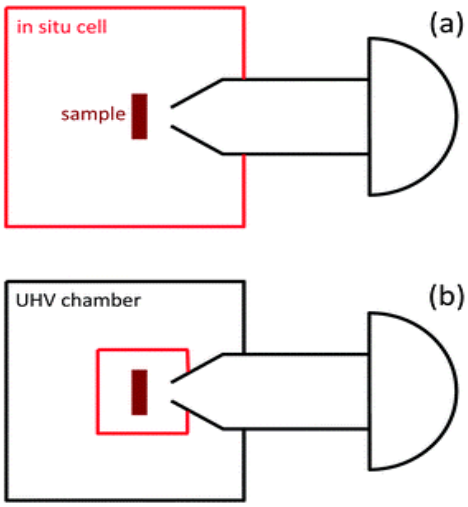

Figure 2.6: *In situ* reaction chamber design schematic. (a) Open reaction cell (b) in situ closed reaction cell is located inside a larger vacuum chamber (from reference 10, copyright permission obtained from RSC publication)

enables to quick switching between UHV and high-pressure as well as also reduced exposed chamber volume for high pressure. However, this is a more complex design and requires

precise manipulation to safely transfer the sample into the reaction cell. In addition, hardly any sample manipulation is possible within the high pressure area in the closed reactor design.

2.2.4 X-ray Windows and Photon-Gas Interaction

The X-ray source in NAPPES set up is generally separated from the high-pressure chamber by a thin membrane (50-100 nm). This is mainly to minimize the photon absorption by high pressure environment employed under NAPPES measurement conditions. Generally silicon nitride (Si_3N_4) and aluminum foil are used, because they have low X-ray absorption coefficient and they are X-ray transparent. However, the photon-gas interaction is weaker than electron- gas interaction and photon-gas scattering cross section is also very less. However, X-rays ionize the gas phase molecules in the analysis chamber, and the gas phase signal can be obtained as well. If the NAPPES measurements are made in a wide pressure range, it is suggested to measure the X-ray flux at different pressures to know the decrease in photon flux. This measurement helps to normalize the intensity losses that would occur, especially, at high pressures. Nonetheless, these gas phase signals indirectly help to determine the ϕ of the solid surfaces in operando condition.[27-31] It is also to be mentioned that gas-phase features can be observed at significantly high pressures around $1x10^{-3}$ mbar and above.

2.3 Angle Dependent X-ray Photoelectron spectroscopy

Angle dependent XPS is a corollary technique which is used to increase the surface sensitivity of the XPS method as well as to know the thickness of the surface layers, such as contamination, deposited layers. This is a nondestructive, highly sensitive technique which is used to determine the compositional variation of a sample from the surface to near surface region. Here the sample surface is tilted towards or away from the analyzer, which makes the less or more sensitive to surface or bulk (within the 10 nm probing depth of XPS). In other words, by changing the angle θ between sample surface normal and analyzer, it is possible to probe different depth from the top surface layers. This angle is called the emission angle or emission angle of photoelectron or take-off angle of photoelectron and denoted by α. To decrease the sampling depth, the take-off should be decreased as shown in Figure 2.7. The

relation between analysis depth and takeoff angle can be given as in equation 2.3.[32] While changing the sample angle θ the inelastic mean free path of the electron (IMPF) or attenuation length of the photoelectrons remains the same.

$$d_{av} = d \sin \alpha = d \cos \theta \qquad \text{Eq- 2.3}$$

d_{av} = The average sampling depth.

d = Maximum sampling depth at angle α,

When α or $\theta = 90^0$ then $d_{av} = d$.

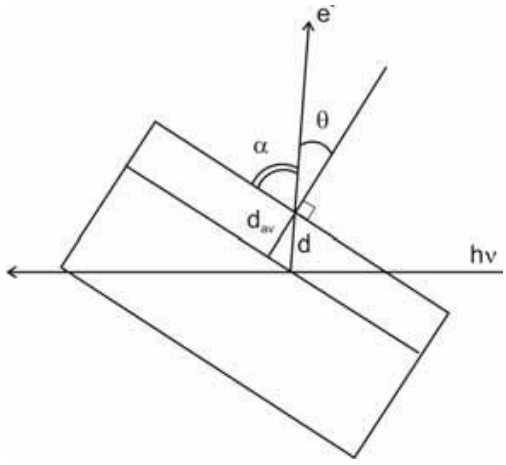

Figure 2.7: Surface sensitivity enhancement by variation of the electron take-off angle.

2.4 Inelastic Mean Free Path (IMFP) of Electrons in Solids

XPS and UPS are used for chemical analysis of surface and near surface region of solid. To determine the compositional variation of surface and near surface regions it is necessary to measure the electron sampling depth. This electron sampling depth can help to determine the role of each layer of sample in the XPS or UPS intensity or electron counts. The sampling depth can be derived from the IMFP values. IMFP could be defined as follows: how far an electron can travel through a thin film of a solid lattice or a near surface region of a solid before it encounters first inelastic collision either with solid atoms and/or gas-phase molecules. Any inelastic collision is known to decrease the kinetic energy of the electron and

after an inelastic collision it will contribute to the background, rather than to the particular energy level in the spectrum. It is also to be noted that very high kinetic energy electrons undergo less number of collisions than its counterpart with low kinetic energy. Background intensity in any typical XPS spectrum increases from low to high binding energy. Most reliable calculations, for IMFPs measurement for element inorganic compound and organic compound were already made by Seah and Dench.[33] The proposed equation for IMFPs by Seah and Dench as follows:-

For elements

$$\lambda m = \frac{538}{E^2} + 0.41(aE)^{\frac{1}{2}} \text{ Monolayer} \qquad \text{Eq. 2.4}$$

For inorganic compounds

$$\lambda m = \frac{2170}{E^2} + 0.72(aE)^{\frac{1}{2}} \text{ Monolayer} \qquad \text{Eq. 2.5}$$

For organic compounds

$$\lambda m = \frac{49}{E^2} + 0.11(aE)^{\frac{1}{2}} \text{ mg m}^{-2} \qquad \text{Eq. 2.5}$$

Here; λm = IMFPs in monolayer

E = Energies between 1 to 10000 eV above fermi energy

a = monolayer thickness in nm

2.5 Near Ambient Pressure Photoelectron Spectrometer at CSIR-NCL, Pune

2.5.1 System Overview

Figure 2.8 shows the image of NAPPES system installed in CSIR- National Chemical Laboratory, Pune. The system was fabricated and supplied by Prevac, Poland. It consists the four chambers, namely, (1) Load lock chamber (2) preparation and storage chamber (3) High-pressure reactor, and (4) Analysis chamber and VG Scienta R3000 three stage differential

pumping hemispherical analyzer. Analysis chamber is made of μ–metal, while other chambers are made of SS-316. All these four chambers are separated by the three manual gate valves. This system equipped with two X-ray sources, one is VG Scienta MX 650 Al kα monochromatic X-ray source and another is Al kα and Mg kα dual anode X-ray source; it yields photons of 1486.7 and 1253.6 eV, respectively, energy. It also equipped with one He-I and He-II ultra-violet (UV) radiation source. The excitation energy of He-I and He-II are 21.2 and 40.8 eV respectively. All radiation sources can work in UHV and high pressure conditions. The instrument is equipped with a gas-manifold with three mass flow controller systems, connected with a common gas mixing chamber, which enables mixing of up to three gases. The vacuum in the system is maintained by the various capacity turbomolecular pumps backed by rotary pumps. More details about the instrument is available in ref. 18.

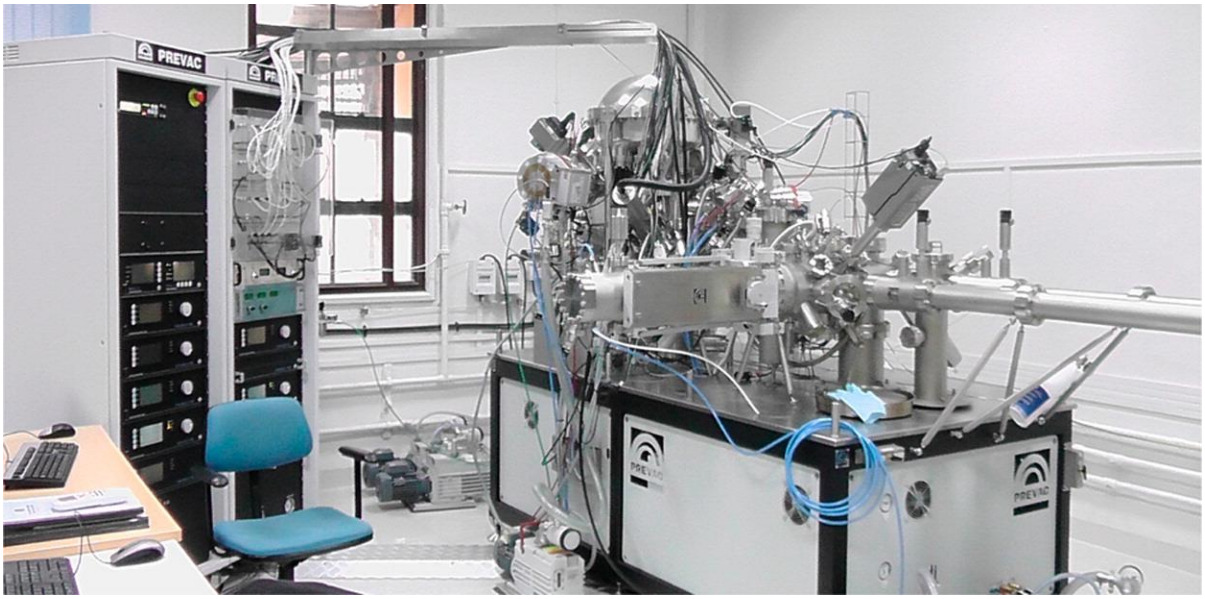

Figure: 2.8: Image of Lab- NAPPES instrument installed in CSIR- National Chemical Laboratory, Pune

2.5.2 Load lock and Preparation chamber

The system is equipped with a fast entry load lock system, where the vacuum is maintained by the 260 l/s HiPace300 Pfeiffer turbo molecular pump backed by the DUO 10M Pfeiffer double stage rotary vane pump. Load lock and preparation chamber is separated by a manual

gate valve from VAT. The load lock is fitted with a manual drive linear arm. With the help of this arm the sample is transferred from load lock to preparation chamber and then high-pressure reactor or analysis chamber. The preparation chamber is equipped with Ar-ion sputter gun (IS 40C1, Prevac) operating between 0 to 5 kV and 0 to 10 mA, quadrupole mass spectrometer (QMS) from SRS, RGA200 and 4-axis manipulator connected with sample heating and cooling system from 100 (liquid N_2 temperature) to 1023 K. The QMS is connected with the analysis chamber through leak valve to analyze the reactions products from the sample surface. The preparation chamber is pumped by the 355 L/s HiPace300 Pfeiffer turbo molecular pump backed by the DUO 20M Pfeiffer double stage rotary vane pump. The preparation chamber has a sample parking system, and up to 10 samples can be stored. The metal foils which are used in this thesis experiments are atomically cleaned by Ar-ion sputtering followed by vacuum annealing up to 1000 K.

2.5.3 Analysis chamber and Analyzer

The analysis or reaction chamber has an open cell design (Fig. 2.3). The design has been explained in section 2.4. The analysis chamber is pumped by two 355 L/s capacity HiPace300 Pfeiffer turbo molecular pump backed by the DUO 20M Pfeiffer double stage rotary vane pump and an ion pump. These pumping systems are efficient to fast switch between 1 mbar pressures to UHV (ultra-high vacuum) within 5 min. Inside view of the analysis chamber is shown in Fig. 2.9. The pressure of the analysis chamber is measured by the Oerlikon Leybold TTR 90 gauges and a BAG (Bayard-Alpert ionization gauge). One another CTR gauge is also fitted to measure the accurate pressure near the reaction zone i.e. close to the sample surface. The analysis chamber is equipped with a differentially pumped VG Scienta MX 650 Al kα monochromatic X-ray, Al kα and Mg kα dual anode X-ray. These X-ray sources are isolated with analysis chamber by a thin Al window. The differential pumping and Al window are keeping the radiation sources in UHV, even when the analysis chamber pressure is 1 mbar. The analysis chamber is also equipped with a UV source which can give stable He I and He II UV radiation for valence band photoelectron spectroscopy (UVPES) measurements under UHV as well as 1 mbar conditions. The water-cooled UV source is mounted on a CF40 flange which can give an emission current up to 100 mA for He I and 200 mA for He II. An electron

flood source operating between 0 and 500 eV for charge compensation during XPS operation is attached to the analysis chamber. A gas mixing manifold equipped with the mass flow controllers, which is useful to mix three gases to the desired composition to simulate the reaction condition. This gas mixing manifold is connected with gas doser via a z-axis manipulator in the analysis chamber. Further, the gas doser can be heated up to 873 K to heat the input gas for high temperature experiments. The sample is stationed on a 4 axes manipulator with the capability of 360^0 rotation of sample. This 360^0 rotation of sample is helpful to carry out the angle-dependent experiments to depth profiling of the sample.

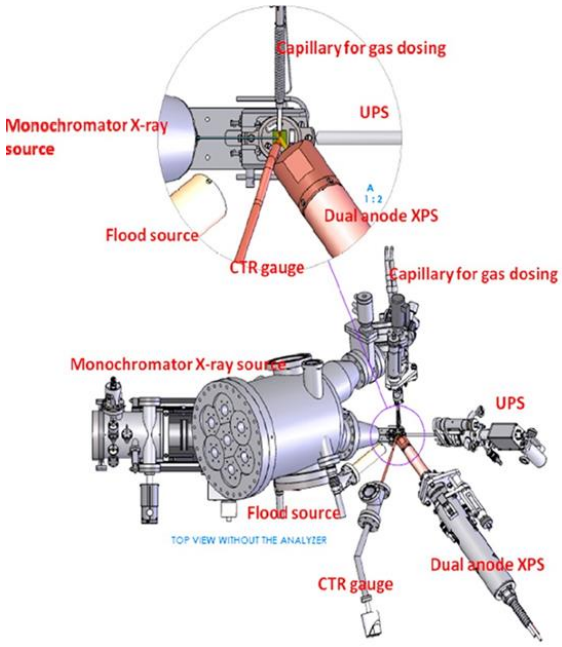

Figure 2.9: The schematic view of the analysis chamber without analyzer. The inset shows an expanded view of the analysis spot. (from reference 18, copyright permission obtained from ACS publication)

The analyzer is the heart of the XPS system. There are various designs of high-pressure analyzers are developed, which is explained in section 2.2.2. This NAPPES system is equipped with the VG Scienta R3000HP analyzer. The loss of electron K.E. due to the inelastic collision between electron and gas molecules is major problem in NAPPES. To minimize the probability of inelastic collisions there are three parameters are adopted in the R3000HP analyzer. First, the sample is kept close to the cone of ELR (electrostatic lens

region, where effective differential pumping is started). It has been already explained that at 1 mbar pressure the electron can travel a maximum up to 4 mm without an inelastic collision. The open reaction chamber and 4 axes manipulator allow varying the distance between the sample and analyzer cone from 0.5 mm to few mm according to pressure requirements. Once the electron enters in the ELR region, there are two factors contribute to getting the high-quality spectra at high pressure, effective differential pumping and converging of electron in ELR region. Total three differential pumps are fitted in the analyzer; first and second differential pumps are fitted in ELR region and third differential pump is in the electron energy analyzer (EEA) as shown in Fig 2.9. At 1 mbar N_2 pressure, a vacuum of 5×10^{-4}, 10^{-6}, and 10^{-7}-10^{-8} mbar is maintained in the first, second and third differential pumping sections, respectively. First, second, and third differential pumping regimes are pumped down by a combination of 400, 300, and 400 L/s turbomolecular pumps, backed by rotary pumps.

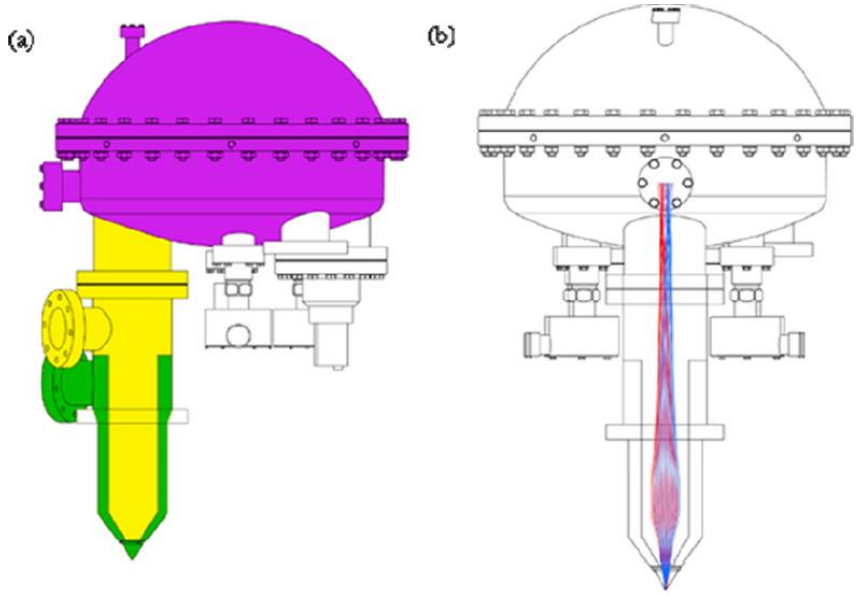

Figure 2.10: Double front cone pumping arrangement (shown in green and yellow) effectively improves the differential pumping to minimize inelastic scattering in electrostatic lens regime (ELR) as well as to decrease the data collection time under high-pressure conditions. The electron energy analyzer region is shown in purple. (b) A schematic of the aperture free ELR and the electron trajectory for faster data acquisition. (from reference 18, copyright permission obtained from ACS publication)

The area of pumping is gradually increased from first to second ELR to EEA. Further, a double front cone pumping arrangement design is adopted which help to decrease the pressure with a steep pressure gradient from the bottom of the cone (which is very close to the sample surface) to the EEA. This differential pumping arrangement helps to minimize the inelastic collision in ELR region. In contrast to conventional analyzers,[15] (Figure 2.2) in R3000HP aperture free electrostatic lens design is adopted and the voltage is applied in such a way that they converge all electrons. Apart from the advanced design of analyzer there are other critical aspects are also incorporated. An exchangeable *analyzer* cone with different aperture size from 0.3 to 5 mm. Currently, the analyzer is fitted with 1.2 mm aperture and data reported in this thesis are obtained with this aperture. A distance of 1.5 mm is maintained between sample surface and aperture for all the data collected and reported in this thesis. The highest resolution achieved is 0.42 ± 0.02 eV with 50 eV pass energy at a (analyzer entrance) slit width of 0.2 mm, and it is in good agreement with that reported for the R3000HP by Mangolini et al.;[15] however, the resolution measured is 0.6 ± 0.02 eV with the maximum slit width of 3.0 mm of the analyser.

The XPS and UPS analysis at near ambient pressures was carried out on the special sample holders supplied by Prevac, Poland. PTS 1000 Res for UHV heating, and PTS 700 HPC res. have been used for 1 mbar experiments and temperature is measured by c/k type thermocouple. Both sample holders are based on resistive heating. The PTS700 HPC sample holder also has the cooling assembly which allows cooling down the sample up to 100 K. The sample has two potential contacts. The potential contact can be connected from outside by a multimeter through the electrical feedthrough on manipulator. These feedthroughs allow apply the required voltage, current and measuring the voltage and current created on sample holder due to gas ions. For this thesis work, the Keithley 2700 multimeter is used for applying the voltage/current on sample. PTS700 sample holder can be used up to 1 mbar and 1023 K. For high temperature measurement the system is equipped with electron beam heating and the sample can heated up to 2273 K; however this is applicable only in UHV conditions.

2.6 References.

1.Siegbahn, K.; Edvarson, K., β-Ray Spectroscopy in the Precision Range of 1: 105. *Nuclear Physics* **1956,** *1,* 137-159.

2. Siegbahn, K., Electron spectroscopy for atoms, molecules, and condensed matter. Rev. Mod. Phys. **1982**, *54*, 709.
3. Salmeron, M.; Schlögl, R., Ambient pressure photoelectron spectroscopy: A new tool for surface science and nanotechnology. *Surf. Sci. Rep*. 2008, *63*, 169-199.
4. Siegbahn, H., Electron spectroscopy for chemical analysis of liquids and solutions. *J. Phys. Chem.* **1985**, *89*, 897-909.
5. Siegbahn, H.; Siegbahn, K., ESCA applied to liquids. *J. Electron. Spectrosc. Relat. Phenom.* **1973,** *2*, 319-325.
6. Joyner, R. W.; Roberts, M. W.; Yates, K., A "high-pressure" electron spectrometer for surface studies. *Surf. sci.* **1979,** *87***,** 501-509.
7. Bradshaw, A.; Menzel, D., Photoelectron Spectroscopy and Surface Chemistry. In *Topics in Surface Chemistry*, Springer: **1978**, 225-259.
8. Ogletree, D. F.; Bluhm, H.; Lebedev, G.; Fadley, C. S.; Hussain, Z.; Salmeron, M., A differentially pumped electrostatic lens system for photoemission studies in the millibar range. *Rev. Sci. Insrtum.* **2002,** *73*, 3872-3877.
9. Bluhm, H.; Hävecker, M.; Knop-Gericke, A.; Kleimenov, E.; Schlögl, R.; Teschner, D.; Bukhtiyarov, V. I.; Ogletree, D. F.; Salmeron, M., Methanol oxidation on a copper catalyst investigated using in situ X-ray photoelectron spectroscopy. *J. Phys. Chem. B* **2004,** *108*, 14340-14347.
10. Starr, D.; Liu, Z.; Hävecker, M.; Knop-Gericke, A.; Bluhm, H., Investigation of solid/vapor interfaces using ambient pressure X-ray photoelectron spectroscopy. *Chem. Soc. Rev.* **2013,** *42*, 5833-5857.
11. Jürgensen, A.; Esser, N.; Hergenröder, R., Near ambient pressure XPS with a conventional X-ray source. *Surf. Interface Anal.* **2012,** *44*, 1100-1103.
12. Newberg, J. T.; Åhlund, J.; Arble, C.; Goodwin, C.; Khalifa, Y.; Broderick, A., A lab-based ambient pressure x-ray photoelectron spectrometer with exchangeable analysis chambers. *Rev. Sci. Instrum*. **2015**, *86*, 085113.
13. Eriksson, S. K.; Hahlin, M.; Kahk, J. M.; Villar-Garcia, I. J.; Webb, M. J.; Grennberg, H.; Yakimova, R.; Rensmo, H.; Edström, K.; Hagfeldt, A., A versatile photoelectron spectrometer for pressures up to 30 mbar. *Rev. Sci. Instrum.* **2014**, *85*, 075119 (1-11).

14. Bukhtiyarov, V.; Kaichev, V.; Prosvirin, I., X-ray photoelectron spectroscopy as a tool for in-situ study of the mechanisms of heterogeneous catalytic reactions. *Top. Catal.* **2005**, *32*, 3-15.
15. Mangolini, F.; Åhlund, J.; Wabiszewski, G. E.; Adiga, V. P.; Egberts, P.; Streller, F.; Backlund, K.; Karlsson, P.; Wannberg, B.; Carpick, R. W., Angle-resolved environmental X-ray photoelectron spectroscopy: A new laboratory setup for photoemission studies at pressures up to 0.4 Torr. *Rev. Sci. Instrum.* **2012**, *83*, 093112.
16. Pantförder, J.; Pöllmann, S.; Zhu, J.; Borgmann, D.; Denecke, R.; Steinrück, H.-P., New setup for in situ x-ray photoelectron spectroscopy from ultrahigh vacuum to 1 mbar. *Rev. Sci. Instrum.* **2005**, *76*, 014102.
17. Jackman, M. J.; Thomas, A. G.; Muryn, C., Photoelectron spectroscopy study of stoichiometric and reduced anatase TiO2 (101) surfaces: the effect of subsurface defects on water adsorption at near-ambient pressures. *J. Phys. Chem. C* **2015**, *119*, 13682-13690.
18. Roy, K.; Vinod, C.; Gopinath, C. S., Design and performance aspects of a custom-built ambient pressure photoelectron spectrometer toward bridging the pressure gap: Oxidation of Cu, Ag, and Au surfaces at 1 mbar O_2 pressure. *J. Phys. Chem. C* **2013,** *117*, 4717-4726.
19. Drake, I. J.; Liu, T. C.; Gilles, M.; Tyliszczak, T.; Kilcoyne, A. D.; Shuh, D. K.; Mathies, R. A.; Bell, A. T., An in situ cell for characterization of solids by soft x-ray absorption. Review of Scientific Instruments **2004**, *75*, 3242-3247.
20. Fuchs, O.; Zharnikov, M.; Weinhardt, L.; Blum, M.; Weigand, M.; Zubavichus, Y.; Bär, M.; Maier, F.; Denlinger, J.; Heske, C., Isotope and temperature effects in liquid water probed by X-ray absorption and resonant X-ray emission spectroscopy. *Phys. Rev. lett* **2008,** *100*, 27801-27804
21. De Jonge, N.; Ross, F. M., Electron microscopy of specimens in liquid. *Nat. Nanotechnol.* **2011,** *6*, 695-704
22. De Jonge, N.; Peckys, D. B.; Kremers, G.; Piston, D., Electron microscopy of whole cells in liquid with nanometer resolution. *Proc. Natl. Acad. Sci. U.S.A.* **2009**, 0809567106 (1-6)

23. Masuda, T.; Yoshikawa, H.; Noguchi, H.; Kawasaki, T.; Kobata, M.; Kobayashi, K.; Uosaki, K., In situ x-ray photoelectron spectroscopy for electrochemical reactions in ordinary solvents. *Appl. Phys. Lett.* **2013,** *103*, 111605.
24. Tsunemi, E.; Watanabe, Y.; Oji, H.; Cui, Y.-T.; Son, J.-Y.; Nakajima, A., Hard x-ray photoelectron spectroscopy using an environmental cell with silicon nitride membrane windows. *J. Appl. Phys* **2015**, *117*, 234902.
25. Kolmakov, A.; Gregoratti, L.; Kiskinova, M.; Günther, S., Recent approaches for bridging the pressure gap in photoelectron micro spectroscopy. *Top. Catal*. **2016**, *59*, 448-468.
26. Weatherup, R. S.; Eren, B.; Hao, Y.; Bluhm, H.; Salmeron, M. B., Graphene membranes for atmospheric pressure photoelectron spectroscopy. *J. Phys. Chem. lett.* **2016**, *7*, 1622-1627.
27. Reddy, K. P.; Mhamane, N. B.; Ghosalya, M. K.; Gopinath, C. S., Mapping Valence Band and Interface Electronic Structure Changes during Oxidation of Mo to MoO_3 via MoO_2 and MoO_3 Reduction to MoO_2: A NAPPES Study. *J. Phys. Chem*. *C* **2018** *122* 23034–23044
28. Ghosalya, M. K.; Reddy, K. P.; Jain, R.; Roy, K.; Gopinath, C. S., Subtle interaction between Ag and O2 : a near ambient pressure UV photoelectron spectroscopy (NAP-UPS) investigations. *J. Chem. Sci.* **2018**, 130, 30.
29. Ghosalya, M. K.; Jain, R.; Reddy, K. P.; Gopinath, C. S., Silicon Oxidation by NAPPES: From Dangling Bonds to Oxygen Islands to 2D SiOx Layer to the Onset of Bulk SiO2 Formation. *J. Phys. Chem. C* **2018,** *122*, 4331-4338.
30. Jain, R.; Gnanakumar, E. S.; Gopinath, C. S., Mechanistic Aspects of Wet and Dry CO Oxidation on Co_3O_4 Nanorod Surfaces: A NAP-UPS Study. *ACS Omega* **2017**, *2*, 828-834.
31. Axnanda, S.; Scheele, M.; Crumlin, E.; Mao, B.; Chang, R.; Rani, S.; Faiz, M.; Wang, S.; Alivisatos, A. P.; Liu, Z., Direct work function measurement by gas phase photoelectron spectroscopy and its application on PbS nanoparticles. *Nano let.* **2013**, *13*, 6176-6182.
32. Merzlikin, S., Depth Profiling by X-ray Photoelectron Spectroscopy. *Fakultät für Chemie* **2007**.
33. Seah, M. P.; Dench, W., Quantitative electron spectroscopy of surfaces: A standard data base for electron inelastic mean free paths in solids. *Surf. Inter. Anal.* **1979,** *1*, 2-11.

Chapter 3a

Subtle interaction between Ag and O_2: a near ambient pressure UV photoelectron spectroscopy (NAP-UPS) investigations

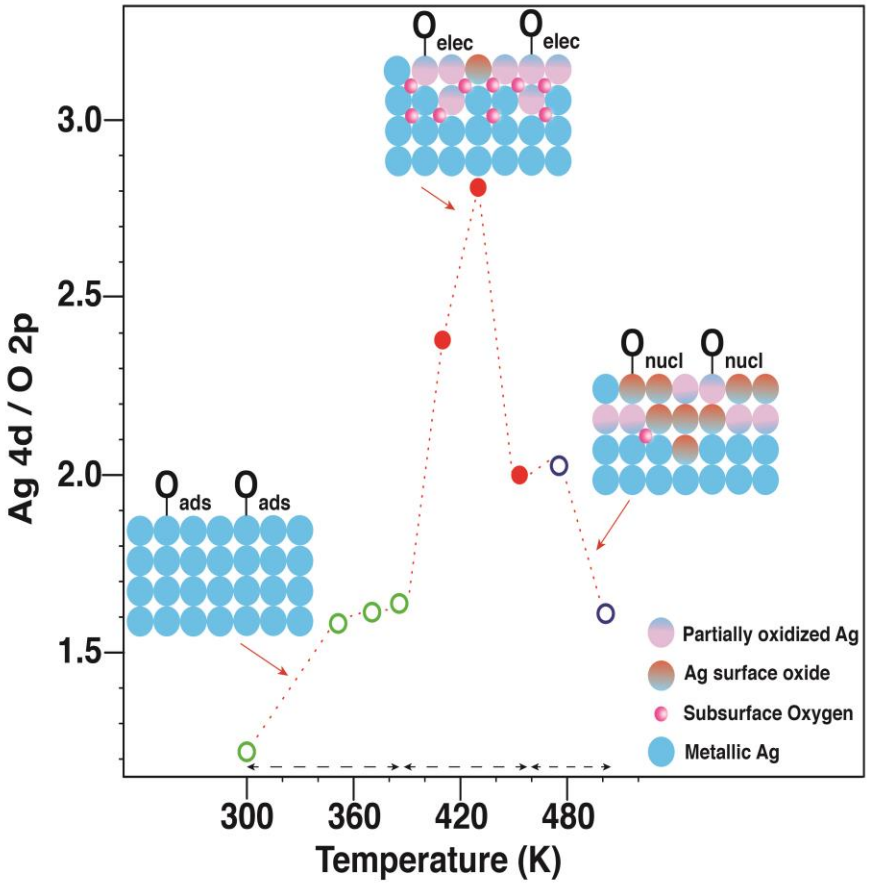

A part of the work presented in chapter 3.1 has been published, and publication detail is:-

Ghosalya, M. K.; Reddy, K. P.; Jain, R.; Roy, K.; Gopinath, C. S., Subtle interaction between Ag and O_2 : a near ambient pressure UV photoelectron spectroscopy (NAP-UPS) investigations. *J. Chem. Sci.* **2018**, 130, 30.

3.1 Introduction

Silver is a unique catalyst for two technologically important partial oxidation reactions, namely, ethylene to ethylene oxide (EtO) and methanol to formaldehyde production.[1–3] Ethylene to EtO conversion mostly takes place on supported silver catalysts. It was discovered by Emile in 1931.[4] EtO is a versatile intermediate chemical for the production of ethylene glycol, glycol ethers, etc. which are used in the production of detergent and surfactant, anti-freezing agent, coolant etc. Ag supported on α-Al_2O_3 is being used as a catalyst for EtO production with 40 to 50 % selectivity. However, the addition of promoters such as chlorine, alkali or alkaline earth metal increases the selectivity up to ~80%.[3,5]Around 15 MT EtO was produced on 2010 on chlorinated hydrocarbon promoted Ag/α-Al_2O_3 at 10 to 30 bar pressure between 450 and 520 K.[6] Even 1 % improvement in the EtO selectivity could save several millions of dollars per year. Many efforts are under way to optimize the reaction conditions and the catalyst to improve the selectivity.

Ethylene to EtO is a kinetically controlled selective oxidation.[1,6] Despite being more prone to combustion than ethylene, EtO formation is high, but in a narrow temperature regime (430–500 K). Oxygen interaction with silver has a crucial role in controlling the EtO selectivity. For the last fifty years, theoretical[7-9] and experimental[11-13] investigations led to various models of Ag-O_2 interaction to explain its role in the partial oxidation reactions catalyzed by silver; however, the mechanism still remains debated, particularly regarding the nature of oxygen involved in the activation of ethylene and the nature of silver surfaces under reaction conditions.[8,14–18] The process of EtO (or any epoxide) formation, which involves the insertion of oxygen into the π-bond of ethylene (alkene) molecule, requires a 'special' oxygen which can activate the alkene.

Campbell et al.,[19,20] studied ethylene epoxidation by varying four reaction parameters like the temperature, the partial pressure of oxygen and ethylene, and surface oxygen coverage (θ_O), and a reaction model was proposed. It suggests that under isothermal conditions, θ_O plays the major role in the epoxide selectivity. Theoretical calculations by van Santen et al.,[1,17] shows that dissolved O-atoms in the subsurfaces of Ag is responsible for epoxidation over complete combustion by Ag catalysts. The presence of dissolved oxygen species in the subsurfaces of Ag facilitates, (a) the reduction in bond energy of adsorbed

oxygen on silver, and (b) modifies the repulsion of adsorbed oxygen atoms and adsorbed ethylene into an attractive one. According to thermodynamic studies, the active oxygen species in ethylene epoxidation over Ag catalysts is a weakly bound species under steady-state conditions,[1,8] and in situ techniques are indispensable for its detection. A series of articles[6,7,12,14] on in situ characterization are available that reports the nature of active species, oxygen adsorption site, and reaction intermediates. XPS studies under in situ conditions are available in the identification of the active oxygen species. Bukhtiyarov et al., reported that electrophilic and nucleophilic oxygen species are present on the catalytically active surface under epoxidation conditions.[14] In the O 1s spectra, the components at 528.5 and 530.2 eV B.E. were attributed to the nucleophilic and electrophilic oxygen, respectively. The nucleophilic oxygen leads to the total combustion of ethylene, whereas the electrophilic oxygen is active for partial oxidation. The nature of nucleophilic oxygen was studied earlier,[21] whereas the role of electrophilic oxygen is inconclusive. The fact is that even the NAP-XPS measurements carried out so far were not able to detect any charge transfer between Ag and O.[7,14] In fact, Ag 3d core level shows no change in the present and earlier studies. However, probing the VB with low energy photons (He- I source; $h\nu = 21.2$ eV) reveals many crucial changes in Ag-O_2 interaction, which otherwise remain untraced in core level XPS.

VB photoelectron spectroscopy with low energy photons is an important tool to access mostly surface specific electronic changes. Indeed, NAP-UPS is fully relevant to explore silver-oxygen interaction, since Ag 4d and O 2p orbitals exhibit high photoionization cross sections (σ) of 16.62 and 10.67 Mb, respectively, with He-I (21.2 eV) photon.[22] The changes observed with He-I excitation is not possible to detect with Mg or Al Kα, due to, (a) three to five order of magnitude smaller σ for Ag 4d (0.1030 with 800 eV; 0.021 Mb with Al Kα photons), and O 2p (0.0022 with 800 eV; 0.00024 Mb with Al Kα photons); (b) low resolution of X-ray; and (c) comparatively high probing depth of X-ray photons. Earlier VB studies on Ag were carried out in vacuum[23,24] or at low pressure ($\leq 10^{-4}$ mbar),[25] whereas NAP-UPS is able to measure under more practical in situ conditions. In situ NAPUPS analysis provides the information about the work function (ϕ), E_F, chemical bonding, etc. This information is very important to determine the nature of oxygen present on the Ag surfaces under high pressure conditions. In the present work, the NAP-XPS and NAP-UPS data was

employed to understand the silver-oxygen interaction and subsequent electronic structure changes in the critical epoxide formation temperature conditions. Three temperature regimes have been identified, and the silver-oxygen interaction changes drastically from one to another regime. Present NAP-UPS analysis provides the direct evidence of subtle Ag – O_2 interaction in the active temperature window of 390–450 K for epoxidation. As the temperature reaches 390 K, the oxygen begins to diffuse into the subsurface layers of Ag, which makes the silver surface marginally cationic and it is confirmed from the ϕ change as well as angle-dependent NAP-XPS. It has also been observed that between 390 to 450 K, the oxygen coverage on Ag surface decreased significantly, in spite of the presence of large excess of gas-phase oxygen (0.1 mbar). On the basis of these observations, it is suggested that the modified surface attract the electron-rich alkene molecules and facilitates alkene adsorption and subsequent epoxidation. The present study contributes significantly to understand the gas-solid interaction at several orders of pressure higher than the conventional surface science measurements at high vacuum (10^{-9} mbar) and hence closer to the actual conditions (10–30 bar).[26–34]

3.2. Experiment

A polycrystalline foil of Ag (purity 99.999%, MaTeck, Germany) was used for the present studies. The samples were cleaned by argon ion sputtering by applying a potential of 3 kV and an acceleration current of 6 mA to the sputter gun, followed by annealing at 1000 K. A series of sputter-anneal cycles produced clean silver surfaces. No contamination of oxygen and carbon was detected by XPS/UVPES. The impurity level of any sulfur, silicon, and phosphorous was lower than the detection limits of R3000 analyzer. Detailed O_2 Ag gas-solid interaction experiments were carried at 0.1 mbar oxygen (99.99%) partial pressure from RT (295 K) to 500 K. Similar but representative studies were carried out at 0.2 mbar O_2 pressure also. A cone with 1.2 mm aperture was fitted to the entrance column of the R3000HP analyzer, and a sample to aperture distance of 1.5mm was maintained for the present measurements. More details about NAPPES are available in chapter 2. The spectra were deconvoluted with Gaussian-Lorentzian type synthetic components after subtracting a Shirley type background in CasaXPS. All the spectra were calibrated with respect to the E_F of Ag. The spectra obtained at elevated pressures and temperatures were intensity-normalized with respect to the spectrum obtained under vacuum and at RT.

3.3. Results and Discussion

3.3.1 *Comparison of VB Spectra in UHV and at 0.1 mbar O_2*

Figure 3.1 shows the VB spectra of (a) a clean Ag surface recorded at RT (295K) in UHV and (b) in the presence of 0.1 mbar O_2. Gas-phase molecular oxygen recorded at RT is given for comparison in Figure 3.1c. Ag 4d band observed for clean silver has three distinct features

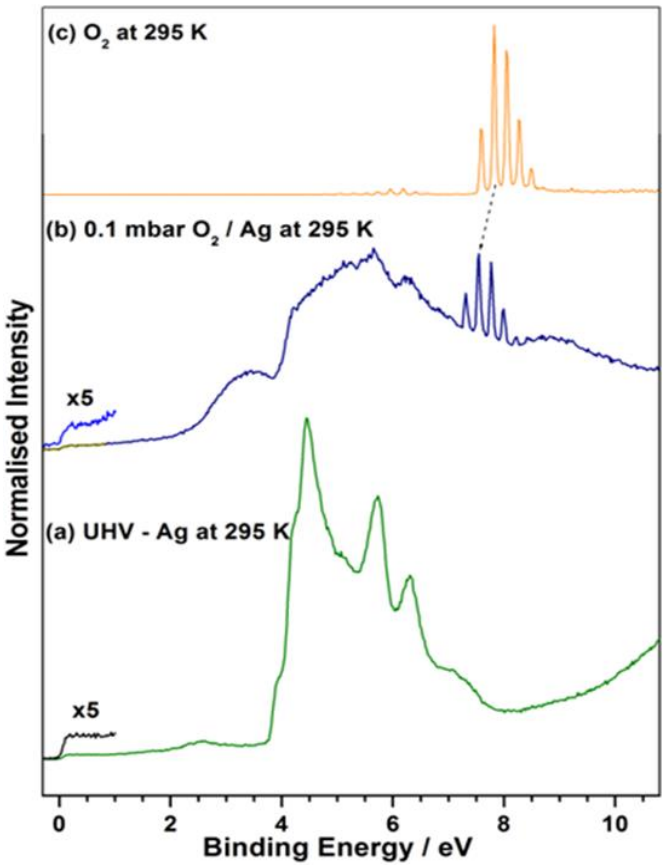

Figure 3.1: Valence band spectra of silver surface recorded. (a) in UHV, and (b) at 0.1 mbar O_2 partial pressure at RT. (c) Gas-phase molecular oxygen spectrum is given for comparison.

between 3.8 and 7 eV and metallic E_F feature at 0 eV; the spectrum is in good correspondence with that of reported in the literature.[24,35–37] The hump observed between 6.8 and 7.6 eV relates to the mixing of the density of states of Ag 4d and 5s orbitals; this is fully supported by the experimental XPS VB studies with high energy photons (hν = 7912 eV) in combination with DFT studies.[37] In fact, it is known that the outermost s orbitals of coinage metals penetrates so deep and hence it is worth exploring further;[38,39] however, early transition metals do not show this trend. A broad and low-intensity peak at ~2.6 eV is a satellite peak

due to the secondary He Iß radiation (excitation energy 23.06 eV).[40] The exposure to oxygen at 0.1 mbar pressure at 295K (Figure 3.1b) broadens the Ag 4d features to such an extent that only a single broad feature was observed without any fine structure (as on clean surface). In addition, a new and broad peak appeared between ~2.3 and 4.0 eV; indeed this feature was not present on the clean Ag surfaces. Dissociative adsorption of molecular oxygen occurs on the Ag surface at room temperature and forms the metal oxide pair. Oxygen covered islands are indicated to be present (discussed later) and lead to metal oxide pair. The new peak observed between 2.3 and 4 eV is due to the contribution from hybridization between O 2p antibonding and Ag 4d orbitals and assigned to π–antibonding orbital. Another low intensity and broad peak was observed at 8.8 eV, which is attributed to hybridized bonding feature between O 2p bonding and Ag 5s orbitals.[17,23] Indeed Ag 4d is a fully-filled *d* band and no formal hybridization with Ag 4d is expected. Both observations are attributed to the formation of metal oxide pair and associated charge transfer from silver metal to oxygen to form oxide anion. O 1s spectrum supports the formation of oxide (O_2^- appearing around 530 eV) and without any superoxide/ peroxo species (Figure 3.11). The difference spectrum calculated between Figure 3.1b and 3.1a after normalization is Figure 3.2 expected to show the contribution due to metal oxide pair formation and information about, particularly, sigma orbitals of the metal-oxide pair. One of the star marked features could be the energy position of sigma orbital. Large electron donation from Ag surface to oxygen and a significant redistribution of electrons is evident from the difference spectrum. Gas phase features of oxygen on Ag surface appears between 7 and 8 eV, which is different from pure gas phase oxygen peaks that appear between 7.5 and 8.5 eV (Figure 3.1c). The vibrational features of the pure gas phase oxygen and oxygen in the presence of Ag, shows the same width which indicates a homogeneous nature of the surface silver atoms on the sample. A shift by 0.3 eV to low BE is due to the surface potential of Ag (Figure 3.1b). No change in intensity of the E_F characterizes a largely metallic Ag surface (Figure 3.1b).

3.3.2 Temperature Dependent Ag-O_2 Interaction

Figure 3.3a provides a set of temperature dependent VB spectra recorded on Ag surface from 295 to 500 K at 0.1 mbar O_2 pressure. From 295 to 350 K, no change was observed. At 370 K, the gas phase features of oxygen begin to broaden and shift to 7.4 eV. BE of the most intense O_2 vibration feature is always referred to indicate the changes observed unless indicated. Ag

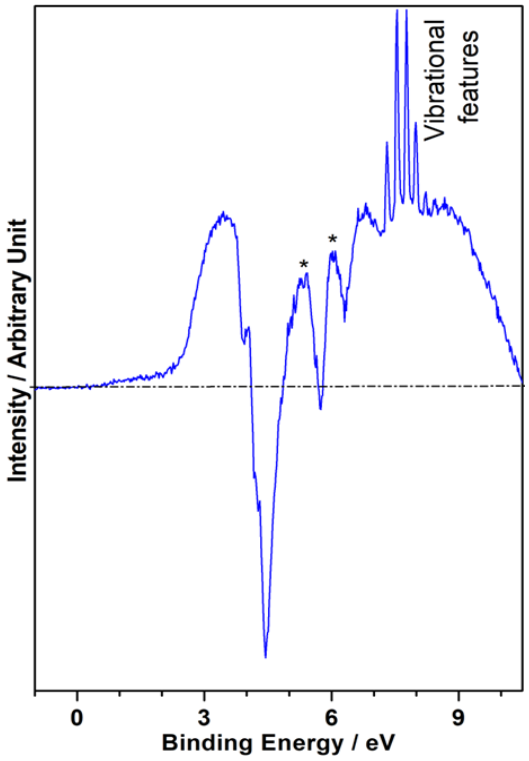

Figure 3.2 : Difference spectrum calculated between clean Ag surface and in the presence of 0.1 mbar O_2 at 295 K spectra (given in Figure 3.1). Sigma orbital energy could be one of the * marked feature.

4d features were unchanged whereas the intensity of O 2p, at 3.35eV, decreased. These observations indicate an onset of change in the electronic nature of silver surfaces under the measurement conditions. The E_F intensity did not change. When the temperature was raised to 390 K, (a) gas phase O_2 vibrational features were observed to be less intense, broadened, and shifted to 7.24eV (Figure 3.3a), and (b) Intensities of bonding and antibonding O 2p features decreased, while features of Ag 4d remain unchanged. Substantial changes were recorded when the temperature was raised to 410 K. (1) ϕ of the Ag surface increased sharply from 4.95 eV (up to 390K) to 5.30 eV (see Figure 3.9). (2) The intensity of the O 2p antibonding and bonding features sharply decreased (Figure 3.3b) which indicated that the surface θ_O is low, even in the presence of large excess of O_2. (3) Ag 4d band peaks at a higher intensity, particularly for the first two components figure 3.4. (4) The gas phase O_2 vibrational features further broadened and shifted towards lower BE to 6.9 eV, indicating the change in nature of

the surface to be heterogeneous in character. The change in ϕ of Ag by 0.35eV and the change in BE of vibrational features of oxygen on Ag (0.34 eV) are found to be in good correlation. The change in ϕ indicates a discreet change in the electronic nature of the Ag surface. (5) E_F intensity remains unchanged. All these observations are fully reversible to metallic Ag, when the O_2 supply was cut-off (*vide infra* Figure 3.10).

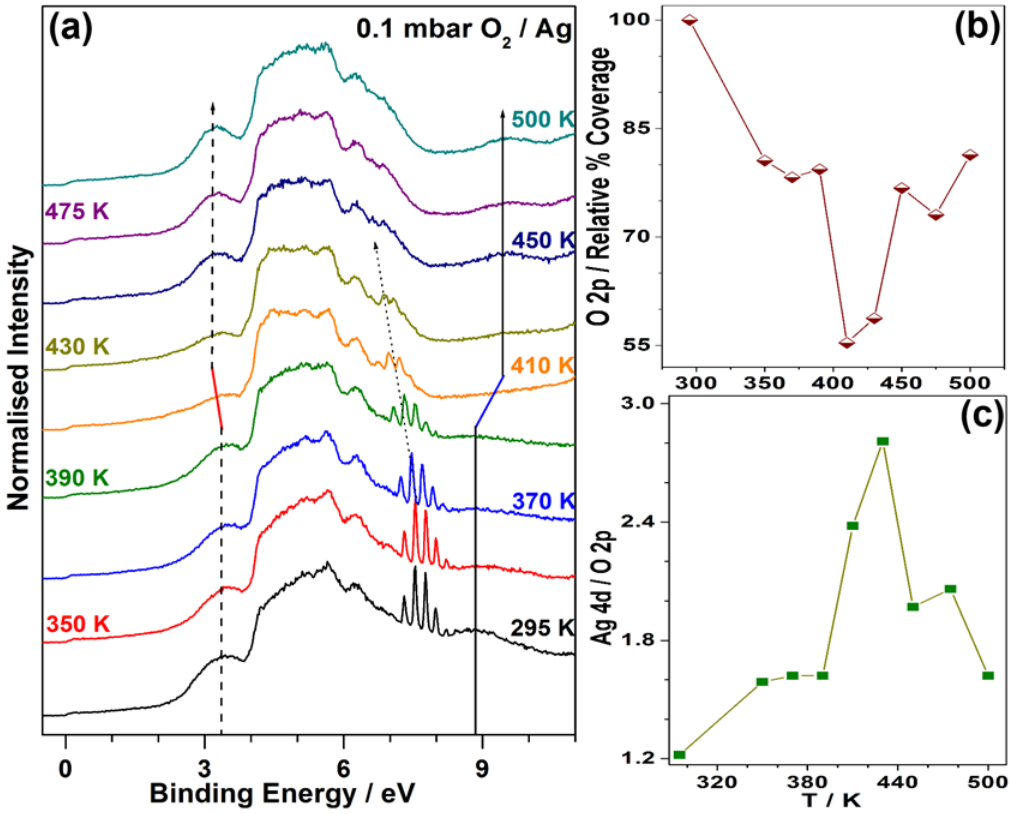

Figure 3.3: (a) Valence band spectra of Ag recorded with He I excitation as a function of temperature at 0.1 mbar O_2. Note a decrease in the intensity of antibonding and bonding O 2p features at 3.15 and 9.5 eV at 410 K with shifts in BE are indicated by dashed and solid arrows, respectively. (b) The contribution from O 2p antibonding band at 0.1 mbar oxygen is plotted against the temperature. (c) Ag 4d/O 2p intensity ratio is plotted as a function of temperature.

It underscores the dynamic changes that occur on the Ag surface in the presence of oxygen. Even if Ag is exposed to plenty of O_2, the intensities of Ag 4d increases and O 2p antibonding decreases; this reflects the unique change that occurred on the surface. Except gold, any other transition metals get oxidized irreversibly under the present measurement conditions; however, the above reversible nature highlights the unique nature of Ag-O_2 -

interactions. We attribute this change with the diffusion of chemisorbed O-atoms into the immediate sub-surfaces of Ag, which modifies the ϕ of Ag. A dynamic equilibrium among the oxygen adsorption, O atoms diffusion into the sub-surfaces of Ag, and oxygen desorption is considered at and above 400 K. No detection of silver oxide (Ag_2O) was observed in the present experimental conditions; this also supports the above conclusion (see Figure 3.10).

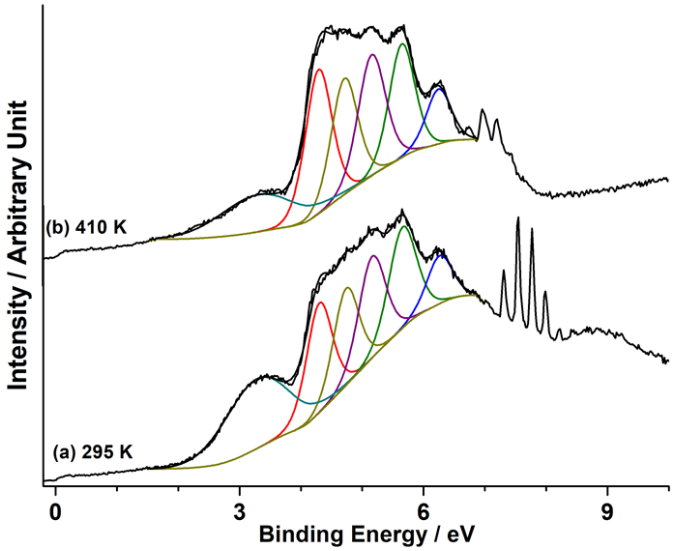

Figure 3.4: Deconvoluted Ag valence band spectra recorded at 295 and 410 K and 0.1 mbar O_2 are shown after normalization. Deconvolution was performed with reference to the binding energy reported from an earlier work (ref. 37: J. Phys.: Cond. Matter **17** (2005) 2671). Note an increase in the intensity of first Ag 4d peak (red color) at 410 K, compared to 295 K. In contrast, the O 2p antibonding band at 3.2 eV decreases in intensity at 410 K, compared to 295 K. Deconvolution was carried out to quantify the changes (reported in Figure. 3.3b and 3.3c) occurring due to the temperature and oxygen pressure.

With further increase in temperature to 430 K at 0.1mbar O_2, the intensity of oxygen antibonding and bonding features increased; however, antibonding feature shifted to lower BE (3.1 eV) and bonding feature shifted to higher BE at 9.5eV. This is due to the reactive nature of antibonding O 2p band at 3.15 eV, and less reactive and stable nature of bonding O 2p band at 9.5 eV. Ag 4d features are similar to that of recorded at 410 K. The O_2 gas phase feature shifted further down to 6.8 eV, and there is no significant change in the ϕ of Ag. The possibility of any interference due to impurities, like carbon or formation of carbonate[30] species, which are likely concerns with a typical high-pressure cell, is absent in the present measurements. No C-species observed in the C 1s spectrum reiterates the clean Ag-surface.

Within the range of 450 to 500 Kat 0.1 mbar, the following changes were recorded. (a) The ϕ of Ag increased from 5.30 (410-440 K) to 5.70 eV (450–500 K). (b) The intensity of the bonding and the antibonding O 2p features further increased, and it is comparable to the intensity observed at 350 K. O 2p antibonding feature is narrow at 450–500 K, compared to that of at ≤430 K. NAP-UPS spectra recorded at 0.2 mbar O_2 pressure Figure 3.5a shows the similar trend. Except a significant decrease in E_F intensity at 500 K, no other important change was observed at 0.2 mbar Figure 3.5a. (c) Increase in the ϕ of Ag and temperature affects further downshift of the oxygen vibrational peaks, and they merged with Ag 4d features. Increase in ϕ at 450K as well as the appearance of O 2p bands at different BE

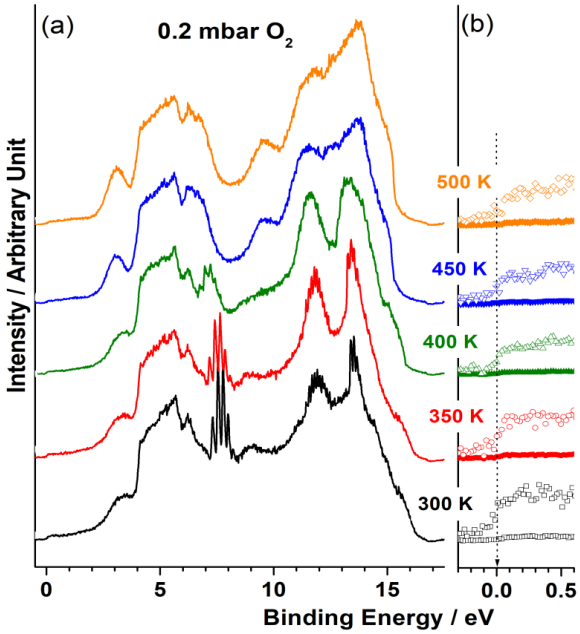

Figure 3.5: Valence band spectra recorded with He-I photons on Ag surface as a function of temperature at 0.2 mbar O_2 partial pressure. Results are shown after normalization. Note the metallic character did not change even in the presence of 0.2 mbar O_2 and up to 500 K. Changes observed at 0.1 and 0.2 mbar O_2 pressure at various temperatures (Figure. 3.3) are very similar.

demonstrates the change in the nature of the surface due to electronic as well as chemical reasons. A similar observation of the change in ϕ of Cu due to the formation of Cu_xO with oxygen was reported earlier.[29] In fact, a mere 0.6 eV shift was observed on the Cu_2O formation with O_2 vibration features, whereas 0.9 eV shift was observed at 450 K just with O-

diffusion into Ag sub-surfaces. It is very likely that the Ag surface undergoes a dynamic partial oxidation. A further increase in temperature up to 650 K does not show any change in the VB. In each set of temperature dependent measurements, three important characteristics were common: (a) Above 400 K, when the oxygen supply was cut-off, all the oxygen-induced changes to disappear, and the surface returns to its original metallic state. It indicates that the presence of oxygen is essential to observe a reversible and dynamic change on the Ag surface. A fast decrease in oxygen-related features observed on increasing the temperature above 500 K after oxygen dosing at 0.1 mbar at 410 K is shown in Figure 3.6. More drastic changes are expected at high pressures under industrial epoxidation conditions. (b) Albeit the intensity changes, Ag 4d band always appear between 4 and 7 eV and shows hardly any shift, irrespective of the applied temperature and oxygen pressure (between UHV to 0.2 mbar O_2

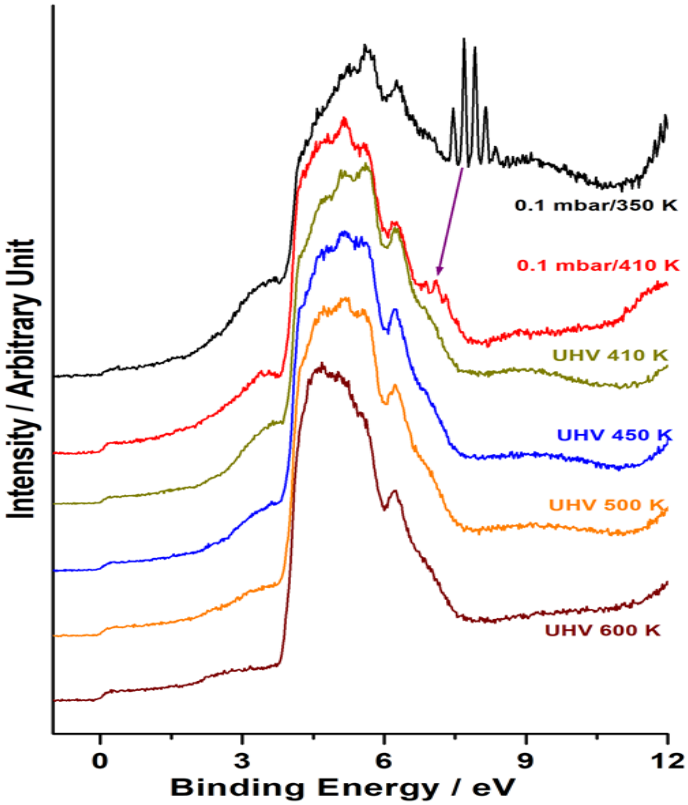

Figure 3.6: NAP-UPS recorded while dosing oxygen at 0.1 mbar and at 350 and 410 K followed by oxygen evacuation. Subsequently UPS was recorded at higher temperatures in UHV shows the disappearance of oxygen related features and room temperature spectrum shows the typical metallic features at UHV. These observations indicate the reversible changes on removing oxygen supply. Normalized spectra are given. It is to be noted that the oxygen (adsorbed and diffused into the subsurfaces) is simply desorbed by a simple thermal treatment.

pressure and up to 600 K). These two observations indicate a subtle and unique interaction of oxygen with Ag under the present reaction conditions. The constant E_F intensity of Ag under the measurement conditions also supports this Figure 3.6. Gold, within group IB elements, possesses similar characteristics and shows hardly any interaction with O_2. However, under such comparable measurement conditions, Cu is prone to form its oxides (Cu_2O and CuO).[29,33] Figure 3.3b shows a relative quantification of O 2p antibonding intensities at different temperatures. The integrated peak area at 295K was considered as 100% oxygen coverage (θ_O) on Ag-surface. With reference to this, other areas were given in relative percentage and are plotted as a function of temperature. The first drop in relative θ_O at 350K does not accompany any change in ϕ. Nonetheless, the second and major change between 390 and 410 K accompanies with a change in θ_O and of Ag. At 450 K, the θ_O again increases to the values similar to that observed at 350 K, but with a change in silver ϕ. The intensity ratio of Ag 4d to antibonding O 2p features was estimated (Figure 3.1.3c) to complement the result shown in Figure 3.3b. First two deconvoluted peaks of Ag 4d Figure 3.4 were considered for this plot. The calculation with the total Ag 4d intensity does not change the trend, shown in Figure 3.3c. Three temperature regimes identified earlier is observed in Figure 3.3c also, reiterating the earlier conclusions. Even though a large amount of gas phase oxygen is available, an unusual decrease in the O 2p feature between 390 and 450K is partly attributed to diffusion of O atoms into the immediate sub-surfaces of Ag. Although oxygen desorption could occur at and above 400 K, this does not support the change in ϕ observed in this temperature window. Further, no impurity such as carbon, carbonate species were observed under the above conditions ≥450 K metastable surface oxide forms and the strong O 2p bonding and antibonding features support this conclusion. This is also evidenced by the decrease in Ag 4d/O 2p ratio (Figure 3.3c). A valley observed between O 2p and Ag 4d features in UVPES deepens further at and above 450K due to increase in the energy difference between them (Figure 3.3a), and ϕ changes from 5.3 (410K) to 5.7 eV (≥450 K). On the basis of these results, it can be concluded that the silver surface has become significantly cationic with the formation of metastable oxide on the surface. Although metastable oxide formation is suggested ≥450 K, it is highly dynamic in nature; the surface shows well resolved Ag 4d features when oxygen was evacuated.

Figure 3.7a is an enlarged view of oxygen vibration features recorded at different temperatures. The vibrational features are characteristic of the Schumann- Runge bands observed in the ultraviolet region around 175–205 nm.[41] As explained above, these narrow vibration features shift towards lower BE, due to the influence of silver surface potential on

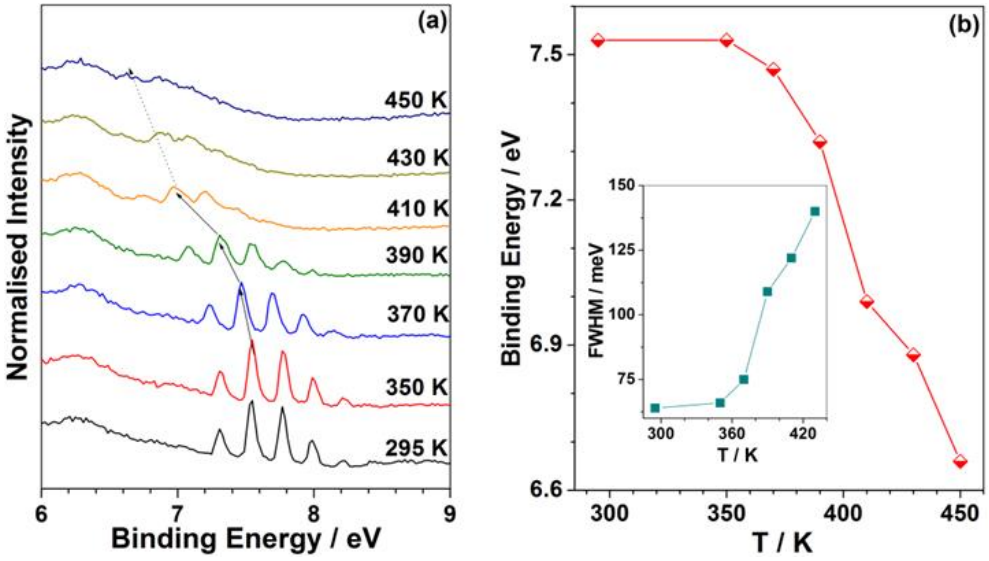

Figure 3.7: (a) Gas phase vibrational features of 0.1 mbar oxygen on Ag is plotted against the temperature. (b) Change in the binding energy of the most intense vibrational peak of O_2 is plotted as a function of temperature. The change in FWHM of O_2 vibration feature with temperature is shown in the inset.

the molecules vibrating close to it. It is to be noted that vibration features are from free O_2 molecules in the gas-phase, but close enough to the surface to sense the electronic changes occurring on the Ag-surface. The broad feature observed at T ≥390K is partly due to surface inhomogeneity, in view of O-diffusion into the sub-surfaces. This is further supported by the gas phase spectrum of in situ heated oxygen shows no significant broadening between 300 and 500 K Figure 3.8. Surface potential influencing Ar 2p core level was recently reported by Axnanda et al.[42] observations, we propose that the sub-surface oxygen population cannot occur in a continuous film; however, it grows into macroscopic size islands with increasing temperature. It is also very interesting to underscore that, in contrast to the expectations of surface potential influencing very limited layers of gas-molecules (of the order of nanometers), surface potential exerts its influence much farther (several hundred microns). This aspect is worth investigating further in a systematic manner. BE of the most intense

Schumann-Runge band is plotted as a function of temperature in Figure 3.7b. A shift toward lower BE was observed above 350 K, compared to RT value. Sharp changes observed at 410 and 450 K are due to the change in the surface potential of Ag, accompanied by a change in ϕ of the Ag surface. The full width at half maximum (FWHM) of oxygen vibrational features is plotted in the inset of Figure 3.7b. Increase in FWHM supports the chemical and electronic

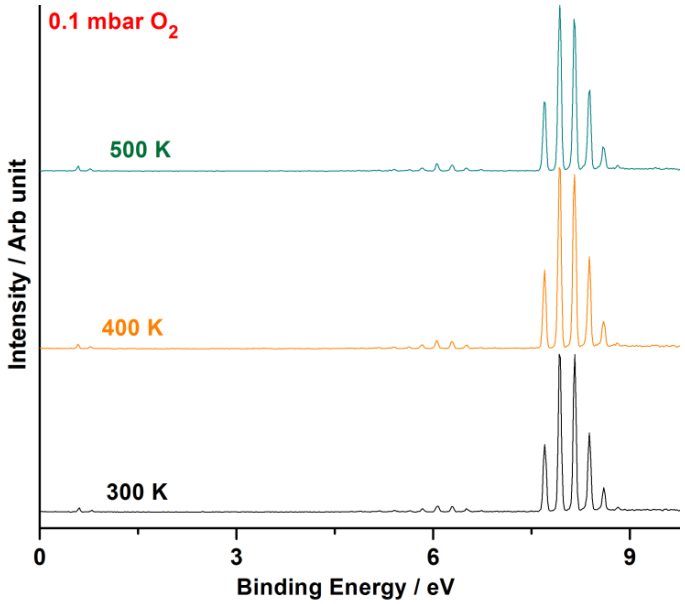

Figure 3.8: Temperature dependent oxygen gas phase spectra were recorded between 300 and 500 K. No significant change in the BE or FWHM of vibrational features was observed. This observation fully supports the shift in BE and FWHM changes observed with oxygen vibrational features in the presence of solid surface is due to the exerting of surface potential.

changes that occur on the surface due to interaction with oxygen. A careful look at the vibration profiles shows that the peak splits into two features at and above 390 K. The heterogeneous nature of the Ag surface imparts such changes. Based on the above due to the heterogeneous distribution of subsurface oxygen, two different surface Ag sites form, one with the presence of subsurface oxygen in its coordination, and the other without any subsurface oxygen. Nonetheless, overall (or average) surface potential also seems to change, which is reflected in the BE shift of oxygen vibrational features. This indicates that epoxidation, as well as combustion of alkenes, are possible simultaneously on such heterogeneous surfaces. However, this needs to be explored by *in situ* microscopy under relevant conditions.

3.3.3 *Temperature Dependent Work Function (ϕ) Changes*

Figure 3.9 shows the secondary cut-off of the Ag VB spectra. The changes in Ag ϕ at different temperatures are evidently notice able. The onset of a change in ϕ begins around 390 K and it increased sharply at 410 K. The second major change in ϕ was observed at 450 K which remains stable up to 650 K. No change in O_2 vibrational features and ϕ of silver observed below 370 K indicate that the nature of the Ag surface is largely unaffected in this regime and it remains largely metallic in nature. Low oxygen desorption temperature at 400 K marks this type of oxygen, which is neither active for epoxidation or combustion.[23] The results discussed above categorize three separate temperature regimes, where each temperature regime has a distinct nature of the interaction between O and Ag. It is also to be mentioned that the ϕ measurements were made at an applied bias of 3V (data not shown). Same ϕ values were obtained with (after correcting values for) applied bias or without bias further supports the actual change in ϕ due to gas-solid O_2-Ag interaction and consequent electronic changes.

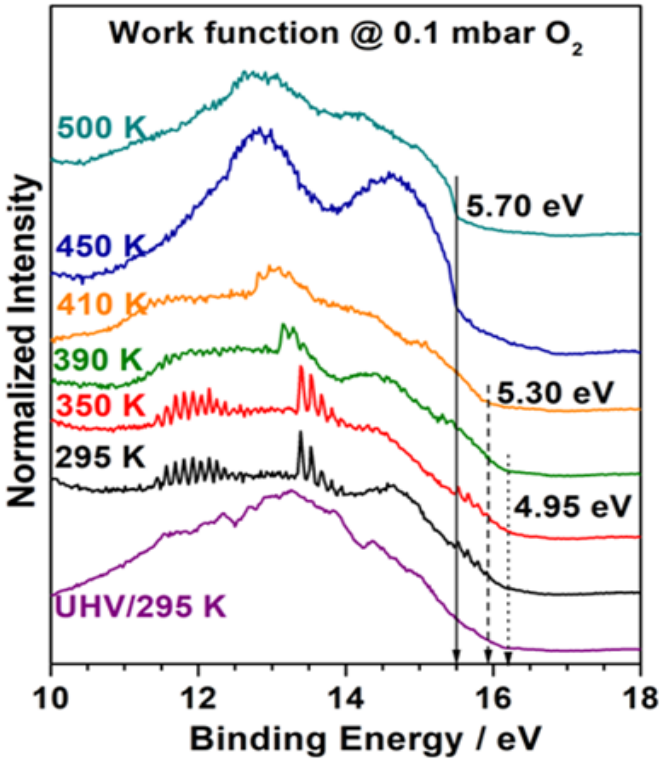

Figure 3.9: Work function measured as a function of temperature at 0.1 mbar oxygen and for clean Ag in UHV at 295 K. The work function of Ag changes from initial 4.95 to 5.3 eV at 410 K and to 5.7 eV at 450 K.

3.3.4 Subtle Silver-Oxygen Interaction

A simple experiment was carried out to understand the nature of antibonding O 2p π-band. Silver surface was exposed to 0.1 mbar O_2 at 350 K and the NAP-UPS was measured. Subsequently, oxygen was evacuated and UPS was measured simultaneously at different temperatures, and the results are shown in Figure 3.10. On gradually increasing the temperature, the intensity of O 2p features decrease while the features of metallic silver reappears ≥350 K. A simple comparison of spectra recorded in UHV and at 0.1 mbar O_2 pressure (Figure 3.3a) fully supports this observation. Critically, no change in ϕ was observed

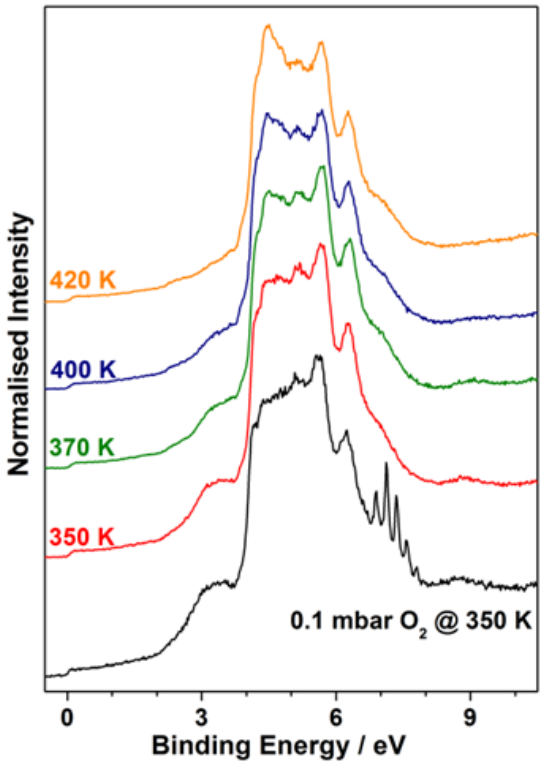

Figure 3.10: UVPES recorded at 0.1 mbar O_2 at 350 K followed by evacuation to UHV and spectral recording at different temperatures. The weakly bound oxygen desorbs and the metallic features of silver revert back gradually.

at 400–420 K, and this underscores that the metallic nature of the silver surface is fully restored. It is also to be reiterated that ϕ changes occur exclusively in the presence of oxygen, and no change observed under UHV conditions further supports the subtle interaction between silver and oxygen. Another point to be highlighted is the large intensity ratio of antibonding to bonding O 2p character (between 5 and 11) across all temperature regions.

This also directly indicates that the oxygen present on the surface is ready to desorb when the oxygen supply was cut-off and makes the Ag-O_2 interaction as the unique one. The diffusion of O atoms into the immediate subsurfaces makes Ag marginally cationic ($Ag^{\delta+}$) in nature; it is to be noted that the diffused oxygen is present as O^{2-}(Figure 3.11) as counter anion to the $Ag^{\delta+}$. This cationic nature creates a space charge layer on the Ag surface and possibly induces a semiconductor-like character.[43] As predicted by van Santen et al.,[17] $Ag^{\delta+}$ character is expected to change the repulsive behavior of alkenes toward Ag to an attractive one ≥ 390 K. In fact, a decrease in the O 2p antibonding character and a shift towards lower BE (Figure 3.3) hints an imminent enhancement in reactivity. A comparison between Figures 3.3b and 3.3c shows an apparent inverse correlation among them. Angle-dependent XPS studies on oxygen interaction with Ag (111) surface too indicates the O-diffusion into subsurface at 420 K.[44]

3.3.5 Core level studies

Figure 3.11 shows O 1s core level spectra recorded at 0.2 mbar O_2 pressure between 295 and 500 K. Very similar to VB, O 1s peak of gas phase molecular oxygen shifts toward low BE (red dash arrow). At 295 K, two peaks for O 1s appear at 538.3 and 539.3 eV, which are typical for O_2. Molecular oxygen has two configurations and photoionization of 1s core level leads to two multiplet states of $^4\sum^-$ and $^2\sum^-$ symmetry with different energies.[45] The peaks broadened, and shifted to 537.9 eV at 400 K, and to 537.6 eV at 450–500 K. It is also to be noted that the doublet observed for O_2 up to 350 K, changed to a featureless single broad peak at ≥400 K. Similar BE shift observed for vibration feature in NAP-UPS and core level of gas-phase O_2 attest the heterogeneity of the surface. While Ag 3d core level does not show any change in the presence of oxygen between 295 and 500K Figure 3.12, O atoms chemisorbed on the surface gives a broad peak around530eV, which can be deconvoluted to three components at 529.4, 530.3 and 531.1 eV. First two components at 529.4 and 530.3 eV are attributed to the nucleophilic and electrophilic O-atoms chemisorbed on the Ag-surface, respectively. This is in accordance to the earlier literature reports.[12,14,44] High BE electrophilic oxygen indicates a relatively low negative charge on it and electron-rich alkenes are attracted towards this. Electrophilic oxygen is expected to be present on cationic $Ag^{\delta+}$ islands, which also makes the reaction with alkene easier. BE of both oxygen species shows the typical oxide (O^{2-}) nature and supports the metal-oxide pair formation. It is also to be noted that there is no

superoxo/peroxo type species are present on the silver surface and no feature observed between 532 and 533eV supports this. The component at 531.1 eV is attributed to O atoms associated with defect sites as well as possible hydroxyl groups, due to interaction with

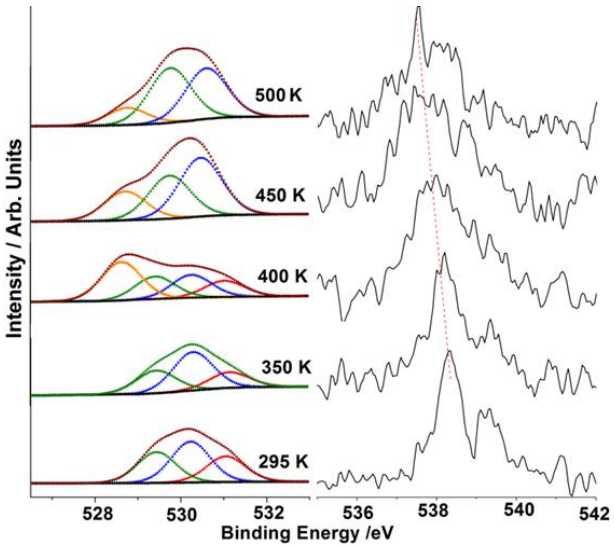

Figure 3.11: O 1s spectra recorded on the silver surface at 0.2 mbar oxygen pressure between 295 and 500 K. Gas-phase oxygen features observed between 536–540eV show a similar BE shift, as observed in NAP-UPS (Figure **3.2**), indicating that the oxygen molecule can be used as probe molecules to observe the change in surface potential.

residual hydrogen in the chamber. When the temperature is raised to 350 K, the relative amount of electrophilic oxygen also increases. With further increase in temperature, the overall intensity at 530 eV decreases, and a new peak appears at 528.7 eV. This new peak is attributed to subsurface oxygen in Ag. The lowest BE of O 1s for subsurface oxygen among the three components indicates the electron donation by adjacent Ag atoms. The lowest BE for subsurface oxygen suggests the oxide nature of subsurface oxygen. In fact, this induces marginally cationic character of the Ag surface. We correlate the diffusion of O into the subsurface with the change in ϕ. In addition, the space charge layer, created on the Ag surface, is likely to hinder the O_2 approaching the surface and this leads to a decrease in surface θ_O. We consider that this is crucial for the onset of attractive interaction with alkenes and subsequently to epoxidation. On further increasing the temperature to 450 K, surface oxygen content increases again while subsurface oxygen was still observed (Figure 3.11).

Electrophilic oxygen at 530.3 eV increases more than other O-species. We attribute that electrophilic oxygen adheres to only those surface atoms beneath which subsurface O atoms are present. Surface defects, which are present in large numbers on polycrystalline Ag, can facilitate the diffusion of subsurface oxygen as in the case of Pd.[46]

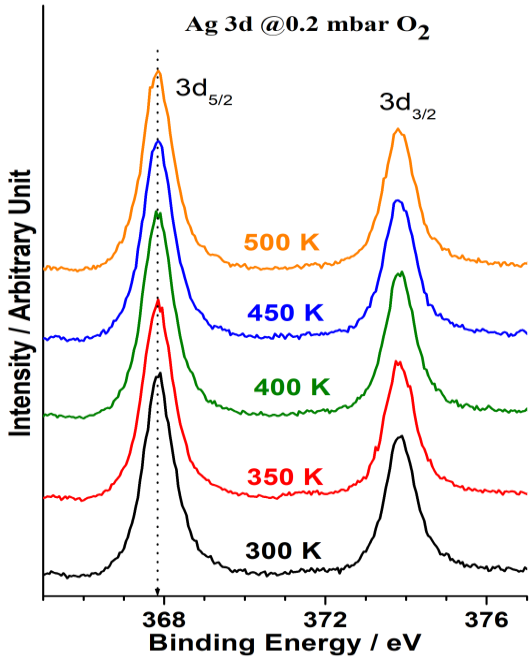

Figure 3.12: Ag 3d core level spectra were recorded at 0.2 mbar O_2 pressure at different temperatures and plotted after normalization. No significant change in the spectra was observed, even though many dynamic changes observed in the VB spectrum under similar conditions (Figures. 3.1-3.4). This is partly attributed to the high probing depth of XPS than UVPES. The metallic character of the silver surface is largely preserved under measurement conditions, as reflected in the Fermi level intensity in Figures 3.1-3.2. These observations underscore the unique and subtle changes that are occurring on the silver surface under the in-situ measurement conditions.

Table 3.1: Table : Binding energy position, FWHM, and percentage ratio of different oxygen species on silver surface at different temperatures from 295 K to 500 K (as in Figure. 3.11).

T / K	Electrophilic Oxygen (~530 eV)		Nucleophilic Oxygen (~529.4 eV)		Subsurface Oxygen (~528.7 eV)		-OH oxygen (~ 531 eV)	
	B.E. (eV)	FWHM (eV) (Area %)	B.E. (eV)	FWHM (eV) (Area %)	B.E. (eV)	FWHM (eV) (Area %)	B.E. (eV)	FWHM (eV) (Area %)
295	530.3	1.07 (~41)	529.4	1.07 (~32)			531.1	1.07 (~27)
350	530.3	1.10 (~50)	529.4	1.10 (~29)			531.1	1.1 (~ 21)
400	530.3	1.10 (~23)	529.5	1.10 (~22)	528.7	1.10 (~38)	531.1	1.1 (~ 17)
450	530.4	1.10 (~45)	579.7	1.12 (~33)	528.7	1.12 (~22)		
500	530.6	1.12 (~42)	529.7	1.12 (~ 44)	582.7	1.10 (~14)		

It is to be noted that nucleophilic oxygen is also present on the surface, and they can simply combust alkene molecules. At 500 K, the intensity of the subsurface O 1s decreases while the nucleophilic and electrophilic oxygen nature changes and shifts to high BE at 529.7 and 530.6 eV, respectively. The intensity of the two components also grows in intensity. This indicates that silver surface is now covered with more oxygen than ≤450 K. This is attributed to the growth of surface oxide, begins above 450 K, and spreads to the immediate sub-surface layers. Consecutive changes in the ϕ of Ag indicate that the surface nature changes, which in turn supports the growth of oxide layers. Diffusion of oxygen into sub-surfaces was further confirmed by angle-dependent O 1s studies and the results are shown in Figure 3.13, and peak fitting parameters are given in Table 1. Development of a new peak at 528.7 eV for O_2 at the normal emission of photoelectrons. However, under the above conditions, angle-dependent XPS shows decreasing subsurface oxygen intensity at lower angles and a simultaneous increase in electrophilic oxygen. This observation fully supports the presence of subsurface oxygen within the probing depth of XPS. Even at the beginning of evacuation of gas-phase oxygen, the surface nature changes considerably at 430 K. With increasing time in UHV or at high temperatures in UHV, the surface reverts to metal. A simple heating to 550K for 2 min removes all the oxygen atoms present on the surface is shown in the top spectrum in Figure 3.13.

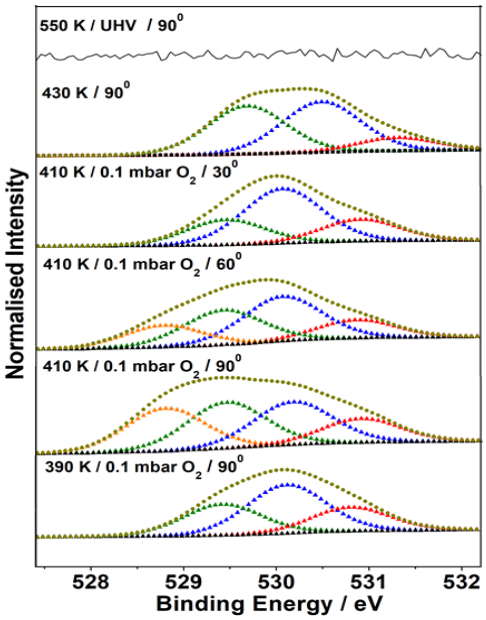

Figure 3.13: Angle-dependent O 1s spectra recorded under relevant conditions. Measurement at 430K was made at the beginning of oxygen evacuation.

Figure 3.14 represents the effects of subsurface oxygen in a schematic way. The population of oxygen in the sub-surfaces of Ag imparts a cationic character to the surface. As an electron-rich molecule, the sticking probability of ethylene to this modified Ag surface is subsurface oxygen is evident at 410 K (orange colour component) in the presence of 0.1mbar likely to be higher than to metallic Ag. The surface silver atoms, which are coordinated to the subsurface oxygen, behave differently from those which do not have subsurface oxygen in their coordination. The former induces electrophilic nature in the oxygen adsorbed onto it. We speculate that the electrophilic oxygen activates ethylene to form EtO. The formation of space charge layers on modified Ag restricts oxygen but favors ethylene adsorption. With the increase in oxygen population in the sub-surface, the surface starts to oxidize gradually and at a certain extent forms the metastable surface oxide. It is to be reminded that commercial Ag-based catalysts work continuously at high pressures, and silver oxide is not active for epoxidation catalysis. A combination of the above facts with our observations suggests a subtle to moderate changes on silver surfaces under actual catalysis conditions.

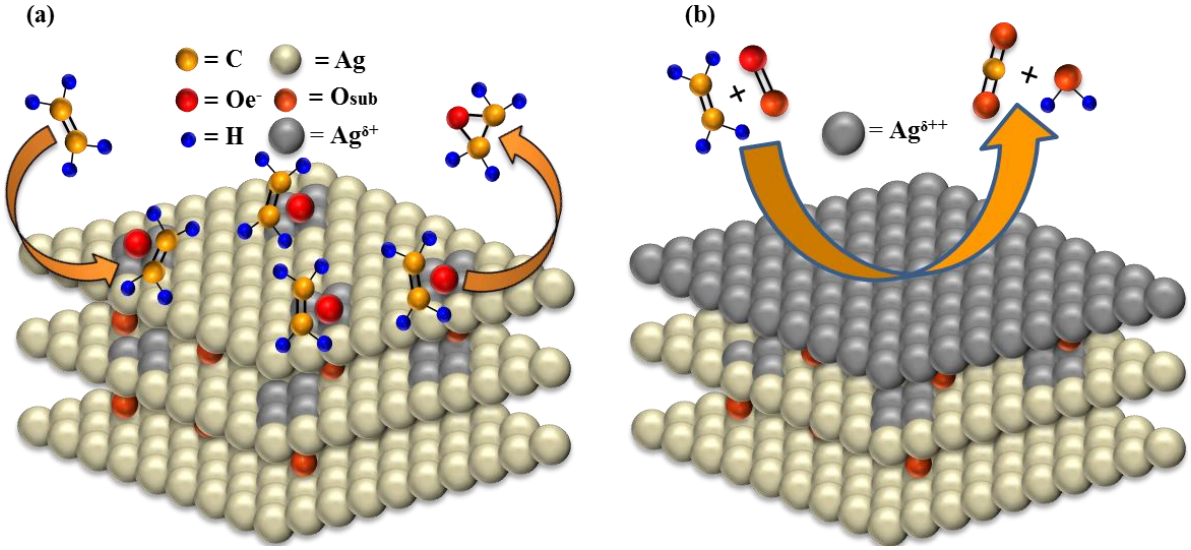

Figure 3.14: Mechanism of (a) ethylene oxidation to EtO, as well as carbon dioxide and water formation. (b) Exclusive combustion occurs on oxidized surface at high temperatures/pressures.

3.4. Conclusions

Ethylene oxide is known to be thermodynamically unstable and it is more prone to combustion than ethylene under typical reaction conditions of epoxidation. We studied the

changes in Ag over the temperature range which is actually employed in ethylene epoxidation. Oxygen diffusion into the subsurface of Ag predominantly occurs between 390 and 450 K, and due to this subsurface population, the Ag surface turns to marginally cationic in nature. The oxygen, further adsorbed on such a cationic Ag-surface, is electrophilic and is highly reactive to ethylene to form epoxide. The increase in ϕ of marginally oxidized silver, in the presence of O_2 at 400 K, compared to its metallic counterpart, fully supports the change in electronic nature of the Ag surface. In a very similar manner, the ϕ increases again at and above 450 K, which reflects the increase in the extent of oxidation. Dynamic and metastable oxide formation on silver surfaces above 450 K favours the complete combustion of alkene to CO_2. A plausible reaction mechanism can thus be proposed from the present findings.

Valence band measurements reveal important changes in the Ag surfaces while Ag 3d core level shows minimal or no change. However, O 1s core level spectra reflect many changes observed in the VB regime. It suggests that changes specifically related to the surface are notably important to understand the reactivity of Ag and oxygen. The behavior of supported Ag catalysts, employed in industrial epoxidation processes, strongly depends on the size of Schottky barriers and band offsets in the heterojunctions between Ag and the semiconducting/insulating support.[47–50] The band offset between metal and the support is expected to be minimized due to the space charge formation on the Ag surfaces by subsurface diffusion of oxygen, and hence ϕ changes on Ag also to be minimized. Indeed, a nearly equal E_F or a minimum difference in E_F is expected between Ag and the support surfaces in the active temperature-window under reaction conditions. Besides that, the formation of space charge on Ag, likely, facilitates epoxidation by facilitating the attraction of alkene molecules toward the catalyst. However, the nature of oxygen on the Ag surface might remain as observed in the present manuscript. The second change in ϕ, observed above 450 K, helps the formation of surface oxides which causes complete combustion of ethylene. It is also to be noted that industrial epoxidation catalysts employ silver supported on alumina with promoters and few other ingredients at high pressures (10–30 bar). Hence, we suggest for detailed ϕ measurements on model surfaces as well as on industrial catalysts

with Kelvin probe force microscopy under reaction conditions. This is expected to give more information about the formation of the space charge layer and the role of surface charge in the reaction.

3.5. References

1. Van Santen, R. A.; Kuipers, H., The mechanism of ethylene epoxidation. *Adv. Catal* **1987,** 35, 265-321.
2. Nagy, A.; Mestl, G., High temperature partial oxidation reactions over silver catalysts. *Appl. Catal. A-Gen.* **1999,** 188, (1), 337-353.
3. Özbek, M. O.; van Santen, R. A. The mechanism of ethylene epoxidation catalysis. *Catal. Lett.* **2013**, *143*, 131-141.
4. L. T. Emile, Process for the production of ethylene oxide US1998878 A23 Apr, 1935.
5. C. N. Satterfield, *Heterogeneous Catalysis in Industrial Practice, 2nd Ed.*; Krieger Publishing Company Malabar, **1996**.
6. Böcklein, S.; Günther, S.; Wintterlin, J., High Pressure Scanning Tunneling Microscopy of a Silver Surface during Catalytic Formation of Ethylene Oxide. Angew Chem. Int. Ed. 2013, 52, (21), 5518-5521.
7. Jones, T. E.; Rocha, T. C. R.; Knop-Gericke, A.; Stampfl, C.; Schlögl, R.; Piccinin, S., Thermodynamic and spectroscopic properties of oxygen on silver under an oxygen atmosphere. *Phys. Chem. Chem. Phys.* **2015,** 17, 9288-9312.
8. Stegelmann, C.; Schiødt, N. C.; Campbell, C. T.; Stoltze, P., Microkinetic modeling of ethylene oxidation over silver. *J. catal.* **2004,** 221, (2), 630-649.
9. Ozbek, M. O.; Onal, I.; Van Santen, R. A., Why silver is the unique catalyst for ethylene epoxidation. *J. catal.* **2011,** *284*, (2), 230-235.
10. Michaelides, A.; Bocquet, M. L.; Sautet, P.; Alavi, A.; King, D. A., Structures and thermodynamic phase transitions for oxygen and silver oxide phases on Ag {111}. *Chem. Phys. Lett.* **2003,** 367, (3), 344-350.
11. Heine, C.; Eren, B.; Lechner, B. A. J.; Salmeron, M., A study of the O/Ag (111) system with scanning tunneling microscopy and x-ray photoelectron spectroscopy at ambient pressures. *Surf. Sci.* **2016,** 652, 51-57.

12. Bukhtiyarov, V. I.; Hävecker, M.; Kaichev, V. V.; Knop-Gericke, A.; Mayer, R. W.; Schlögl, R., Atomic oxygen species on silver: Photoelectron spectroscopy and x-ray absorption studies. *Phys. Rev. B* **2003,** 67, 235422.
13. Xu, Y.; Greeley, J.; Mavrikakis, M., Effect of subsurface oxygen on the reactivity of the Ag (111) surface. *J. Am. Chem. Soc.* **2005,** 127, 12823-12827.
14. Bukhtiyarov, V. I.; Nizovskii, A. I.; Bluhm, H.; Hävecker, M.; Kleimenov, E.; Knop-Gericke, A.; Schlögl, R., Combined in situ XPS and PTRMS study of ethylene epoxidation over silver. *J. catal.* **2006,** 238, 260-269.
15. Bertole, C. J.; Mims, C. A., Dynamic isotope tracing: role of subsurface oxygen in ethylene epoxidation on silver. *J. catal.* **1999,** 184, 224-235.
16. Linic, S.; Barteau, M. A., Formation of a stable surface oxametallacycle that produces ethylene oxide. *J. Am. Chem. Soc.* **2002,** 124, 310-317.
17. Van den Hoek, P. J.; Baerends, E. J.; Van Santen, R. A., Ethylene epoxidation on silver (110): the role of subsurface oxygen. *J. Phys. Chem* **1989,** 93, 6469-6475.
18. Grant, R. B.; Lambert, R. M., A single crystal study of the silver-catalysed selective oxidation and total oxidation of ethylene. *J. catal.* **1985,** 92, 364-375.
19. Campbell, C. T., Surface science study of selective ethylene epoxidation catalyzed by the Ag (110) surface: Structural sensitivity. *J. Vac. Sci. Technol. A* **1984,** 2, 1024-1027.
20. Campbell, C. T.; Paffett, M. T., Model studies of ethylene epoxidation catalyzed by the Ag (110) surface. *Surf. Sci.* **1984,** 139, 396-416
21. Schnadt, J.; Knudsen, J.; Hu, X. L.; Michaelides, A.; Vang, R. T.; Reuter, K.; Li, Z.; Lægsgaard, E.; Scheffler, M.; Besenbacher, F., Experimental and theoretical study of oxygen adsorption structures on Ag (111). *Phys. Rev. B* **2009,** 80, 075424.
22. Yeh, J. J.; Lindau, I., Atomic subshell photoionization cross sections and asymmetry parameters: 1< Z<103. *Atom. Data. Nucl. Data.* **1985,** 32, 1-155.
23. Segeth, W.; Wijngaard, J.; Sawatzky, G., The electronic structure of a new c (2× 2) oxygen phase on Ag (110). *Surface science* **1988,** *194*, 615-625.
24. Boronin, A. I.; Koscheev, S. V.; Zhidomirov, G. M., XPS and UPS study of oxygen states on silver. *J. Electron. Spectrosc. Relat. Phenom.* **1998,** 96, 43-51.

25. Jones, T. E.; Rocha, T. C. R.; Knop-Gericke, A.; Stampfl, C.; Schlögl, R.; Piccinin, S., Insights into the electronic structure of the oxygen species active in alkene epoxidation on silver. *ACS Catal.* **2015,** *5*, 5846-5850
26. Jain, R.; Dubey, A.; Ghosalya, M. K.; Gopinath, C. S., Gas solid interaction of H_2 $Ce_{0.95}$ $Zr_{0.05}$ O_2: new insights into surface participation in heterogeneous catalysis. *Catal. Sci. Tech.* **2016,** *6*, 1746-1756.
27. Gopinath, C. S.; Roy, K.; Nagarajan, S., Can We Shift and/or Broaden the Catalysis Regime towards Ambient Temperature? *ChemCatChem.* **2015,** *7*, 588-594.
28. Roy, K.; Jain, R.; Gopinath, C. S., Sustainable and Near Ambient DeNO x Under Lean Burn Conditions: A Revisit to NO Reduction on Virgin and Modified Pd (111) Surfaces. *ACS Catal.* **2014,** 4, 1801-1811.
29. Roy, K.; Gopinath, C. S., UV Photoelectron Spectroscopy at Near Ambient Pressures: Mapping Valence Band Electronic Structure Changes from Cu to CuO. *Anal. Chem.* **2014,** 86, (8), 3683-3687.
30. Jain, R.; Gnanakumar, E. S.; Gopinath, C. S., Mechanistic Aspects of Wet and Dry CO Oxidation on Co_3O_4 Nanorod Surfaces: A NAP-UPS Study. *Acs Omega* **2017,** *2*, 828-834.
31. Jain, R.; Reddy, K. P.; Ghosalya, M. K.; Gopinath, C. S., Water Mediated Deactivation of Co_3O_4 Naonrods Catalyst for CO Oxidation and Resumption of Activity at and Above 373 K: Electronic Structural Aspects by NAPPES. *J. Phys. Chem. C* **2017,** *121*, 20296-20305.
32. Reddy, K. P.; Jain, R.; Ghosalya, M. K.; Gopinath, C. S., Metallic Cobalt to Spinel Co_3O_4 Electronic Structure Evolution by Near-Ambient Pressure Photoelectron Spectroscopy. *J. Phys. Chem. C* **2017,** *121*, 21472-21481.
33. Roy, K.; Vinod, C. P.; Gopinath, C. S., Design and performance aspects of a custom-built ambient pressure photoelectron spectrometer toward bridging the pressure gap: Oxidation of Cu, Ag, and Au surfaces at 1 mbar O2 pressure. *J. Phys. Chem. C* **2013,** 117, 4717-4726.
34. Dubey, A.; Reddy, K. P.; Gopinath, C. S., Ambient CO Oxidation on In-Situ Generated Co_3O_4 Spinel Surfaces with Random Morphology. *ChemistrySelect* **2017,** *2*, 533-536.
35. Barrie, A.; Christensen, N. E., High-resolution x-ray photoemission spectra of silver. *Phys. Rev. B* **1976,** 14, 2442.

36. Fuster, G.; Tyler, J. M.; Brener, N. E.; Callaway, J.; Bagayoko, D., Electronic structure and related properties of silver. *Phys. Rev. B* **1990,** 42, 7322.
37. Panaccione, G.; Cautero, G.; Cautero, M.; Fondacaro, A.; Grioni, M.; Lacovig, P.; Monaco, G.; Offi, F.; Paolicelli, G.; Sacchi, M., High-energy photoemission in silver: resolving d and sp contributions in valence band spectra. J. Phys. Condens. Matter. **2005**, 17, 2671
38. Yoshino, K.; Freeman, D. E.; Parkinson, W. H., Atlas of the Schumann–Runge absorption bands of O2 in the wavelength region 175–205 nm. *J. Phys. Chem. Ref. Data* **1984,** 13, 207-227.
39. Ertl, G., Dynamics of reactions at surfaces. In *Advances in catalysis*, Elsevier: **2000**; Vol. 45, pp 1-69.
40. Gopinath, C.; Subramanian, S.; Huth, M.; Adrian, H., Comparative photoemission studies of Bi2− xPbxSr2Can− 1CunO2n+ 4+ y (n= 2, 3). *J. Electron. Spectros. Rela.t Phenomena.* **1994,** *70*, 61-71.
41. Yoshino, K.; Freeman, D. E.; Parkinson, W. H., Atlas of the Schumann–Runge absorption bands of O2 in the wavelength region 175–205 nm. *J. Phys. Chem. Ref. Data* **1984,** 13, 207-227.
42. Axnanda, S.; Scheele, M.; Crumlin, E.; Mao, B.; Chang, R.; Rani, S.; Faiz, M.; Wang, S.; Alivisatos, A. P.; Liu, Z., Direct work function measurement by gas phase photoelectron spectroscopy and its application on PbS nanoparticles. *Nano letters* **2013,** *13*, 6176-6182.
43. Kolekar, S. K.; Dubey, A.; Date, K. S.; Datar, S.; Gopinath, C. S., An attempt to correlate surface physics with chemical properties: molecular beam and Kelvin probe investigations of Ce_{1-x} Zr_x O_2 thin films. *Physical Chemistry Chemical Physics* **2016,** *18*, 27594-27602.
44. Bukhtiyarov, V. I.; Kaichev, V. V.; Prosvirin, I. P., Oxygen adsorption on Ag (111): X-ray photoelectron spectroscopy (XPS), angular dependent x-ray photoelectron spectroscopy (ADXPS) and temperature-programmed desorption (TPD) studies. *J. Chem. Phys.* **1999,** 111, 2169-2175.

45. Larsson, M.; Baltzer, P.; Svensson, S.; Wannberg, B.; Martensson, N.; de Brito, A. N.; Correia, N.; Keane, M.; Carlsson-Gothe, M.; Karlsson, L., X-ray photoelectron, Auger electron and ion fragment spectra of O_2 and potential curves of O22+. *Journal of Physics B: Atomic, Molecular and Optical Physics* **1990,** *23*, 1175.
46. Nagarajan, S.; Thirunavukkarasu, K.; Gopinath, C. S., A revisit to carbon monoxide oxidation on Pd (111) surfaces. *J. Phys. Chem. C* **2009,** 113, 7385-7397.
47. Patra, K. K.; Bhuskute, B. D.; Gopinath, C. S., Possibly scalable solar hydrogen generation with quasi-artificial leaf approach. *Scientific Reports* **2017,** *7*, 6515.
48. Patra, K. K.; Gopinath, C. S., Harnessing Visible-Light and Limited Near-IR Photons through Plasmon Effect of Gold Nanorod with $AgTiO_2$. *The Journal of Physical Chemistry C* **2018,** *122*, 1206-1214.
49. Devaraji, P.; Sathu, N. K.; Gopinath, C. S., Ambient oxidation of benzene to phenol by photocatalysis on $Au/Ti_{0.98}V_{0.02}O_2$: Role of holes. *ACS Catalysis* **2014,** *4*, 2844-2853.
50. Patra, K. K.; Gopinath, C. S., Bimetallic and Plasmonic Ag–Au on TiO2 for Solar Water Splitting: An Active Nanocomposite for Entire Visible-Light-Region Absorption. *ChemCatChem* **2016,** *8*, 3294-3311.

Chapter 3b

FeO_x Supported Catalyst for Oxidative Dehydrogenation of n-Butane to 1, 3- Butadiene: Catalysis and Mechanistic Aspects

3.6 Introduction

1,3-butadiene (1,3-BD) is an important monomer for manufacturing styrene butadiene rubber which is the main component in the car tyres. Butadiene is also being used to produce a variety of polymers/chemicals, such as adiponitrile, acrylonitrile–butadiene–styrene, polybutadiene, vinylcyclohexene, hexamethylene diamine, styrene-butadiene latex, chloroprene, and nitrile rubbers.[51,52] Industrially, 1,3-BD is obtained as a side product from naphtha cracking process.[53] Since the amount of naphtha being cracked around the world is huge, C-4 side streaming were sufficient to meet the world's need of 1,3-BD. However, the advent of shale gas and the uncertainties associated with crude oil price opens up the path to find the alternate ways to produce 1,3-BD. Hence, converting butane to 1,3-BD seems to be an attractive way although it poses a significant challenge.[54]

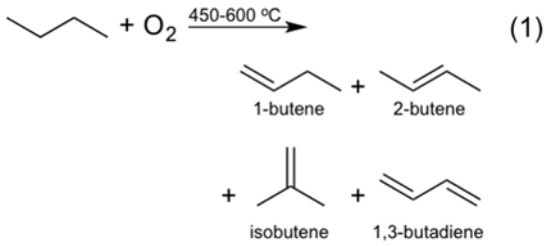

Eq. 3.1 Oxidative dehydrogenation of butane to butenes and butadiene.

In general, commercial productions of small olefins are not common due to thermodynamic limitation, coke formation, high energy uptake and large favorability of cracking. To overcome all the above limitations, oxidative dehydrogenation (ODH) is the best alternate way to produce 1, 3-BD from butane. Addition of oxygen removes H_2 by combustion and also initiates dehydrogenation of the butane and removes the coke by burning off at reaction temperature. Again this process is still far from the commercial application due to combustion of butane and low selectivity of 1,3-BD.[55] Therefore it is important to develop the highly active and selective catalyst for the oxidative dehydrogenation of butane to

1,3-BD reaction. In the literature, many supported catalysts such as VOx/support, Cr_2O_3/SiO_2, Fe-Zn-O, Ni-B/Al_2O_3 and Mg-V based catalysts have been explored for the butane ODH reaction.[55,56] Most of the catalysts suffer either activity and/or selectivity problem. In general, butane ODH reaction results in cracking and combustion products (CO and CO_2) along with dehydrogenation products (1-butenes and 2-butenes) and less selectivity towards 1,3-BD.

In our current work, we have synthesized 5 wt % Fe_2O_3/support (support=Al_2O_3, and Nb_2O_5) catalysts by simple wet impregnation method. The synthesized catalysts were subjected to different physico-chemical characterization techniques to understand the structure and morphology of the catalysts. These catalysts were screened for butane ODH reaction in a fixed bed reactor between 723 and 873 K with varying butane: oxygen ratios (1:1, 1:0.5 and 1:0.25). Among all these catalyst Fe_2O_3/Al_2O_3 catalyst shows best activity in terms of 1, 3-BD yield (higher selectivity towards 1,3-BD) at all different temperatures. In order to understand the active site of the Fe_2O_3/Al_2O_3 catalyst compared with less active catalyst i.e., Fe_2O_3/Nb_2O_5 catalysts we have performed in-situ XPS analysis under simulated reaction conditions. XPS study shows that the iron is present in Fe_2O_3 form on the both fresh catalyst. ODH reactions were carried out at Amsterdam University, Netherlands and NAPPES studies were measured at CSIR- National Chemical Laboratory, Pune India.

3.7: Experimental Section

3.7.1 Synthesis of the Supported Catalysts

Fe supported catalysts were prepared by wet impregnation method. Initially, 50ml of DI water was taken into 250ml RB flask. Then the required amount of $Fe(NO_3)_3.9H_2O$ was dissolved into the water. The calculated amount of alumina, as support, was added to the iron nitrate solution. The mixture was kept for stirring on the magnetic stirrer at 80°C for overnight. Then the powder was calcined at 500°C for 4 h at a ramping rate of 4 °C/min. In this synthesis method, different amounts of Fe (1, 5, 10, 20 wt%) supported catalysts were prepared to find out the best active catalyst. Similarly, Fe supported niobia (Fe/Nb_2O_5) catalyst was also prepared using the same procedure.

3.7.2 Procedure for Catalytic Tests

Oxidative dehydrogenation of butane was carried out in the custom built six-flow parallel fixed-bed setup.[57] This set up enables the fast, yet accurate, screening of catalysts and systematic studies of the reaction conditions. The catalytic reactor system is directly connected to a gas chromatograph (Interscience micro GC, with FID and TCD). The gas feed flow rate and the composition of each catalyst bed can be selected independently, whereas the gas feed composition and the temperature are the same for all six reactors. A back-pressure regulator maintains the feed pressure to the six distributing mass-flow controllers of the individual reactors. A selection valve sequentially selects the product mixture of each reactor and sends it for analysis to the gas chromatograph. Each reactor was loaded with 100 mg catalyst. The reaction temperature was varied from 450 °C to 650 °C. The total reaction feed of each reactor was 32 ml/min, with a volumetric ratio of $O_{2:}$ n-butane: argon varying from 0.25:1:18 to 1:1:18.

3.8 Reaction Results

Butane ODH reaction was carried out using oxygen as an oxidant. The reaction temperature was varied from 723 to 923 K, and at each temperature, the reaction was kept for 30 min to attain the steady state of the reaction. Butane to oxygen ratio was varied from 1:0.25 and 1:0.5 Initially Fe_2O_3/Al_2O_3 with different amount of iron oxide (1, 5, 10 and 20 wt%) loaded catalyst was screened for the butane ODH reaction at different temperatures as well as different butane: oxygen ratios.

Figure 3.15 shows the butane ODH results of Fe_2O_3/Al_2O_3 with different iron oxide (1, 5, 10 and 20 wt. %) loaded catalyst using 1:0.25 butane to oxygen ratio. It is important to note that, in this discussion to avoid the complexity the products are clubbed into three groups, namely selectivity for 1, 3-BD, all C4-products except 1, 3-BD (C4-total) and propylene. The rest of the products are ethylene, methane, CO, and CO_2; however, they are not shown directly in the result. The conclusions derived from these results are as follows (a) 1 wt % Fe_2O_3/Al_2O_3 catalyst shows butane conversion of 3.9 % with a 1,3-BD selectivity of 15.8% at 723 K. As the reaction temperature increases conversion of the butane also increases

and reaches the maximum conversion of 9.7%. However, the highest selectivity i.e., 23.7 % for 1,3-BD was achieved at 773 K at a conversion level of 7.6%. (b) Butane conversion increased to 6 % at 723 K with 1,3-BD selectivity of 33.5% for 5 wt % Fe_2O_3/Al_2O_3 catalyst. Expectedly, butane conversion increases as the reaction temperature increases. At 773 K, the maximum 1,3-BD selectivity of 33.7 % is achieved for 1,3-BD with 6.1 % butane conversion. (c) 10 wt. % Fe_2O_3 /Al_2O_3 catalyst gives 5.2% conversion of butane with maximum 1,3-BD selectivity (28.8 %) at 723 K among all the reaction temperatures. This catalyst also results in the higher conversion of butane with an increase in temperature. At 923 K, maximum of butane conversion of 9.2 % is achieved with 22 % of 1, 3-BD selectivity. (d) 20 wt % Fe_2O_3/Al_2O_3 catalyst results in 4.5% conversion of butane with 16.9 % selectivity of 1,3-BD at 723 K. Similar to other catalysts, conversion of butane is directly proportional to the reaction temperature and maximum butane conversion of 8.5 % is observed at 923 K with 1,3-BD selectivity of 23.3 % . Highest 1, 3-BD selectivity of 26.1 % is obtained at 873 K with 6.7% butane conversion.

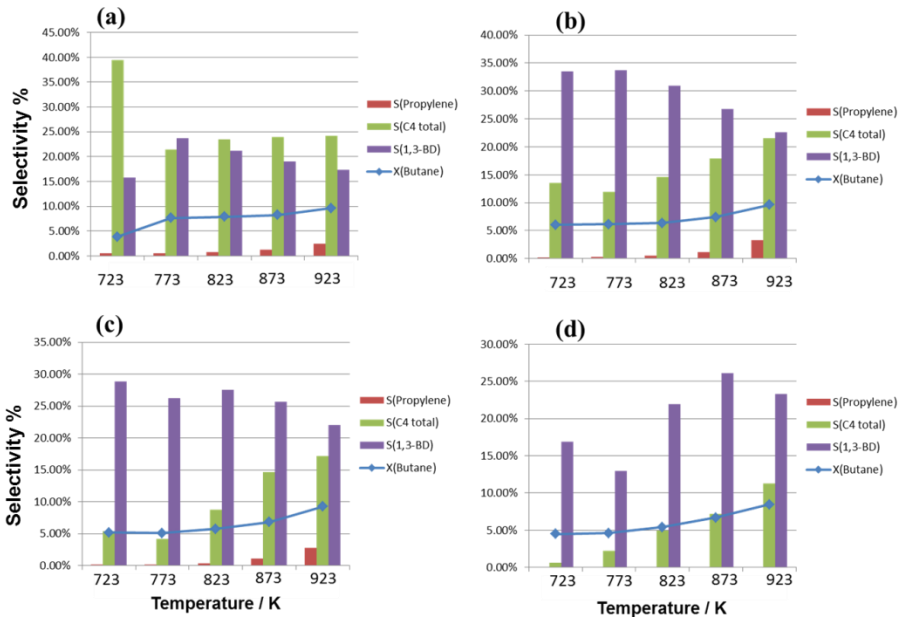

Figure 3.15: The catalytic performance of (a) 1 wt % of Fe_2O_3/Al_2O_3 (b) 5 wt % of Fe_2O_3/Al_2O_3 (c) 10 wt % of Fe_2O_3/Al_2O_3 and (d) 20 wt % of Fe_2O_3/Al_2O_3 catalyst. 5% of Fe_2O_3/Al_2O_3 shows the high selectivity for 1,3-BD observed at lower temperatures (723 and 773 K). Butane to oxygen ratio was maintained at (1 : 0.25).

The next batch of butane ODH reaction is carried out with 1:0.5 ratio of butane to oxygen ratio for different Fe_2O_3/Al_2O_3 supported (1, 5, 10 and 20 wt%) catalyst and the results are shown in Figure 3.16. 1,3-BD conversion doubles for all the catalyst compositions and in the measured temperature range, compared to the results obtained with feed composition of 1:0.25 (Figure. 3.15). The important conclusions derived from this reaction are as follows: (a) 1 wt % Fe_2O_3/Al_2O_3 catalyst shows 5 % butane conversion with 14.1 % selectivity towards 1,3-BD at 723 K. Conversion of the butane increases as the temperature of the reaction increases and reached a maximum of 16.1 % at 923 K. Maximum selectivity of 17.2% for 1,3-BD is obtained at 773 K with 13% butane conversion (b) At 723 K, 5 wt % Fe_2O_3/Al_2O_3 catalyst gives 9.9 % butane conversion with 1,3-BD selectivity of 27%. Maximum selectivity for 1,3-BD, i.e., 28.2 % is achieved at 773 K with 10.3% butane conversion (c) 10 wt % Fe2O3/Al_2O_3 catalyst shows 8.7% butane conversion with 20.3 % selectivity towards 1,3-BD at 723 K. Maximum 1,3-BD selectivity of 22.8 % is obtained at 823 K with 9.5 % butane conversion. Conversion of butane is increasing as the reaction temperature increases and reached the maximum conversion of 13.5 % with 20.1 % selectivity of 1, 3-BD. (d) 20 wt % Fe2O3/Al_2O_3 catalyst results in butane conversion of 7.4 % at 723 K with 1,3-BD selectivity of 10.7 %. Similar to the other catalysts, conversion of butane is directly proportional to the reaction temperature. Highest selectivity for 1, 3-BD i.e., 21.8% is obtained at 873 K with 10.9% butane conversion. It is to be noted that at high temperatures, large amount of cracking also occurs and that leads to other products, such as CO, CO_2, ethylene, methane. Hence a relatively low temperature is preferred to minimize cracking as well as to maximize 1, 3-BD selectivity.

The same reaction is also carried out with 1:1 ratio of butane to oxygen; although the butane conversion increases between 15-20 %, selectivity to 1.3-BD is the lowest than the butane to oxygen ratio 1: 0.5 for different amount of Fe_2O_3/Al_2O_3 supported (1, 5, 10 and 20 wt%) catalyst. In addition to that, large amount of cracking and combustion occurs, which leads to CO, CO2, methane etc. In view of this the results obtained with 1:1 ratio of butane:oxygen is not shown .

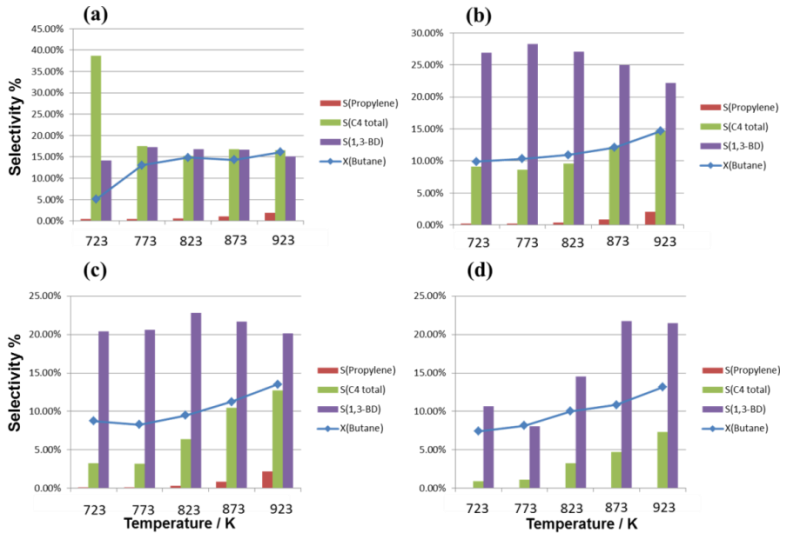

Figure 3.16: The catalytic performance of (a) 1% of Fe_2O_3/Al_2O_3 (b) 5% of Fe_2O_3/Al_2O_3 (c) 10% of Fe_2O_3/Al_2O_3 and (d) 20% of Fe_2O_3/Al_2O_3 catalyst. 5% of Fe2O3/Al_2O_3 shows the high selectivity for 1,3-butadiene observed at 773 K. Butane oxygen ratio was maintained at 1 : 0.5.

The conclusions derived from above reaction are as follows: (1) Generally, when the reaction temperature increases the conversion of the butane also increases due to the contribution from thermal effect for different butane to oxygen ratio. (2) Selectivity for 1, 3-BD is increasing from 723 K to a higher reaction temperature. However, once it reaches the maximum, it started to decrease at higher temperatures (3) Butane to oxygen ratio plays an important role in determining the conversion of butane and selectivity of 1,3-BD. When 1:0.25 butane to oxygen ratio is used, lower conversion of butane and best selectivity of 1, 3-BD is obtained at certain temperature compared with 1:0.5 and 1:1 butane to oxygen ratio at the same temperature. (4) Among all screened Fe_2O_3/Al_2O_3 catalyst compositions, 5 wt % Fe_2O_3/Al_2O_3 catalyst gives better butane conversion and high selectivity towards 1, 3-BD compared to another Fe_2O_3/Al_2O_3 supported catalyst; this composition also provides smaller amount of cracking products. Hence 5 wt % Fe_2O_3/Al_2O_3 catalyst is considered as an optimum performance catalyst.

In order to see how other supported catalyst performs for the same butane ODH reaction, 5 wt% Fe_2O_3/Nb_2O_5 catalyst was synthesized and tested using different butane to

oxygen ratio between 723 K to 923 K. Reaction results obtained for 5 wt % Fe_2O_3/Nb_2O_5 catalyst is shown in Figure 3.17. The highest butane conversion is obtained with 1:0.5 ratio of butane to oxygen at 923 K. However, the highest 1,3- BD selectivity (10 %) is observed with 1:0.25 ratio of butane to oxygen at 923 K. 5 wt % Fe_2O_3/Nb_2O_5 catalyst always gave significantly low butane conversion and selectivity towards 1,3-BD irrespective of the butane to oxygen ratio. It is important to note that, even the butenes selectivity altogether were extremely lower than the 5 wt % Fe_2O_3/Al_2O_3 catalyst.

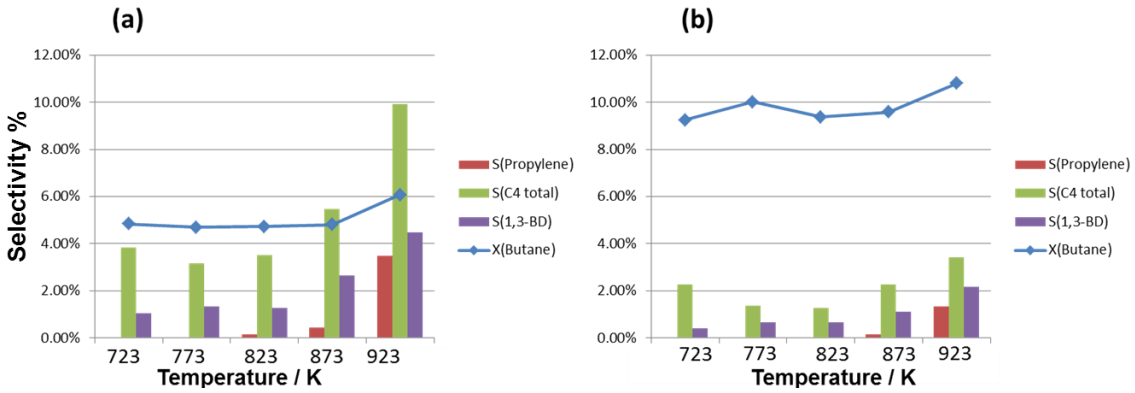

Figure 3.17 : The catalytic performance observed for 5 wt % Fe_2O_3/Nb_2O_5 with (a) butane to oxygen ratio (1 : 0.25) and (b) 1 : 0.5. The highest 1,3- BD is observed with 1:0.25 ratio of butane to oxygen at 923 K and highest conversion is obtained with 1:0.5 ratio of butane to oxygen at 923 K. However, the conversion and selectivity is far lower compared to the catalyst supported on alumina.

From the comparison of 5 wt % Fe_2O_3/Nb_2O_5 and 5 wt % $FeOx/Al_2O_3$ catalyst we can derive the following conclusions: (1) 5 wt % Fe_2O_3/Al_2O_3 catalyst is selective towards 1,3-BD with relatively high conversion irrespective of all temperatures and butane to oxygen ratios. (2) Fe_2O_3/Nb_2O_5 catalyst shows poor conversion compared to Fe_2O_3/Al_2O_3 catalyst; however 1,3-BD selectivity is very poor. It is important to note that even other butenes selectivity is not good. Very high percent of butanes undergoes combustion reaction leading to CO, CO_2. (3) Even though both the catalyst have the same amount of Fe_2O_3 species, different reactivity/selectivity for butane ODH products were obtained for similar reaction conditions. Although the difference in activity could be attributed to catalyst-support interaction, is there any other changes occur, which is not obvious from the reaction results are worth exploring.

Here, we have synthesized the Fe_2O_3 catalyst on two supports and tested the catalyst for butane ODH reaction with varying the temperature and butane-oxygen ratio. The best yield and selectivity was obtained with the 5 wt % Fe_2O_3/Al_2O_3 catalyst with 1: 0.5, butane oxygen ratio. Whereas, Fe_2O_3/Nb_2O_5 catalyst showed very low butane conversion and very low selectivity to 1, 3-BD also. In both catalysts, Al_2O_3 and Nb_2O_5 are not active for butane ODH reaction, and Fe_2O_3 is the common and active catalyst for this reaction. Our efforts to measure the activity with support alone leads exclusively to combustion products with very low conversion indicating the role of catalytic activity of support is minimal. However, interestingly Fe_2O_3/Nb_2O_5 does not show any activity and 5% Fe_2O_3/Al_2O_3 shows very good conversion of butane with ~30% 1, 3- BD selectivity. All these results, clearly indicating that there are possible electronic interactions which are the critical for the ODH reaction of butane as well as high selectivity to 1, 3 BD. To understand these results we have carried out the NAPXPS study under the simulated reaction condition.

3.9 NAPPES Study

The NAPXPS spectra recorded on Fe_2O_3/Al_2O_3 at 0.1 mbar pressure of Butane: Oxygen: Argon (2: 1: 3) mixture between 573 to 873 K is shown in Figure 3.18. It can be seen that at 573 K a broad Fe 2p core level peaks are observed with significant satellite intensity. Deconvolution procedure adopted to Fe $2p_{3/2}$ core level shows peaks at 710.1, 711.4, 712.6 and 713.9 eV with a strong satellite feature at 719.0 eV, which indicate that Fe is present in the form of (Fe^{+3}) Fe_2O_3. Here Fe_2O_3 gives four features (Fe^{+3} 2p gives four multiples due to crystal field splitting)[58,59]. Similarly due to spin orbit coupling, the Fe $2p_{1/2}$ core level is also observed in between 722.5 to 726 eV which are fitted to four peaks. Although no butane conversion and any products were observed below 700 K, different Fe oxidation states observed testifies the beginning of the interaction. . On increasing the temperature to 723 K, two new peaks arises at 707.6 eV (purple color) and 709 eV (wine blue). These are related to iron carbide[60] and FeO (Fe^{+2})[61], respectively. The presence of satellite at 714.8 eV (dark cyan color) is strongly support the presence of FeO species on the catalyst surface. However; iron carbide does not give any satellite peak. In iron carbide, the partial charge transfer takes place from carbon to iron, as carbon is less electronegative than oxygen. In fact, the nature of iron

in iron carbide is closer to metallic iron due to high charge density. Iron carbide and metallic iron appears between 707-707.5 eV and it fully supports the metallic character of iron carbide under the reaction conditions. Mattevi et al.[62] studied the Fe_2O_3/Al_2O_3 and Fe_2O_3/SiO_2 interactions and growth of carbon nanotubes (CNT) by *in situ* XPS. They observed that, Fe^{+2} and Fe^{+3} both species were present on the Al_2O_3 supported catalyst whereas, on SiO_2 only Fe^{+3} species were present at 1023 K. This study indirectly supports our observations of Fe^{+2} and Fe^{+3} species. Under the reaction and NAPXPS conditions, butane act as a reducer gas for iron due to that Fe_2O_3 was reduced to FeO. Kramm et al. observed by XRD that FeO can be converted to FeC at 773-873 K.[63] However, we observed the carbide formation at 723 K. It is to be noted that butane ODH reaction is an exothermic reaction and local hotspots are very much possible; in fact the average catalyst surface temperature is expected to be more than the applied temperature due to formation of hot spots.

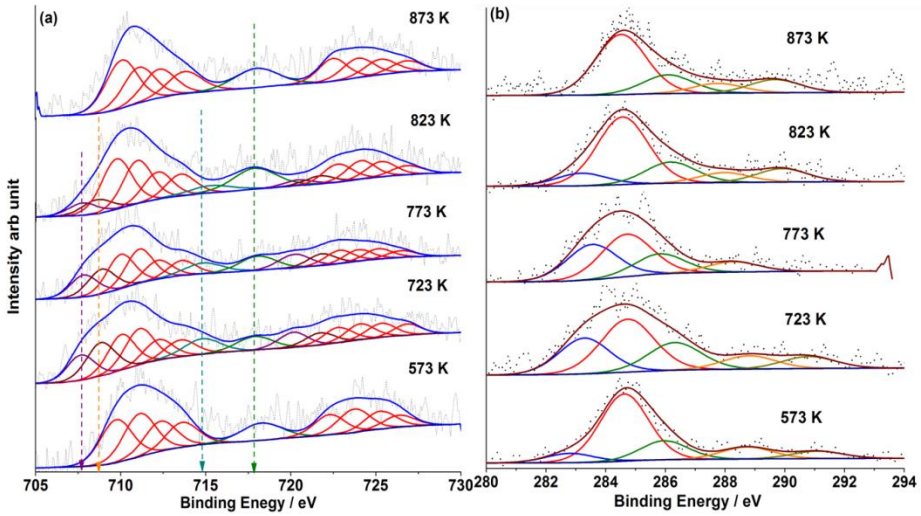

Figure 3.18: (a) Fe $2p_{3/2}$ and Fe $2p_{1/2}$ spectra obtained on 5 wt % Fe_2O_3 on Al_2O_3 catalyst under NAPPES conditions recorded at 0.1 mbar pressure of butane:oxygen:argon (2: 1: 3) from 723 K to 873 K. At 573 K Fe is present in Fe^{+3} (red color peaks are associated with +3 oxidation state). At 723 K two peaks are observed at 707.6 eV (purple color) and 709.1 eV (wine color) due to iron carbide and FeO respectively. Carbon 1s spectra recorded under NAPPES conditions are shown in panel b. At 723 K carbide formation (Purple color) occurs, which is stable up to 823 K and disappears above 823 K.

The iron carbide formation on catalyst surface is also confirmed by the carbon 1s core level spectra shown in Figure 3.18b. At 523 K, five peaks are present at 282.8 eV, 284.6 eV, 286.6 eV, 288.8 eV and 291 eV. The first peak at 282.7 eV is observed due to the carbide formation on catalyst surface. Second component is the major component and it is attributed to the adsorbed butane. Higher BE peaks are attributed to the carbon bonded to either lattice oxygen or adsorbed oxygen. As the temperature increases to 723 K, low BE carbide feature at 282.8 eV gets shifted towards higher BE at 283.2 eV; it is to be noted that at the same temperature (723 K) there are two new low BE features develops in Fe 2p spectra, as explained in Figure 3.18a which is confirmed the formation of iron carbide. The peak centered at 284.6 eV carbon spectra is arises due to the sp^3 C of butane on catalyst surface. Next three peak are centered at 286.6 eV, 288.8 eV and 291 eV arises due to the carbon of C-O, C=O and CO_2 respectively.[4] The presence of carbon peak at 283.2 eV shows the solid evidence on carbide formation at 723 K. Carbide peak of C 1s at 283.2 and Fe $2p_{3/2}$ peak at 707.6 are present up to 800 K. However, at and above 823 K the intensity of both peaks decreased drastically and at 873 K they diminish completely. It is very likely that at 873 K, the iron carbide and FeO is re-oxidized to Fe_2O_3 which can be confirmed by the disappearance of the iron carbide peak at 707.6 eV and FeO main peak and satellite peak at 709 and 714.8, respectively. It is also to be noted that the intensity of satellite peak of Fe_2O_3 also increased. It can be concluded that the iron carbide formation takes place around 723 K which is stable up to ~800 K. As explained in section 3.8 (Figure 3.16b) below 723 K there is no 1,3-BD formation was observed. The identification of carbide features in NAP-XPS and high yield of 1,3-BD correlates very well and both occur simultaneously. This reiterates the importance of carbide formation, possibly as a precursor for 1,3-BD formation. It is also possible that iron carbide could be an active phase and responsible for 1,3-BD and more studies may be required. It is to be noted that, as explained in other chapters, ϕ of the active phase matters a lot for the reaction. Compared to oxide, carbide is expected to exhibit different work function, which might be a reason for the high catalytic activity associated in the presence of carbide.

An interesting result is also observed with Al 2p core level features and the result is

shown in Figure 3.19. Generally, Al 2p feature of Al^{+3} (Al_2O_3) is observed at ~75 eV. In addition to the Al 2p feature observed at 75.2 eV, very low intense peak was also observed at 72.7 eV at 573 K. However, when the temperature is increased to 723 K the peak shift to lower B. E. to 74.7 eV as well the intensity of the peak centered at 72.4 eV increased substantially. The interesting aspect is that Al_2O_3 is very stable and it cannot be reduced at least under the above reaction conditions. There is a possibility of formation of a heterojunction on Al_2O_3 leading to metal-semiconductor (iron carbide-alumina) junction. . Although oxidation state of aluminum to be retained in 3+ state, the heterojunction would make the alumina to appear at lower BE.

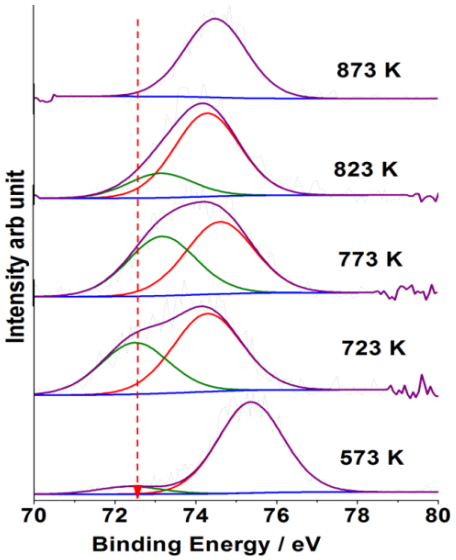

Figure 3.19: Al 2p core level feature recorded under NAPXPS conditions from 573K to 873 K. Two peaks are observed at 75.2 and ~72.7eV.

To further confirmation we have also studied the least active and least selective catalyst Fe_2O_3/Nb_2O_5 catalyst by NAP-XPS under similar condition, employed for Figure 3.17 and 3.18. The XPS spectra of Fe_2O_3/ Nb_2O_5 shown in Figure 3.20 at 0.2 mbar pressure Butane: Oxygen: Argon (2: 1: 3) from 573 to 873 K. Fe remains to be present in Fe_2O_3 form on Nb_2O_5 catalyst. It has been observed that with changing the temperature there is no change in the oxidation state of Fe catalyst on the Nb_2O_5 catalyst. This directly indicates that there is no interaction between Fe catalyst and Nb_2O_5. Further, there is no carbide feature formation

was observed, as in the earlier case. However, there is a small shift is observed towards lower BE in Nb 3d spectra. Nb_2O_5 is stable up to ~1300 K even in reducing environment[64] and hence the possibility of Nb_2O_5 reduction is ruled out. Probably this shift is observed due to the adsorption of reactant and product which leads to the band bending resulting in the changes in BE.[65]

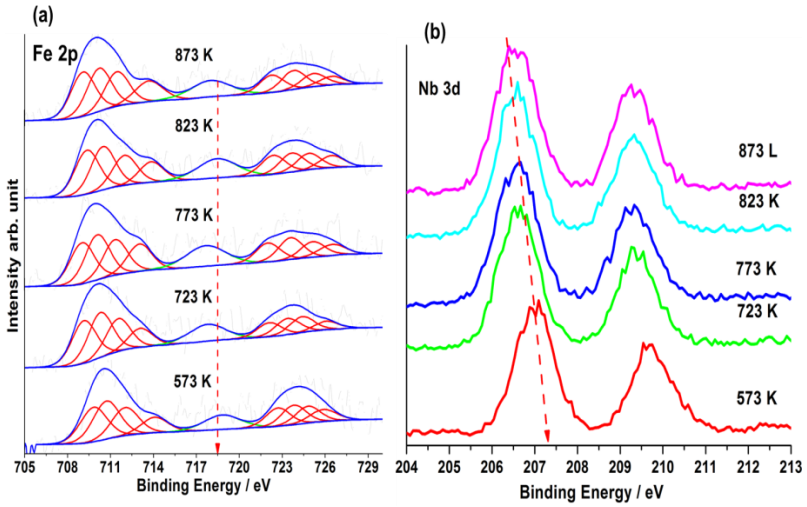

Figure 3.20: (a) Fe $2p_{3/2}$ and Fe $2p_{1/2}$ spectra recorded on 5 wt % Fe_2O_3/Nb_2O_5 catalyst under NAPXPS conditions recorded at 0.2 mbar pressure Butane: Oxygen: Argon (2: 1: 3) from 573 to 873 K. There is no reduction observed for Fe. (b) Nb 3d of Nb_2O_5.

3.10 Conclusion

We have synthesized the Fe_2O_3 catalyst on Al_2O_3 and Nb_2O_5 supports for ODH of butane. ODH of butane has been carried out as a function of temperature, % of Fe_2O_3 on supports and ratio of butane and oxygen mixture. It has been observed that 5% Fe_2O_3/Al_2O_3 catalyst shows high selectivity for 1,3-BD at low temperature (723 K) with 1:0.5 butane oxygen ratio. To understand the active center of catalyst for high selectivity and effect of support on selectivity to 1,-3BD, we carried out the NAPXPS studies. NAPXPS studies were carried out on high selective catalyst 5% Fe_2O_3/Al_2O_3 and least selective catalyst 5%Fe_2O_3/Nb_2O_5. In NAPXPS study it has been observed the reduction of Fe_2O_3 to FeO and formation of iron carbide on Fe_2O_3/Al_2O_3 catalyst under the simulated butane ODH reaction conditions. Whereas, no

reduction of Fe_2O_3, or carbide formation was observed on Fe_2O_3/Nb_2O_5 catalyst under similar reaction conditions. Portela et al.[66] observed that with increasing the coal charge on nickel-molybdenum metal oxide catalyst at 673 K also increased the 1, 3-BD selectivity in butane ODH reaction and after 873 K the selectivity is decreased. However, there are no reasons available about the origin of active center(s) and reason for decrease in the selectivity after 873 K. Present studies clearly indicating the relation between the high selectivity to 1,3-BD and iron carbide formation on catalyst surface. Based on the experimental results and observations it has been concluded that iron carbide is very likely to be the active center for the butane ODH reaction to 1,-3-BD rather than other alkene. When the temperature increased more than 800 K, the iron carbide and FeO re-oxidized to Fe_2O_3 which leads to decrease in the selectivity to 1,3-BD. This study has demonstrated the role of new phase formation under catalysis conditions and metal-catalyst support interactions on the selectivity and activity of catalyst.

3.11 References

51. Bartholomew, C. H.; Farrauto, R. J., *Fundamentals of industrial catalytic processes*. John Wiley & Sons: **2011**.
52. Chenier, P. J., *Survey of industrial chemistry*. Springer Science & Business Media: **2012**.
53. White, W. C., Butadiene production process overview. *Chem.-Biol. Interact.* **2007,** *166*, 10-14.
54. Plotkin, J. S., The continuing quest for butadiene. *ACS*: **2016**.
55. Madeira, L. M.; Portela, M. F., Catalytic oxidative dehydrogenation of n-butane. *Catal. Rev.* **2002,** 44, 247-286.
56. Makshina, E. V.; Dusselier, M.; Janssens, W.; Degreve, J.; Jacobs, P. A.; Sels, B. F., Review of old chemistry and new catalytic advances in the on-purpose synthesis of butadiene. *Chem. Soc. Rev*. **2014**, 43, 7917-7953.
57. Ng, W. H.; Gnanakumar, E. S.; Batyrev, E.; Sharma, S. K.; Pujari, P. K.; Greer, H. F.; Zhou, W.; Sakidja, R.; Rothenberg, G.; Barsoum, M. W., The Ti3AlC2 MAX phase as an efficient catalyst for oxidative dehydrogenation of n-butane. *Angew. Chem.* **2018,** *130*, 1501-1506

58. Grosvenor, A.; Kobe, B.; Biesinger, M.; McIntyre, N., Investigation of multiplet splitting of Fe 2p XPS spectra and bonding in iron compounds. *Surf. Interface Anal*. **2004,** *36*, 1564-1574.
59. Gupta, R.; Sen, S., Calculation of multiplet structure of core p-vacancy levels. *Phys. Rev. B* **1974,** *10*, 71.
60. Furlan, A.; Jansson, U.; Lu, J.; Hultman, L.; Magnuson, M., Structure and bonding in amorphous iron carbide thin films. *J. Phys. Condens. Matter.* **2015,** *27*, 045002.
61. Yamashita, T.; Hayes, P., Analysis of XPS spectra of Fe2+ and Fe3+ ions in oxide materials. *Appl. Surf. Sci.* **2008,** *254* (8), 2441-2449.
62. Mattevi, C.; Wirth, C. T.; Hofmann, S.; Blume, R.; Cantoro, M.; Ducati, C.; Cepek, C.; Knop-Gericke, A.; Milne, S.; Castellarin-Cudia, C., In-situ X-ray photoelectron spectroscopy study of catalyst− support interactions and growth of carbon nanotube forests. *J. Phys. Chem. C* **2008,** *112*, 12207-12213.
63. Kramm, U. I.; Herrmann-Geppert, I.; Fiechter, S.; Zehl, G.; Zizak, I.; Dorbandt, I.; Schmeißer, D.; Bogdanoff, P., Effect of iron-carbide formation on the number of active sites in Fe–N–C catalysts for the oxygen reduction reaction in acidic media. *J. Mater. Chem. A* **2014,** 2, 2663-2670.
64. Forghany, S. K. E.; Anderson, J. S., Reduction and polymorphic transformation of B-Nb_2O_5. *J. Chem. Soc., Dalton Trans*. **1981**, *1*, 255-261.
65. Eichelbaum, M.; Hävecker, M.; Heine, C.; Wernbacher, A. M.; Rosowski, F.; Trunschke, A.; Schlögl, R., The electronic factor in alkane oxidation catalysis. *Angew. Chem.* **2015,** *54* (10), 2922-2926.
66. Maldonado-Hodar, F.; Madeira, L.; Portela, M., The use of coals as catalysts for the oxidative dehydrogenation of n-butane. *Appl. Catal., A* **1999,** *178*, 49-60.

Chapter 4

Silicon Oxidation by NAPPES: From Dangling Bonds to Oxygen Islands to 2D SiO_x Layer to the Onset of Bulk SiO_2 Formation

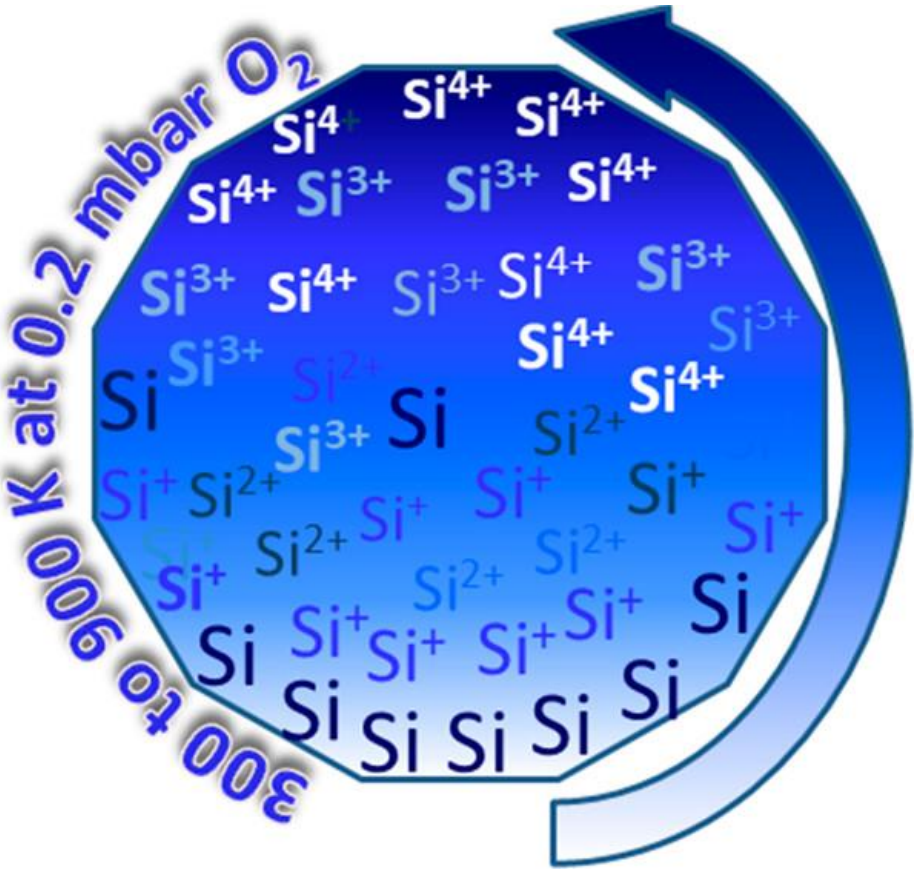

A part of the work presented in chapter 4 is published, and publication details are:-

Ghosalya, M. K.; Jain, R.; Reddy, K. P.; Gopinath, C. S., Silicon Oxidation by NAPPES: From Dangling Bonds to Oxygen Islands to 2D SiOx Layer to the Onset of Bulk SiO_2 Formation. *J. Phys. Chem. C* **2018,** *122*, 4331-4338

4.1. Introduction

Silicon has unique ability to form a protective SiO_2 layer on the surface, and advance MOS (metal oxide semiconductor) technology, and VLSI (very large scale integration) is based on the extraordinary properties of the Si−SiO_2 interface layer. Properties of the Si-SiO_2 interface are controlled by the atomic composition, electrical properties, and Si−O bonding features. Although these features have been explored quite well in the past, however, there are many issues remain unresolved. Therefore, a deep understanding of physics and chemistry of Si-SiO_2 interface is required. SiO_2 layer can be grown on Si surface thermally, but controlling the thickness and defect free SiO_2 layer on Si substrate are still a challenging task. For the fabrication of defect-free SiO_2 layer with a controlled thickness, it is necessary to understand the kinetics of Si oxidation from the initial elemental Si to SiO_2 layer formation with an understanding of the nature of adsorbed state of oxygen. Therefore, Si−O_2 interaction is the central point of surface science studies.[1−3] Although many Si−O_2 interaction studies has been reported in the past, no study has been reported in the presence of molecular oxygen at pressures close to ambient pressure and the present efforts fill that gap. By leaving Si in the atmospheric pressure at 1 bar, it is known to form SiO_2 layers on the surface; however, how the gas-solid interaction between O_2-Si begins, nucleates and growth occurs is not known. How the ϕ and electronic nature of surface changes as a function of surface oxidation is important to understand the device making, as well as device failure. In addition, silica is known to be an inert support in catalysis; however, how the surface dangling bonds interacts with the adsorbed oxygen molecules is of immense importance to the fundamental phenomenon of catalysis. Globally many efforts have been made to understand the kinetics of Si oxidation and properties of the Si-SiO_2 interface. On 1965, Deal and Grove proposed a mathematical model for thermal oxidation kinetics of single crystal substrate.[4] However; this model is useful only for single crystal surfaces. In case of thinner layer, the Deal and Grove model has been modified, and several other models have been proposed subsequently.[5−7] The adsorption of oxygen molecule on Si surface is the first step of oxidation; however, due to the lack of availability of precision tools to identify the mechanism of early stage oxidation and bonding configuration of initial adsorbed oxygen was not possible. This is also the main

interest of surface science studies and still unresolved. NAPPES can immensely help to pursue the oxygen interaction with the semiconductor surface, especially with NAP-UPS. UPS have few distinct advantages over the XPS, such as very low probing depth and high resolution, and the valence band spectra provide a wealth of information about chemical bonding, hybridization, work function, E_F, etc. In view of this, NAP-UPS was employed extensively in the present study to explore the Si oxidation process in the presence of gas-phase oxygen partial pressure up to 0.2 mbar and evaluated Si−O_2 interaction.

Si-oxygen interaction has been studied by NAP-UPS, NAP-XPS, and angle-dependent NAP−XPS. In the current study, we attempted to address three major points of Si oxidation. First point is on the nature of initially adsorbed oxygen at NAP conditions. The second point is the kinetics or progress of Si oxidation as a function of temperature and pressure. The third point is focused on the composition of various silicon species due to the oxidation at 0.2 mbar of O_2 pressure and high temperatures (800−900 K). There is general consensus for well-ordered 7 × 7 Si(111) surface that oxidation of Si surface takes place via molecular adsorption of oxygen followed by the dissociative adsorption and finally incorporation of oxygen atom in Si−Si bond.[8,9] However, there is no consensus on the fate of chemisorbed oxygen. This chemisorbed oxygen can directly dissociate to form atomic oxygen,[1,10] or it can dissociate via the negatively charged molecular precursor state.[2,3,11] According to theoretical studies both types of pathways are possible.[3,12] When the chemisorption takes place on the dimer−bridge site it immediately dissociated to atomic oxygen; however, if the oxygen adsorption occurs on nondimer bond site, it dissociated via metastable precursor to atomic oxygen.[13] Present study indicates that there are dangling bonds present on the clean silicon surface, and initially, molecular oxygen adsorbs on these dangling bonds, also known as Höfer precursor; molecular oxygen dissociates at high temperatures and then the oxygen atoms are inserted in to Si−Si bond in a stepwise manner.

The second point is the kinetics of Si oxidation. The kinetics of dry Si oxidation is a temperature- and pressure-dependent phenomenon;[14] however no XPS/UPS measurements has been reported at pressures higher than 10^{-6} mbar. It is well-known that the oxidation of

the first layer is limited by the localized O_2 adsorption on dangling bond and phase transfer takes place at 973−1073 K from passive oxidation to active oxidation.[14−18] Current study demonstrates a localized molecular oxygen adsorption phenomenon that occurs at 300 K followed by a homogeneous 2D surface oxidation at 600 K; this is fully supported by changes in the O_2 gas-phase vibrational features. Bulk oxidation begins to occur above 800 K and ≥0.2 mbar oxygen pressure. Graded oxidation layers could be observed with highly oxidized layers present on the top surface. The third point is focused on the bulk Si composition after the oxidation at 0.2 mbar of O_2 pressure and 900 K. In the angle dependent XPS experiments it has been observed that Si is not fully oxidized to Si^{4+} and several other intermediate oxidation states are observed. Si^{3+} and Si^{4+} oxidation states are dominantly present on the surface; however, Si^{1+} and Si^{2+} present in the subsurface or bulk.

4.2. Experimental Section

The XPS spectra have been recorded with Al Kα and UPS spectra recorded with He I photons (hν = 21.2 eV) from a He discharge lamp. A cone with 1.2 mm aperture was fitted to the entrance column of R3000HP analyzer, and a sample to aperture distance of 1.5 mm was maintained for the present set of measurements. More details of the system can be found in our previous reports.[19,20] Silicon disc purchased from MaTeck, Germany and cleaned with argon ion sputtering by applying 5 mA current and 3 kV followed by vacuum annealing up to 1000 K.[21] After several cycles of sputtering and annealing the clean silicon surface was prepared and confirmed by XPS as well as UPS. UPS spectrum recorded for silicon surface is in excellent agreement with spectra reported in the literature.[2,8,22] No contamination was detected by XPS/UPS. In the present studies, photoelectron spectral measurements were carried out on Si surfaces up to 0.5 mbar of O_2 partial pressure (99.99% pure) and between 300 and 950 K temperatures. All spectra are calibrated with respect to E_F of gold surface and normalized against room temperature measurement data. All spectra were deconvoluted after subtracting the Shirley type background and Gaussian−Lorentzian (G−L) function for line shape. Angle dependent XPS was recorded by changing the sample surface angle.

4.3. Result and Discussion

4.3.1. Temperature-Dependent Oxidation at 0.1 mbar of O_2 Pressure

Figure 4.1 shows the results due to initial oxidation of silicon surface at 0.1 mbar oxygen pressure between 300 and 700 K. NAP−UPS studies provide plenty of information about the molecular level interaction between the gas-phase molecules and solid surfaces under in situ or operando conditions. In Figure 4.1a, the first spectrum (black) shows the UHV valence band (VB) spectrum of the clean silicon surface recorded at 300 K. In this spectrum, a broad peak is observed between 0.3 and 3.7 eV, which is attributed to surface state or dangling bonds.[1,23-25] High intensity peak centered at 6.5 eV arises due to Si VB. VB features observed is in good agreement with the data reported in the literature.[1,2,8] In the presence of 0.1 mbar oxygen pressure at 300 K significant changes are observed in the VB spectra of silicon. Intensity of the dangling bond feature is reduced to one-third of that of clean Si surface. A significant shift in Si VB to 5.5 eV along with peak narrowing was observed. A new broad peak centered at 12.2 eV arises and also can be seen the oxygen gas phase vibrational features (corresponding to π-antibonding) around 8.0 eV. A careful look at the feature at 12.0 and 13.8 eV reveals the presence of not so well-resolved additional vibrational features of oxygen molecules from π-bonding and σ-bonding orbitals, respectively.[26] However, all vibrational features observed due to bonding and antibonding orbitals are well-resolved for gas-phase oxygen molecules in the absence of the Si surface. In comparison to pure gas-phase O_2 NAP−UPS spectrum, the O_2 on the silicon surface shows not only broadening, but also shift toward lower BE By 0.4 at 7.43 eV. It is to be noted that binding energy of the most intense O_2 vibration feature (observed at 7.82 eV for pure O_2 without Si or any surface) is always referred to indicate the changes observed. All these observations are indicating the onset of changes in the electronic nature of Silicon surface even at ambient temperature and 0.1 mbar of O_2 pressure.

The change in the vibrational spectra of O_2 on the surface with respect to pure gas phase spectra can be corroborated with the change in the nature of Si surface due to gas-lattice interaction and hence significantly different surface potential of oxidized Si surface.[20] An increase in Si surface potential by 0.4 eV due to oxygen adsorption at 300 K is deduced from

the shift in gas-phase vibrational features to lower binding energy. The feature at 12.2 eV is attributed to the molecular precursor state or well-known Höfer precursor state; our results are in good agreement with the earlier experimental and theoretical results.[8,27,28] A simultaneous decrease in the intensity of dangling bond feature and appearance of Höfer state corroborates well and underscores the molecular precursor state of oxygen. The full-width at half-maximum (FWHM) of O_2 gas phase vibrational features on Si surface also increases compared to the pure gas-phase feature; this demonstrates the heterogeneous nature of silicon surface due to O_2-Si gas-solid interaction. At least two chemically different surface sites are discernible; one with oxygen covered and the other without or less oxygen. Gas-phase features are broadened so much that the vibrational features from any of the bonding state is merged into a feature-less broad bands at 11.9 and 13.5 eV. These results shows a good correlation with results published by other groups using STM,[29] polarization- and shows a good correlation with results published by other groups using STM,[29] polarization- and photon-energy-dependent UPS,[30] and Kelvin probe microscopy.[11,31] Further increase in the temperature to 400 K results in a decrease in the intensity of Höfer precursor state as well as it becomes narrow; in addition a new peak observed at ~9.3 eV (indicated by dotted arrow in Figure 4.1a). According to literature reports,[1] this peak is attributed to oxygen insertion in Si-Si bond. Simultaneously, the gas phase vibrational spectra broadened and shifted further down to 7 eV compared to 7.44 eV at room temperature. However, the Si VB remains observed at the same BE; a shoulder is observed at 3.7 eV, which disappears on heating to high temperatures, and we do not know the reason for this feature. Intensity of the dangling bond feature decreased further, compared to the spectrum recorded at 300 K and 0.1 mbar pressures. The π-antibonding feature broadens to the level that it cannot be resolved into individual vibrations. The shift in the vibrational feature can be correlated to a further increase in the ϕ of the surface due to high temperature. Similar changes in ϕ were reported by Sturm et al.[31] by using Kelvin probe force spectroscopy. They demonstrated the initial ϕ increases with temperature because of the presence of Höfer precursor state. It is also to be highlighted that oxygen insertion into silicon, oxygen island formation, patches of remaining pure Si islands all coexists around 400 K and leads to broadening of VB as well as oxygen vibration

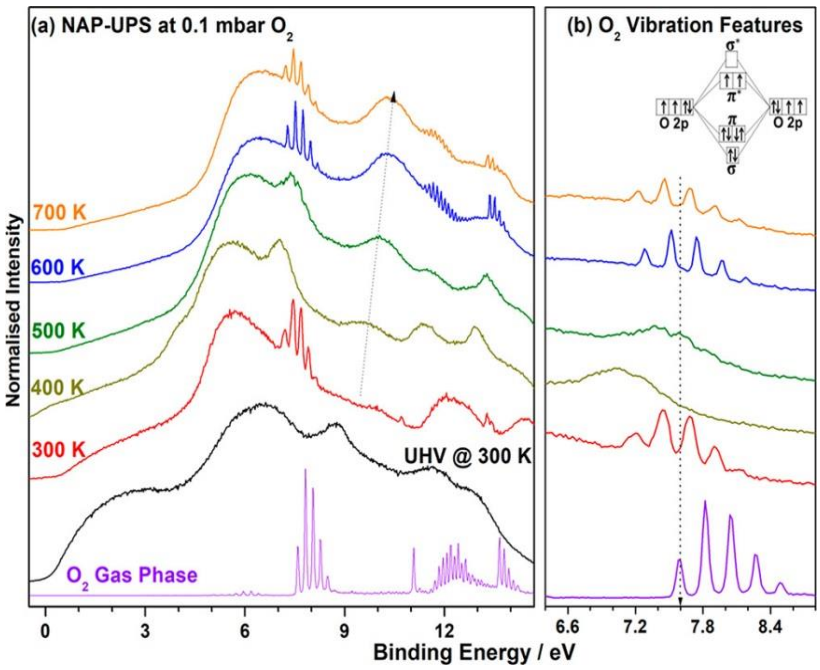

Figure 4.1: (a) Temperature-dependent Si valence band spectra at 0.1 mbar of O_2 pressure recorded with He I (hν = 21.2 eV) photons. The black color spectrum represents the clean Si VB in UHV at 300 K and gas-phase O_2 spectrum is given for reference. (b) Shift and broadening observed in the gas phase spectra of O_2 is shown in the enlarged manner; dotted arrow drawn is for the guide to eye. It is to be noted that BE of the most intense O_2 vibration feature (observed at 7.82 eV) is always referred to indicate the changes observed. Inset shows the MO diagram of O_2.

features. This could also lead to local variation in ϕ and hence complicate the analysis. When the temperature was further increased to 500 K, surprisingly the gas phase vibrational spectra begin to shift to higher BE to 7.32 eV. Nonetheless, the gas phase vibrational feature remain observed to be broad at 400 K (Figure 4.1b). The feature due to Si−O−Si is shifted to ~10 eV with an increase in the intensity; whereas the peak at 12.15 eV was shifted to lower BE, as well as the intensity decreases drastically. Si VB also shifts to higher B.E. by 0.3 eV. VB shift and gas-phase vibrational features shift in the same direction underscores the change in the electronic nature of the surface. The dissociation of Höfer precursor leads to a decrease in the ϕ which can be correlated with the shift or gas phase spectra toward the higher BE in Figure 4.1b. These results are indicating that the Höfer precursor state is quite stable at least up to 400 K, and at 500 K it begins to dissociates in to –Si=O species (Si^{2+}) which leads to a decrease in the ϕ.[11,31]

An important observation to be underscored from the NAP− UPS results is the broadened vibrational features of oxygen molecules. From the sharp features observed for reference gas phase spectrum recorded for O_2, extent of broadening on the Si surface increases from 300 to 500 K. In fact, the broadening is so much that all the vibrational features are clubbed into one broad envelope. Without a detailed fitting procedure it is difficult to make out how many different environments could be present on the surface; these details are discussed latter with Figure 4.2. Another observation to be noted is the relative higher intensity of antibonding orbital features of gas-phase oxygen molecules than the bonding orbital features throughout the temperature and pressure regimes employed in the present work. This is attributed to the following: while removal of electron from antibonding (or nonbonding) orbital enhances the bonding character, it is exactly the opposite while removal of electron from bonding orbitals. In other words, while bonding is improved or at least unperturbed by removing electron from the antibonding orbitals; however, bonding is significantly perturbed by removing electron from the bonding orbitals.[26] These changes are attributed to relatively low intensity for bonding orbital vibrational features of oxygen than the antibonding features. It is also to be indicated that the dangling bond feature maintained the same intensity up to 800 K, after initial reduction in intensity. It is known that the oxidation of Si surface is localized and form islands/patches on the oxidized surface. Therefore, the nature of surface changes to be heterogeneous and the same is the reason for the broadened gas phase vibrational features. At least two different surface features due to different extent of oxidation are possible. Surprisingly, when the temperature increases to 600 K, the gas-phase vibrational features fully reverts back to be narrow and shifted toward high BE to 7.54 eV; high BE features of gas-phase oxygen also reappears at 600 K. Gas-phase features at 600 K are very similar to reference O_2 spectrum. At 700 and 800 K, the NAP−UPS results are similar to that of the results observed at 600 K.

The fitted data is shown in Figure 4.2. The FWHM of these peaks is kept constant and as that of pure gas phase vibrational features. Energy gap between vibration features of one set of gas-phase O_2 molecules on Si-surface also remains that of pure gas-phase features. It can be clearly seen that when the oxygen dosed on silicon surface at 300 K, each vibrational

feature split at least into three peaks and indicating that three different types of surface Si species are present. When the temperature increased to 400 K, the gas phase vibrational spectra shifted to lower binding energy, as well as broadened more. At 400 K, each vibrational peak split into four peaks, which indicate that there are four different types of surfaces present on silicon surface. Similar type of splitting was observed at 500 K. At 600 K, the vibrational spectra become resolved much better than spectrum recorded at 300 K, and shifted toward higher binding energy. This indicates the reduction in the heterogeneity of the surface at 600 K and above. A predominantly homogeneous 2D oxidation layer occurs on the Si surface; in fact a major and a minor vibration features was fitted. At 700 K, vibrational spectra gets broadened and fitted with three peaks. The present observations may be critical and relevant to understand some of the important aspects of heterogeneous catalysis. For example, when the catalyst surface itself undergoes electronic and/or chemical changes due to adsorption/ interaction with the reactant(s) and/or products, the work function also changes significantly. Further the surfaces that are modified due to the above interaction influences the electronic and vibrational levels of reactant molecules. This underscores the nature of catalyst surfaces, especially highly reactive material surfaces, are moderate to completely different under reaction conditions, compared to the fresh catalyst surfaces; current efforts provides some light on such changes. Observation of such dynamic changes is possible exclusively due to the deployment of NAP−UPS. Cu−O_2,[20] Pd−O_2,[32,33] Co−O_2,[34,35] Ag−O_2,[36] CO oxidation on Co_3O_4,[37,38] and H_2 on ceria zirconia[39] show similar changes, and they are reported in our earlier reports. Recently, the 2D materials, like graphene, MoS_2, and h-BNx, has attracted a significant attention due to indispensable role of them in energy,[40] environment, and catalysis.[41,42] The chemical and electronic property of 2D materials can be modulated by several methods, such as doping with an heteroatom, introducing a functional group.[41] Introduction of a particular type of functional groups on graphene layers could change the surface potential, work function and hence reactivity. The present approach demonstrates the efficacy of NAP−UPS as an effective diagnostic tool to understand the above aspects. Particularly, how these materials behave in the presence of reactants can be explored in full detail. Further, charge transfer, in situ growth of 2D material on different substrates,

electronic and chemical changes of substrate and 2D material in the presence of reactant molecules are important aspects and they can be evaluated with NAP−UPS. Si 2p and O 1s core level spectra were also recorded parallel under 0.1 mbar of O_2 pressure at different temperatures and the results are presented in Figure 4.3. Si 2p core level spectra recorded under UHV-300 K and at 0.1 mbar of O2 pressure at 300 K are similar and BE of Si 2p was observed at 99 eV corresponding to Si^0; however, O 1s core level shows a peak at 531.1 eV indicating the possibility of peroxide like linkages. This supports the Höfer precursor state for molecular oxygen on Si surfaces. In contrast to the significant changes observed in NAP−UPS under the same conditions (Figure 4.1) NAP−XPS do not show any change; it is attributed to the exploration of predominantly bulk (up to 7−8 nm) layers, which is unaffected by the gas-lattice interaction that occurs on the surface between oxygen and Si. This result shows the importance of NAP−UPS over NAP−XPS for the study of oxidation mechanism of the semiconductor/material surface under relevant conditions.

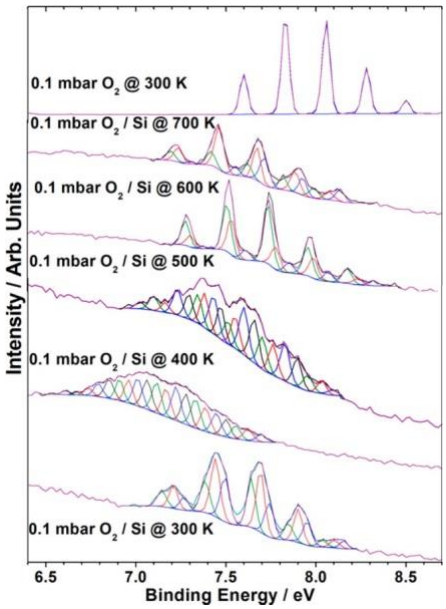

Figure 4.2: Fitted oxygen gas phase vibrational spectra at 0.1 mbar (pure gas phase and on Si surface) and at temperatures between 300 and 700 K.

On increasing the temperature to 400 K, O 1s and Si 2p core levels were broadened and observed at lower BE by 0.3 eV than that observed at 300 K. On increasing the temperature between 500 and 700 K, Si 2p and O 1s core levels shift toward higher BE than

that observed at 400 K. In addition, Si 2p core level displays a weak and broad peak at higher BE between 101 and 102 eV. Si 2p shows a peak at 101.2 eV (at 500 K) and this is attributed to Si^{2+} state. However, at 600−700 K, a low intensity feature is observed at 102.2 eV in Si 2p core level and it is attributed to further oxidation to Si^{3+}. Higher BE feature due to oxidized silicon is in good agreement with -Si=O and Si−O−Si features observed in NAP−UPS. All of these results indicate that Langmuir type of adsorption takes place below 600 K; in other

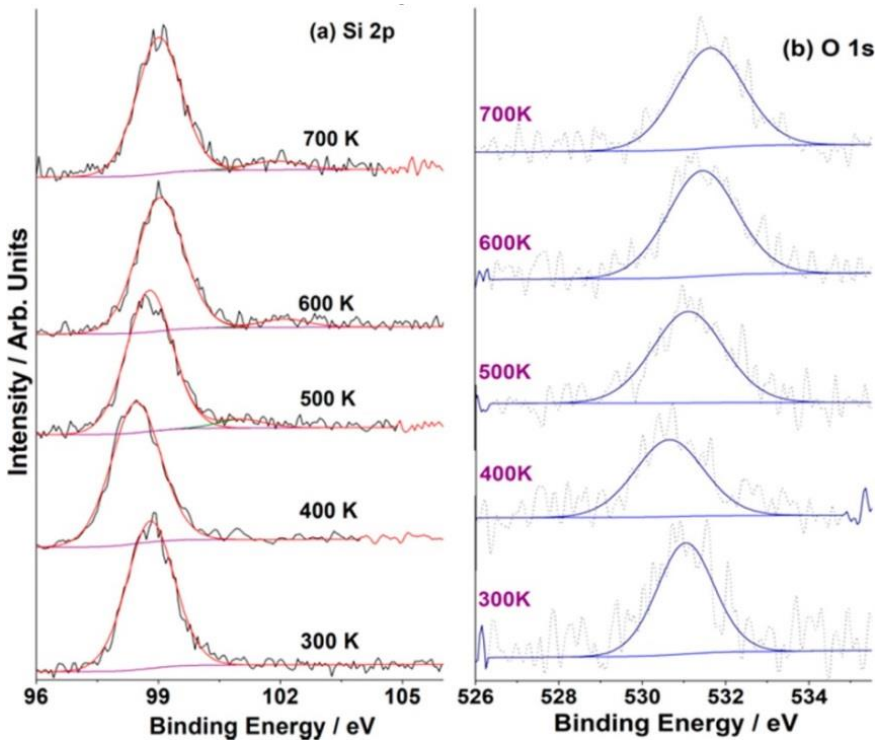

Figure 4.3: (a) Si 2p, and (b) O 1s core level spectra recorded at 0.1 mbar oxygen pressure between 300 and 700 K.

words, oxide grow randomly where dissociation of Höfer precursor takes place and form –Si=O (Si^{2+}) species. However, at 600 K, −Si=O dissociates, and oxygen migrate from the preferential site to form uniform 2D oxide layer on Si surface.[16,17,43] This is fully supported by the reappearance of narrow vibrational features of oxygen molecules underscoring the homogeneous nature of the surface. Therefore, gas phase vibrational spectra become well resolved between 600 and 800 K. On further increase in the temperature up to 800 K, minor change in the vibrational features was observed and no other significant surface changes were observed.

4.3.2 High Temperature and High Pressure (0.5 mbar) Oxidation.

Very limited oxidation occurs on the Si surface up to 800 K in the presence of 0.1 mbar of O_2 pressure (Figures 4.1−4.3). Indeed no Si^{4+} was observed under the above conditions indicating the requirement of more severe oxidizing conditions for the propagation of oxidation to subsurface and bulk layers. Within the current experimental limitations, these aspects are studied between 800 and 900 K from 0.2 to 0.5 mbar of O_2 pressure. Interesting results are observed in the NAP−UPS valence band measurements under the above conditions and the results are displayed in Figure 4.4. When the temperature is increased from 300 to 850 K at 0.2 mbar and remained there for 30 min, following interesting changes is observed. (a) Dangling bond feature observed at 300 K, completely disappeared after 30 min at 0.2 mbar of O_2 pressure at 850 K. Kinetics of dangling bond disappearance is really slow that just attaining 850 K in 0.2 mbar of O_2 pressure (850 K/0 min) was not sufficient. (b) A major change observed in the work function and the same increased by 1 eV at 850 K/30 min compared to 300 K (indicated by two dashed arrows in Figure 4.4). (c) O_2 gas-phase vibrational feature shifted from 7.4 to 6.15 eV, fully supporting the change in work function due to surface oxidation. (d) A weak feature observed at 10.15 eV at 300 K increased in intensity and shifted to 10.9 eV at 850 K/30 min.; thereafter, it remained at the same BE, irrespective of higher pressure (0.5 mbar) and temperature to 900 K. (e) Valence band remains observed at the same BE; however, the intensity of the main valence band increases up to 850 K/30 min and it is attributed to the O 2p feature from the silica layers. This enhancement in intensity is attributed to the silica formation on the surface. Photoionization cross section[44] of Si 3p (0.3269 Mb) and O 2p (10.67 Mb) fully supports an increase in the intensity due to the hybridization of Si and O orbitals. (f) σ and π-bonding vibrational features broadens to a large extent and single broad features were observed; while antibonding vibrational features were broadened and observed with low intensity, even at 900 K. All these observation underscoring the onset of bulk oxidation; however it is still limited to few layers, which is discernible from the corresponding XPS data shown in Figure 4.5. 0.2 mbar oxygen dosed for 90 min at 850 K shows no further changes indicating thermodynamically limited oxidation. O_2 pressure was increased to 0.5 mbar and held at 850 and 900 K; however, the

NAP-UPS spectra were recorded at 0.2 mbar pressure but at the same temperatures and the results are shown in Figure 4.4. Except for a minor increase in the work function by 0.1 eV, no other changes were observed and the valence band features remained the same. Corresponding XPS studies indicate an increased oxidation in the bulk layers, while surface layers remain the same.

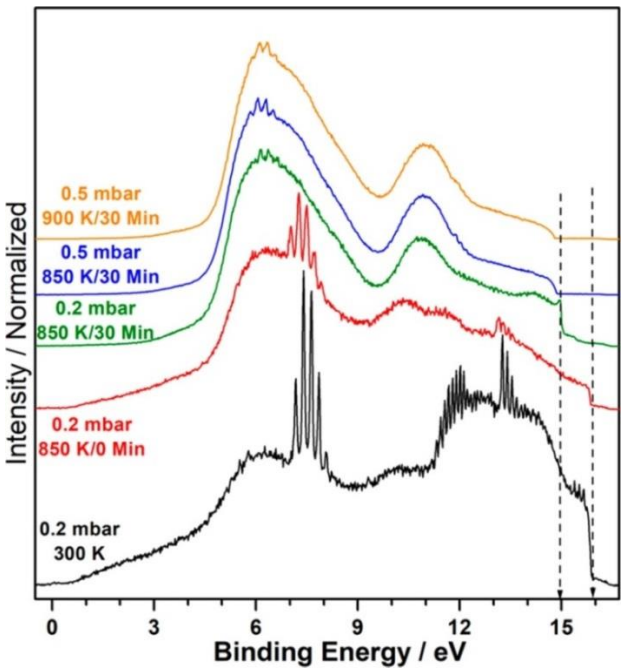

Figure 4.4: NAP−UPS spectra recorded at 0.2 mbar oxygen pressure between 850 and 900 K. Spectrum recorded at 300 K at 0.2 mbar is given for comparison. Two topmost spectra were recorded at 0.2 mbar, but after exposure to 0.5 mbar oxygen for 20 min.

Figure 4.5 shows the NAP−XPS spectra recorded under the same conditions employed as that of Figure 4.4. Deconvolution shows five peaks at 99.2, 100.5, 101.3, 102.5, and 103.4 eV which are due to elemental Si, Si^{1+}, Si^{2+}, Si^{3+}, and Si^{4+}, respectively. It is evident that the intensity of highly oxidized silicon (Si^{3+} and Si^{4+}) features increases with increasing severity of the oxidizing condition. Nonetheless, it is also evident that elemental silicon is still largely present within the probing depth of 7−8 nm (Figure 4.6). However, a comparison of the results obtained under same conditions between NAP−UPS and NAP−XPS suggests the complete oxidation of silicon on the surfaces, possibly to 3+ and 4+ valence states (Figure 4.6). This is fully supported by the large change in work function observed in NAP−UPS.

Low intensity peaks for lower valent (1+ and 2+) silicon hints its presence at the interface of oxide and elemental silicon, at the bulk. This aspect is further supported by the angle-dependent NAP−XPS measurements, and it is discussed later.

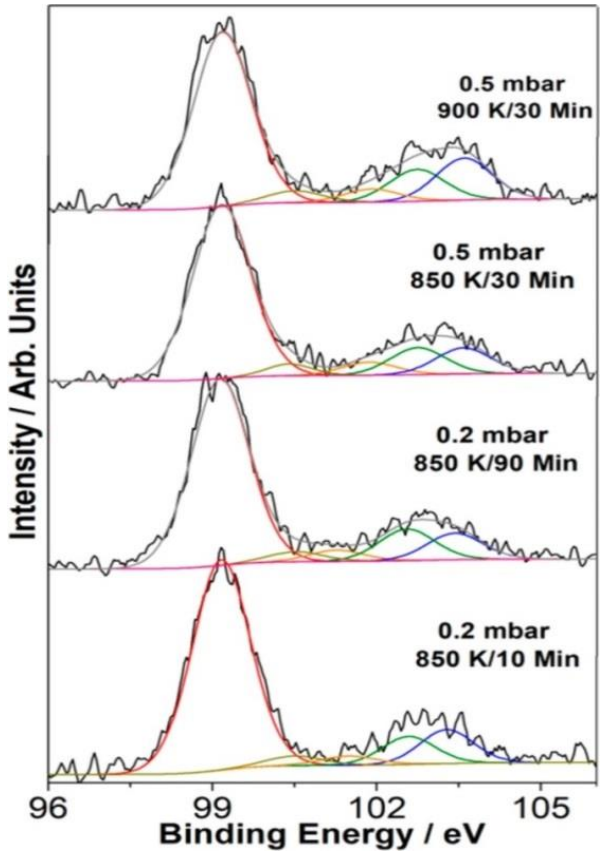

Figure 4.5: Si 2p NAP−XPS spectra recorded between 0.2 and 0.5 mbar between 850 to 900 K. Deconvolution shows an increasing extent of oxidation in the bulk with predominant 3+ and 4+ oxidation state of silicon.

Surface oxidation states of silicon observed in Figure 4.4 is quantified and the results are given in Figure 4.6. In NAP−XPS, it can be observed that initially at 0.2 mbar of O_2 pressure at 850 K (10 min.), 74% elemental silicon is present. However, with increasing O_2 pressure up to 0.5 mbar and temperature up to 900 K (30 min.), the percentage of elemental silicon decreased to 65% and other oxide species percentage increased. High oxidation state species increases from about 10 to 15%, while that of low oxidation states increased from 3 to 4% with increase in the severity of the oxidation conditions.

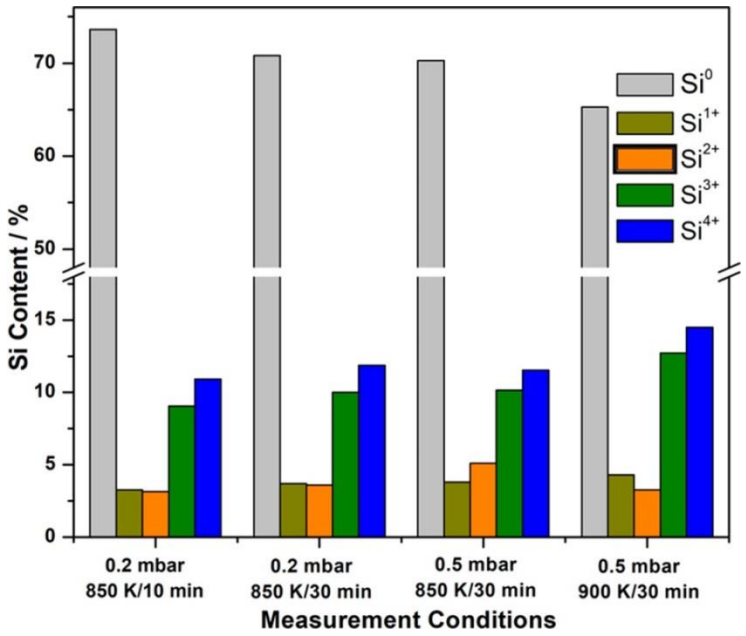

Figure 4.6: Percentage of elemental silicon and oxidized silicon species as a function of oxidation time and temperature and oxygen pressure.

To understand the mechanism of oxidation propagation and composition of oxidized silicon layers, angle-dependent XPS study was carried out at 900 K at 0.5 mbar and the result is shown in Figure 4.7. At normal emission angle (Figure 4.6, 900 K at 0.5 mbar/30 min) 35% oxidized silicon species and 65% elemental silicon are present. When the angle of incidence of X-ray decreased gradually from normal to grazing, the amount of elemental silicon decreased and that of oxidized silicon species increased. At the lowest angle of incidence at 20°, the amount of elemental silicon decreased to 48 %, and the oxidized silicon increased to 52 %. It is to be noted that there is no complete oxidation of Si to oxidized silicon species was observed within the XPS probing depth under the present experimental conditions. However, it is evident from the spectral data shown in Figure 4.7a that close to the surface, Si^{4+} and Si^{3+} are present predominantly and almost equal in amount. There is a surface gradation in the oxidized silicon species observed from top to the bulk layers. Highest oxidized species are present on the top surface and lowest oxidized silicon is present at deeper levels (or just above elemental Si layers) suggesting the introduction of oxygen between Si atoms are occurring one at a time. Oxidation from elemental to Si^{1+} to Si^{4+} requires increasingly severe conditions, in terms of both temperature and oxygen pressure. Between 850 and 900 K at 0.5 mbar

oxygen pressure, the oxidized layer thickness is measured to be between 2.4 and 3.2 nm. Indeed, our results are in good agreement with that of Enta et al. on 1.7−2.5 nm of SiO thickness between 573 and 723 K and at 1 Torr of O_2 pressure.[45] Because of the employment of Al Kα radiation (1486.6 eV), the probing depth is up to 7−8 nm and hence large amount of elemental Si was observed from the bulk layers in Figures 4.5−4.7. This also reiterates that after initial oxidation, the oxidation propagation into the bulk layers becomes really slow. This is also in good agreement with that of Enta et al.[45]

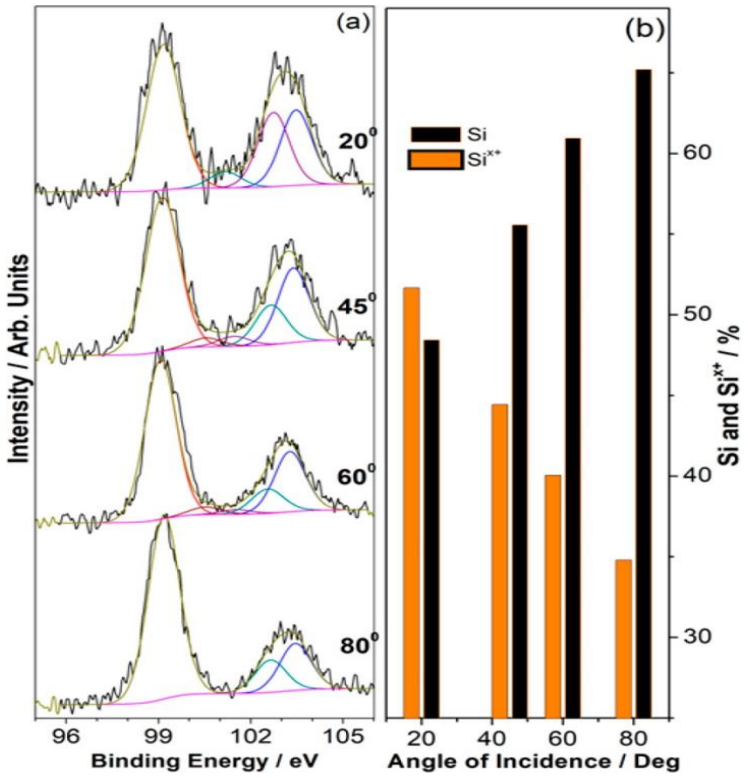

Figure 4.7: (a) Angle-dependent XPS spectra of silicon. (b) Percentage distribution of silicon oxide species as the function of incidence angle.

4.4. Oxidation Propagation Model.

On the basis of the experimental findings described in Figures 4.1−4.7 a possible oxidation propagation model is described in Figure 4.8. Clean Si surface is known to exhibit dangling bond (Figure 4.8a), which disappears on exposure to molecular oxygen at room temperature (Figure 4.8b). On heating the Si surface, in the presence of 0.1 mbar of O_2 pressure, leads to

oxygen covered islands; however, the surface is not fully covered with oxygen even up to 500 K (Figure 4.8c). This leads to heterogeneity of the surface and leads to broadening of vibration features of O_2 (Figures 4.1-4.2). On heating to 600 K, vibration features narrows to a near single vibration feature (Figure 4.2) with uniform surface oxidation to SiOx layer (Figure 4.8d). On further heating to 850−900 K and high pressures up to 0.5 mbar leads to begin the propagation of bulk oxidation (Figure 4.8e-f). In all these cases, initial oxidation appears to be very fast, which is supported by Enta et al.[45] observations. Nonetheless, the propagation of oxidation to bulk layers is slow.

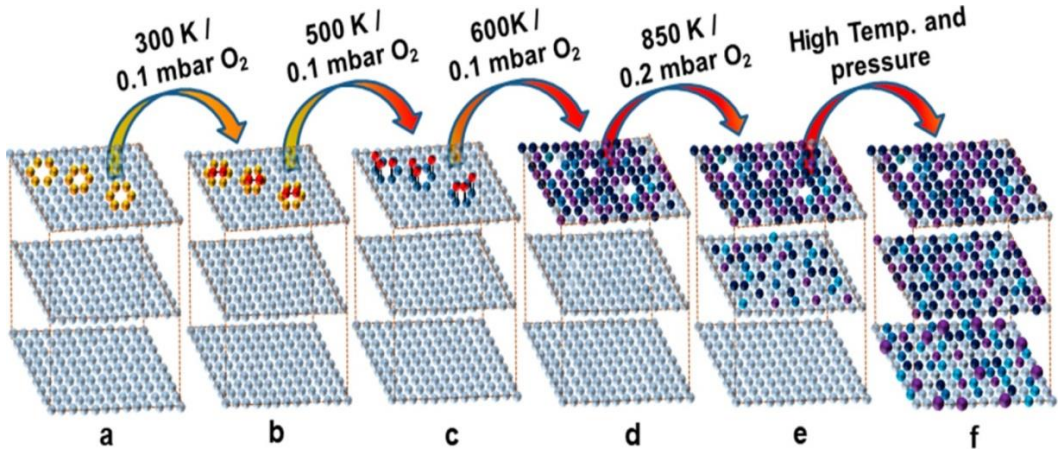

Figure 4.8: Model for various stages of silicon oxidation. (a) Bare silicon surface with dangling bonds associated Si atoms are shown in yellow color. (b) Preferential oxygen adsorption on dangling bonds at 300 K. (c) Oxygen islands formation occurs on heating to 500 K at 0.1 mbar of O_2. (d) Nearly uniform 2D layer of SiOx forms on heating to 600 K. (e and f) Onset of propagation of bulk oxidation beginning at 850 K and above at pressures higher than 0.1 mbar. Dark blue and purple indicates highly oxidized Si^{4+} and Si^{3+} species, respectively. Blue and bright blue indicates Si^{2+} and Si^{1+}, respectively.

4.5. Conclusion

An attempt has been made to study and explore the initial oxidation mechanism of Si by the NAP−UPS, NAP−XPS, and angle-dependent XPS. Our result indicates the molecular oxygen adsorption occurs on the dangling bonds of Si surface which leads to an increase in the ϕ from 300 to 400 K. Heterogeneous nature of surface oxidation is evident from the NAP−UPS results. However, a uniform 2D oxidized layer is evident from the results obtained at 0.1 mbar oxygen pressure and ≥600 K. This 2D layer acts as a protective layer for the inner or bulk

layers of Si, and prevent them from further oxidation up to 800 K. Between the above two regimes, the initially adsorbed oxygen dissociate to – Si=O species around 500 K. At temperatures higher than 800 K and pressures more than 0.1 mbar, oxidation begins to propagate into the bulk. Within the maximum operating experimental conditions employed in the present efforts, complete oxidation of Si to Si^{4+} was not observed within the probing depth of 7−8 nm; however, a gradation in the oxidation layers is observed with most oxidized on the top surfaces (Figure 4.8). More severe pressure and temperature are expected to increase the oxidation extent and follow the same trend reported in the present manuscript.

Present investigations reveal the changes not only on the solid surfaces due to gas-lattice interaction, but also with the interacting gas-molecules. Surface ϕ very much influences the electronic state of gas-phase molecules. Changes observed in the ϕ of lattice due to chemical/ electronic interaction with gas phase molecules, which in turn affects the electronic state of interacting gas molecules. To the best of our knowledge no such information has been obtained or published in the literature. Present studies are also relevant to any surface dependent applications, such as heterogeneous catalysis, electrochemistry, nanomaterials, and sensors. Particularly, 2D layered materials can be explored for change in work function, nature of charge transfer. When the lattice surface is highly reactive, interaction with reactive environments, such as oxygen, hydrogen, would lead to dramatic changes. It is also worth to underscore the nature of such surfaces are very different under relevant application conditions. Understanding this aspect would help one to design better quality material and material surfaces for surface-dependent applications.

Present study also indicates how difficult it is to form silica, found throughout the globe. Although present studies are limited to a maximum of 0.5 mbar and 900 K, we are surprised to learn the robustness of silicon to bulk oxidation. Needless to say that bulk oxidation of silicon would require much higher temperature at ambient O_2 pressure or possibly high pressure. Such drastic conditions are possible under non-ideal conditions, such as volcanoes, forest burning. It is possible that these types of conditions might have severely existed in the pre-historic periods. Although this point is not the objective of this chapter, it is a corollary conclusion derived from the present studies. It is also interesting paradox to learn

the easy oxidation of surface layers at very low oxygen pressures, but highly challenging to oxidize bulk layers of silicon. Indeed the same point protects the bulk silicon from getting oxidized under ambient conditions.

4.6. References

1. Tabe, M.; Chiang, T.; Lindau, I.; Spicer, W., Initial stage of thermal oxidation of the Si (111)-(7× 7) surface. *Phys. Rev. B* **1986**, *34*, 2706.
2. Morgen, P.; Höfer, U.; Wurth, W.; Umbach, E., Initial stages of oxygen adsorption on Si (111): The stable state. *Phys. Rev. B* **1989,** *39*, 3720-3734.
3. Höfer, U.; Morgen, P.; Wurth, W.; Umbach, E., Initial stages of oxygen adsorption on Si (111). II. The molecular precursor. *Phys. Rev. B* **1989,** *40*, 1130-1145.
4. Deal, B. E.; Grove, A., General relationship for the thermal oxidation of silicon. *J. Appl. Phys.* **1965,** *36*, 3770-3778.
5. Von der Meulen, Y., Kinetics of Thermal Growth of Ultra-Thin Layers of SiO2 on Silicon I. Experiment. *J. Electrochem. Soc.* **1972,** *119*, 530-534.
6. Kamigaki, Y.; Itoh, Y., Thermal oxidation of silicon in various oxygen partial pressures diluted by nitrogen. *J. Appl. Phys* **1977,** *48*, 2891-2896.
7. Maity, N.; Rajamohanan, P. R.; Ganapathy, S.; Gopinath, C. S.; Bhaduri, S.; Lahiri, G. K. MCM-41-Supported Organometallic-Derived Nanopalladium as a Selective Hydrogenation Catalyst. *J. Phys. Chem. C* **2008**, *112*, 9428−9433.
8. Höfer, U.; Morgen, P.; Wurth, W.; Umbach, E., Metastable molecular precursor for the dissociative adsorption of oxygen on Si (111). *Phys. Rev. Lett.* **1985,** *55*, 2979.
9. Silvestre, C.; Shayegan, M., Observation of a metastable precursor for adsorption of oxygen on Si (111) and the activation energy for chemisorption. *Phys. Rev. B* **1988,** *37*, 10432.
10. Schaefer, J.; Göpel, W., Initial stages of oxidation of Si {100}(2× 1): A combined vibrational (EELS) and electron binding energy (XPS) study. *Surf. Sci.* **1985,** *155*, 535-552.
11. Sturm, J.; Croes, G.; Wormeester, H.; Poelsema, B., Metastable precursor for oxygen dissociation on Si (001) 2×1 resolved by high lateral resolution work function measurements. *Surf. Sci.* **2007,** *601*, 2498-2507.

12. Barone, V.; Lelj, F.; Russo, N.; Toscano, M., Chemisorption of atomic and molecular oxygen on the (100) surface of silicon; a theoretical study. *Surf. Sci.* **1985,** *162*, 230-238.
13. Zheng, X.; Smith, P., The chemisorption behaviour of oxygen on the Si (100) surface. *Surf. Sci.* **1990,** *232*, 6-16.
14. Engel, T., The interaction of molecular and atomic oxygen with Si (100) and Si (111). *Surf. Sci. Rep.* **1993,** *18*, 93-144.
15. Takakuwa, Y.; Ishida, F.; Kawawa, T., Phase transition from Langmuir-type adsorption to two-dimensional oxide island growth during oxidation on Si (0 0 1) surface. *Appl. Surf. Sci.* **2003,** *216*, 133-140.
16. Enta, Y.; Miyanishi, Y.; Irimachi, H.; Niwano, M.; Suemitsu, M.; Miyamoto, N.; Shigemasa, E.; Kato, H., Real-time core-level spectroscopy of initial thermal oxide on Si (100). *J. Vac. Sci. Tech. A: Vacuum, Surfaces, and Films* **1998,** *16*, 1716-1720.
17. Engstrom, J.; Bonser, D.; Nelson, M.; Engel, T., The reaction of atomic oxygen with Si (100) and Si (111): I. Oxide decomposition, active oxidation and the transition to passive oxidation. *Surf. Sci.* **1991,** *256*, 317-343.
18. Suemitsu, M.; Enta, Y.; Miyanishi, Y.; Miyamoto, N., Initial Oxidation of Si (100)-(2× 1) as an Autocatalytic Reaction. *Phys. Rev. Lett.* **1999,** *82*, 2334.
19. Roy, K.; Vinod, C.; Gopinath, C. S., Design and performance aspects of a custom-built ambient pressure photoelectron spectrometer toward bridging the pressure gap: Oxidation of Cu, Ag, and Au surfaces at 1 mbar O2 pressure. *J. Phys. Chem. C* **2013**, *117*, 4717-4726.
20. K. Roy, C. S. Gopinath, UV photoelectron spectroscopy at near ambient pressures: Mapping valence band electronic structure changes from Cu to CuO. *Anal. Chem.* **2014**, *86*, 3683-3687.
21. Enta, Y.; Kinoshita, T.; Suzuki, S.; Kono, S., Angle-resolved ultraviolet photoelectron spectroscopic study of Si (001)-(2× 1)/K and Si (001)-(2× 1)/Cs surfaces. *Phys. Rev. B* **1989**, *39*, 1125.
22. Sakurai, T.; Hagstrum, H., Chemisorption of atomic hydrogen on the silicon (111) 7× 7 surface. *Phys Rev B* **1975**, *12*, 5349

23. Uhrberg, R.; Hansson, G.; Nicholls, J.; Flodström, S., Experimental Evidence for One Highly Dispersive Dangling-Bond Band on Si (111) 2× 1. *Phys. Rev. Lett.* **1982,** *48*, 1032.
24. Uhrberg, R.; Kaurila, T.; Chao, Y.-C., Low-temperature photoemission study of the surface electronic structure of Si (111) 7× 7. *Phys. Rev. B* **1998**, *58*, R1730.
25. Northrup, J. E., Origin of surface states on Si (111)(7× 7). *Phys. Rev. Lett.* **1986**, *57*, 154.
26. Hüfner, S., Photoelectron Spectroscopy – Principles and applications, p. 217, *3rd Ed*, Springer, Heildelberg, **2003**
27. Hoshino, T.; Nishioka, Y., Molecular adsorption and dissociative reaction of oxygen on the Si (111) 7× 7 surface. *Phys. Rev. B* **2000,** *61*, 4705.
28. Silvestre, C.; Shayegan, M., Observation of a metastable precursor for adsorption of oxygen on Si (111) and the activation energy for chemisorption. *Phys. Rev B* **1988**, *37*, 10432.
29. Dujardin, G.; Mayne, A.; Comtet, G.; Hellner, L.; Jamet, M.; Le Goff, E.; Millet, P., New Model of the Initial Stages of Si (111)-(7× 7) Oxidation. *Phys. Rev. Lett.* **1996,** *76*, 3782.
30. Avouris, P.; Cahill, D., STM studies of Si (100)-2× 1 oxidation: defect chemistry and Si ejection. *Ultramicroscopy* **1992,** *42*, 838-844.
31. Sturm, J. M.; Wormeester, H.; Poelsema, B., Heterogeneous oxidation of Si (1 1 1) 7× 7 monitored with Kelvin probe force microscopy. *Surf. Sci.* **2007,** *601*, 4598-4602.
32. Gopinath, C. S.; Roy, K.; Nagarajan, S., Can We Shift and/or Broaden the Catalysis Regime towards Ambient Temperature? *ChemCatChem* **2015,** *7*, 588-594.
33. Roy, K.; Jain, R.; Gopinath, C. S., Sustainable and Near Ambient DeNO_x Under Lean Burn Conditions: A Revisit to NO Reduction on Virgin and Modified Pd (111) Surfaces. *ACS Catal.* **2014**, *4*, 1801-1811
34. Dubey, A.; Reddy, K. P.; Gopinath, C. S., Ambient CO Oxidation on In-Situ Generated Co3O4 Spinel Surfaces with Random Morphology. *ChemistrySelect* **2017,** *2*, 533-536.
35. Reddy, K. P.; Jain, R.; Ghosalya, M. K.; Gopinath, C. S., Metallic Cobalt to Spinel Co_3O_4 Electronic Structure Evolution by Near-Ambient Pressure Photoelectron Spectroscopy. *J. Phys. Chem. C* **2017**, *121*, 21472-21481.

36. Ghosalya, M. K.; Jain, R.; Reddy, K. P.; Roy, K.; Gopinath, C. S., Subtle Interaction between Ag and O_2: A Near Ambient Pressure UV Photoelectron Spectroscopy (NAP-UPS) Investigation. *J. Chem. Sci.* **2018**, *130*, 30.
37. Jain, R.; Reddy, K. P.; Ghosalya, M. K.; Gopinath, C. S., Water Mediated Deactivation of Co_3O_4 Naonrods Catalyst for CO Oxidation and Resumption of Activity at and Above 373 K: Electronic Structural Aspects by NAPPES. *J. Phys. Chem. C* **2017**, *121*, 20296-20305.
38. Jain, R.; Gnanakumar, E. S.; Gopinath, C. S., Mechanistic Aspects of Wet and Dry CO Oxidation on Co_3O_4 Nanorod Surfaces: A NAP-UPS Study. *ACS Omega* **2017**, *2*, 828-834.
39. Jain, R.; Dubey, A.; Ghosalya, M. K.; Gopinath, C. S., Gas–solid interaction of H_2–$Ce_{0.95}Zr_{0.05}O_2$: new insights into surface participation in heterogeneous catalysis. *Catal. Sci. Tech.* **2016,** *6*, 1746-1756.
40. Khan, A. H.; Ghosh, S.; Pradhan, B.; Dalui, A.; Shrestha, L. K.; Acharya, S.; Ariga, K., Two-Dimensional (2D) Nanomaterials towards Electrochemical Nanoarchitectonics in Energy-Related Applications. *Bull. Chem. Soc. Jpn.* **2017,** *90* (6), 627-648
41. Fu, Q.; Bao, X., Surface chemistry and catalysis confined under two-dimensional materials. *Chem. Soc. Rev.* **2017,** *46*,1842-1874
42. Bharad, P. A.; Sivaranjani, K.; Gopinath, C. S. A Rational Approach Towards Enhancing Solar Water Splitting: A Case Study of Au-RGO/N-RGO-TiO_2. *Nanoscale* **2015**, *7*, 11206 −11215.
43. Ogawa, S.; Takakuwa, Y., Temperature Dependence of Oxidation-Induced Changes of Work Function on Si (001) 2× 1 Surface Studied by Real-Time Ultraviolet Photoelectron Spectroscopy. *Japan. J. Appl. Phys.* **2005**, *44*, L1048.
44. Yeh, J. J.; Lindau, I., Atomic subshell photoionization cross sections and asymmetry parameters: 1< Z<103. *Atom. Data Nucl. Data. Tables* **1985**, *32*, 1-155.
45. Enta, Y.; Mun, B. S.; Rossi, M.; Ross, P. N., Jr; Hussain, Z.; Fadley, C. S.; Lee, K.-S.; Kim, S.-K. Real-time Observation of the Dry Oxidation of the Si(100) Surface with Ambient Pressure X-ray Photoelectron Spectroscopy. *Appl. Phys. Lett*. **2008**, *92*, 012110.

Chapter 5

Gas-Solid Interactions with Reactive and Not-So-Reactive Gas Molecules: Near Ambient Pressure Ultraviolet Photoelectron Spectral Studies

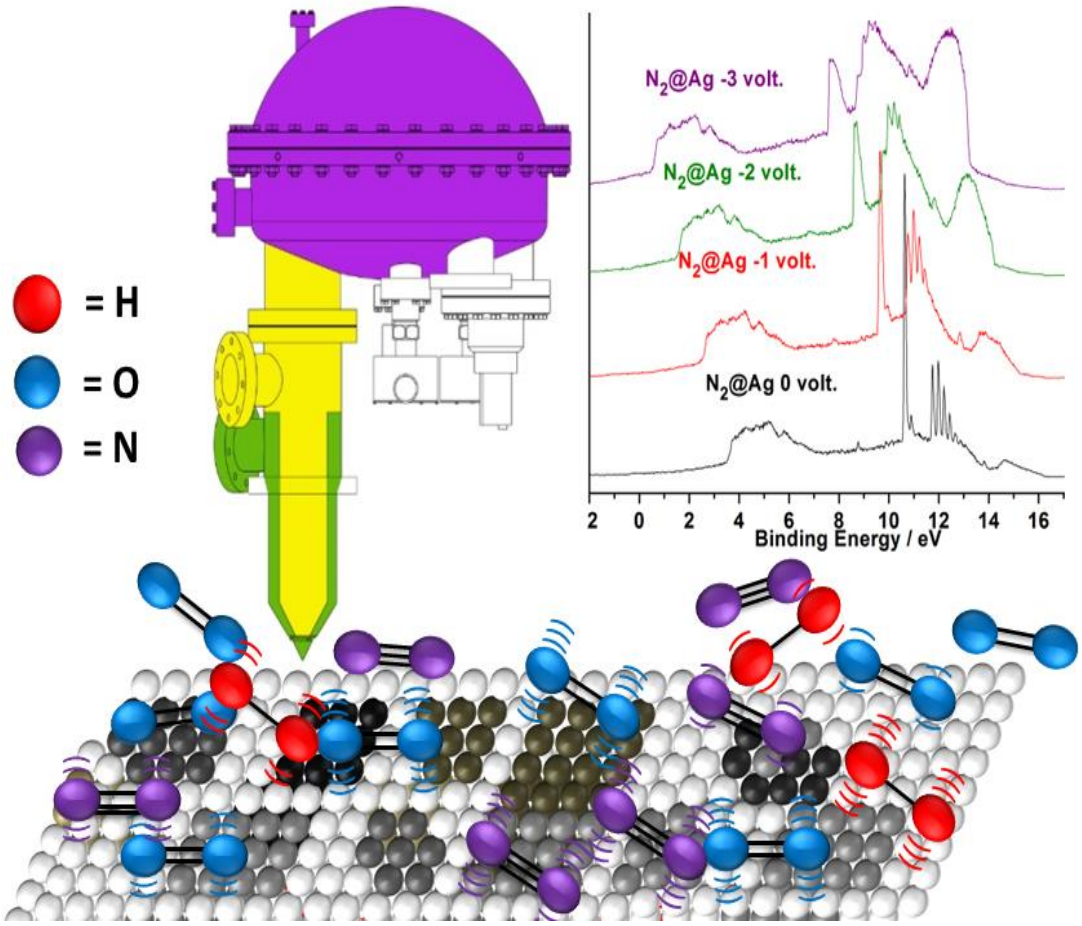

The work presented in chapter 5 is submitted to *J. Phys. Chem C* details are:-

Manoj Kumar Ghosalya, Kasala Prabhakar Reddy Nitin B. Mhamane, Ravi Ranjan, and Chinnakonda S. Gopinath[*] Gas-Solid Interactions with Reactive and Not-So-Reactive Gas Molecules: Near Ambient Pressure Ultraviolet Photoelectron Spectral Studies.

5.1 Introduction:-

There are numerous studies conducted on the molecular/atomic gas phase spectrum with various gases by using IR spectroscopy[1] and/or UVPES.[2] These type of studies are very much essential to understand the traces of atmospheric gases and their interaction with each other. However, gas-solid interaction forms the basis for surface-dependent phenomenon/properties, such as catalysis, electrochemistry, and nanomaterials. Simple adsorption of atmospheric components (O_2, CO_2, and H_2O) is known to affect the surface properties. Adsorption, particularly chemisorption, is the fundamental phenomenon for catalysis. However, not much is known about this important fundamental factor, and especially it is not evaluated at atmospheric pressure or closer to ambient pressures in a reliable manner. Real-world catalysis occurs under ambient pressure or high pressures, and it is essential to explore the gas-solid interaction in a reliable manner at real-world applied conditions or closer to that. Ertl and coworkers explained the non-linear changes in the catalytic activity for CO oxidation on Pt(110) surfaces through surface reconstruction by O-atoms under reaction conditions.[3] Gopinath et al. explained the changes in the nature of Pd surfaces due to the interaction between Pd and O_2 and the modified surface induces ambient temperature CO oxidation activity. It is also to be noted that Pd –surfaces are known to exhibit CO oxidation activity above 400 K.[4] Hence it is not necessarily the initial or the virgin catalyst surface is the active surface for the actual catalysis, and surface changes are most often inevitable under actual reaction conditions. Predominant number of catalysts surfaces is significantly different under reaction conditions, compared to its virgin counterpart.[5-7] Catalysis being a surface phenomenon, it predominantly depends on the surface nature. The elementary steps involved in any catalysis reaction, such as adsorption of reactants, dissociation, diffusion, desorption of products, involves bond-making and bond-breaking; they heavily depend on the nature of gas-solid interaction in heterogeneous catalysis. Indeed it is essential to evaluate the fundamental aspect to understand as well as to develop better catalysts.

For the present chapter, we have evaluated the atomic/molecular photoelectron spectrum of monoatomic (Argon gas), and some homonuclear diatomic molecules like H_2, O_2, and N_2 by using the NAPUPS. This work is divided into two parts. In the first part, we have

recorded the pure gas phase spectra of the gases mentioned above at 300 K with varying the pressure from $1x10^{-3}$ to $3x10^{-1}$ mbar. We made an unusual observation that with increasing pressure the BE of molecular orbital of all gases mentioned above has increased. However, when we recorded the NAP-UPS of these on the metal surfaces, surprisingly, no shift has been observed in the BE.

The properties of metal and metal oxide film and their interaction with atmospheric components have a lot of practical and fundamental interest in the heterogeneous catalysis,[8-11] solar cell[12,13] and semiconductor devices.[14,15] Especially the ϕ is the key electronic property to understand the relative Fermi energy[16] and charge carrier concentration[17] of the material which is highly surface sensitive properties. Because of the large dependence of ϕ on surface nature, it is a very important as well as challenging task to measure the accurate work function of the particular material under technically relevant conditions. The most prevalent technique to measure the ϕ is Photoelectron spectroscopy and Kelvin probe force microscopy (KPFM);[18] however; both techniques have stringent surface preparation conditions. The KPFM method depends on the potential change of the reference electrode; however, the inherent potential of the reference electrode can be affected by the contamination even in high vacuum. This applies very well to the electrochemistry measurements carried out with different electrodes at ambient conditions. In PES, the ϕ is generally determined by the secondary electron cutoff; however, because of adsorption of foreign particles or defect sites or heterogeneous nature of the surface, the shape of secondary electron cut off line in PES spectrum may not be a straight line. Under these conditions, the determination of secondary electron cut off line and ϕ measured may not be accurate. Hence in-situ prepared surfaces or in-situ cleaned surfaces offer the best solution and NAPUPS on such surfaces provide the accurate values. The other method for determining the ϕ like field emission and the PES of adsorbed xenon require UHV condition.

In the second part, we evaluated the influence of different solid surfaces on nature and energy position of electronic and vibrational features of interacting gas-phase atom/molecules. For these studies, we have chosen the two inert gases, namely homodiatomic N_2, and another one is monoatomic Ar gas. Both (Ar and N_2) shows ultralow sticking

coefficient across many metal/oxide surfaces and highly inert in nature, which is required to understand the influence of surface on the gas-phase molecules. Both gas phase spectra is recorded on the inert metal surfaces, like Ag and Au, semiconductor Si and SiO_2 surfaces, reactive metal Ni, Cu, Co and their oxides. In our previous studies, [4,15,19-22] we have observed that with change in the electronic nature of the surface, the BE of the electronic state of molecular gas-phase species also changes. However, in our previous studies mostly we used the reactive gases, such as O_2, CO_2, H_2, CO, on reactive metal/oxide surfaces.[4,15,19-22] Therefore, with change in the experimental condition these reactive gas-phase molecules reacts and changes the electronic nature of solid surface, which in-turn leads to a shift in the BE of the gas phase molecules in the resulting spectrum. In this particular work, we have chosen the inert gases (N_2 and Ar) interaction with above mentioned metal surface and their oxides. Particularly inert gases are chosen to minimize the complications that would arise due to the dynamic interaction between reactive gas molecules and the surface.

5.2 Experimental Section

All experiments are carried out in a custom built laboratory-based near-ambient pressure photoelectron spectrophotometer (NAPPES) unit installed in our laboratory at CSIR-National Chemical Laboratory, Pune. Design and performance of this system has been explained in detail in the references 21 and 23. The system is equipped with the differentially pumped Scienta R3000HP analyzer, capillary gas-doser, Al-Mg dual anode X-ray, monochromatic Al X-ray source, differentially pumped discharge lamp to generate He I and He II UV radiation source. The polycrystalline foils (Ni, Co, Si, Ag, Au, 99.999 pure) which are used in the experiments are procured from MaTeck, Germany. These foils are cleaned by the several cycles of Ar sputtering and annealing in UHV up to 1000 K. A series of sputter-anneal cycles produced clean metal foil surfaces which is confirmed by the XPS as well as UVPES. The metal foils are oxidized in the 1 mbar oxygen environment at the appropriate temperature. 99.99 % pure gases are used for all of the experiments. All spectra are calibrated with respect to Fermi energy and normalized against room temperature. All the UVPES experiments are carried out at 298 K temperature.

5.3 Electronic Spectrum of Gases

According to Born-öppenheimer approximation, the total energy of a diatomic molecule is the sum of $E_{electronic}$, $E_{vibrational}$, and $E_{rotational}$ energies. All these three energies of a molecule can be considered as completely independent of each other. So the total energy of a molecule can be written as:- $E_{total} = E_{electronic} + E_{vibrational} + E_{rotational}$

And the approximate orders of magnitude of these transitions are following:[24]

$$E_{electronic} \approx E_{vibrational} \times 10^{3} \approx E_{rotational} \times 10^{6}$$

On an electronic transition, the vibrational and rotational changes produce "coarse structure" and "fine structure" respectively. There is no quantum mechanical restriction on the change of vibrational quantum number during the electronic transition, therefore, there may be n (n =1,2,3….n) number of vibrational transitions are possible with different intensities. The Franck-Condon principle governs the transition, and the relative intensities of the lines depend on the position of potential well for the neutral atom and ionized species, giving the highest intensities where the bond length of ion is closer to that of the neutral species. Above changes happen within any two levels of diatomic or multi atomic molecules through excitation and these aspects has been thoroughly studied by IR, Raman, and UV-Visible spectroscopy for light absorption; similarly, light emission spectroscopy can be studied by fluorescence methods. However, in photoelectron spectroscopy, an electron is ejected from one of the core or valence level depending on the energy of the incident radiation employed. It is true that the X-ray induced core level spectrum arises from the valence band to deep core levels. However, UVPES spectrum arises exclusively from the valence band (for solids) or hybridized molecular orbitals (in molecules) and the valence orbital energy range generally fall in between 0-15eV, with reference to the vacuum level. In fact, the UVPES can provide the high resolution or fine structure spectrum than the core level XPS results. This is mainly attributed to the energy resolution and the energy width of the incident radiation. The relative intensity of spectral lines mainly depends on the type of molecular orbital and the vibrational states from which the electrons are ejected.

Figure 5.1(a) shows NAPPES of the hydrogen molecule recorded at 0.1 mbar. Indeed, hydrogen is the simplest molecule with only one fully-filled valence level/orbital and $1s^2$ electronic configuration. $1s^2$ level with vibrational fine structure is observed at a BE between 11 and 13 eV. When UV light is irradiated on hydrogen molecules, the electron is ejected from the bonding orbital leaving behind the H_2^+ ion. In other words, photoelectron spectroscopy measures the ionization energy of transition between the ground state of the neutral hydrogen molecule and excited electronic state of the ion. The transition takes place between v = 0 vibrational states of the neutral molecule to v' = 0 states of the ion. The required ionization energy for this process is known as adiabatic ionization energy. If the transition takes place from v = 0 to $v' \neq 0$ then the required energy for this excitation is known as vertical ionization energy. Mostly, the transition occurs from the v = 0 state of a neutral atom to one of several states of ion, which gives the approximately equally spaced bands of spectrum. Here, the number of lines in a spectrum depends on the number of transitions between several transition states. If the photoelectron is removed from the non-bonding orbital, the intensity of vibrational lines is concentrated almost entirely close to 0,0 line. Therefore, the first line will be more intense than the other and thereafter intensity will decrease in a regular manner for subsequent line. Whereas if the photoelectron removal occurs from the boning or antibonding orbital, the most intense line will arise from the v = 0 to $v' = n$ (n = 2, 3, 4… depending on the inter-nuclear separation between ground state and excited electronic state). Hence, the overall shape of the spectrum mainly depends on the inter-nuclear distance between the ground state and excited electronic states. Lowest to highest BE peaks originates from v = 0 to higher vibrational states. Highest intensity peak is observed for v = 2, and thereafter the intensity decreases for higher vibrational states, mainly due to lower population in those states. Beyond v = 12 states, the intensity is negligible due to dissociation of hydrogen molecules into hydrogen atoms and hence there is a continuum observed at high BE. This is in good correspondence with the results reported from Raman results. Koopmans's theorem suggests that for a closed-shell molecule, the ionization energy of an electron in a particular orbital is approximately equal to the orbital energy. In the case of

the hydrogen molecule, it is equal to the ionization energy of hydrogen to hydrogen ion. In the hydrogen spectrum, very low intensity satellite peaks are observed between 9 and 11 eV is attributed to the low intensity He-Iβ (23.06 eV) secondary radiation present along with He-I. The removal of an electron from the bonding orbital of hydrogen molecule induces a significant change in the molecular orbital; this leads to an increase in the bond length and weakens the bond strength, resulting in the wider and shallower potential well and with a lower vibrational frequency than the neutral molecule. In the hydrogen spectrum, the most intense feature could be that of where the bond length of ion is closest to the bond length of a neutral atom. However, the observed Raman line for neutral hydrogen molecule[25] is 4158 cm^{-1}. Whereas, in the H_2 UVPES spectrum, the energy gap between two successive lines is 0.26 eV which corresponds to 2097 cm^{-1}, which is about 50 % of that of neutral molecule vibration observed in the Raman spectrum. The electron in the H_2 atom is ejected from the bonding orbital which is the reason for the decrease in the bond strength.

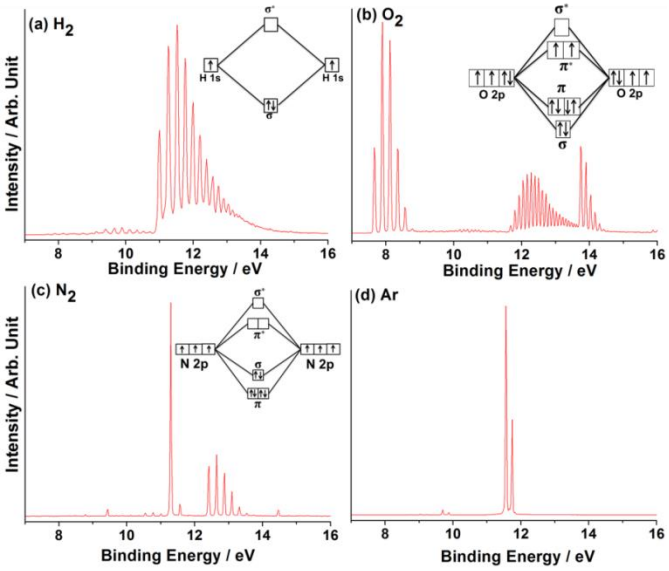

Figure 5.1: The gas phase photoelectron spectra recorded at 0.1 mbar pressure at room temperature. (a) The hydrogen spectrum represents the 1s σ orbital. Low intensity features observed between 9 to 10.5 eV is due to HeI_β satellite radiation associated with $He\text{-}I_\alpha$ (1.5 % intense as that of HeI_α); similar features are observed with other spectra given in this chapter. (b) Molecular oxygen gas phase spectrum arises from the $2p_\pi$*, $2p_\pi$, and $2p_\sigma$ orbitals from low to high BE, respectively. (c) Molecular nitrogen gas phase spectrum arises from $2p_\sigma$ and $2p_\pi$ bonds from low and high BE, respectively. (d) Monoatomic Ar gas phase spectrum features arise from fully-filled $3p^6$ spin-orbit coupled ($3p_{3/2}$ and $3p_{1/2}$) levels.

Figure 5.1b displays the photoelectron spectrum of gas-phase O_2 molecule. For oxygen molecule, all three types of orbitals (antibonding, bonding and non-bonding) can be seen. The oxygen molecule has a total 12 electrons in its valence shell. However, the 2s orbital electron remains non-bonded and considered as shallow core level; the He I photon does not have sufficient energy to eject the electron from O 2s orbital. Hence in Figure 5.1b, only three sets of vibrational features appear in the spectrum, at 7.5 eV, 11.8 eV and 13.7 eV and they are related to the fine structure of $2p_{\pi}$*, $2p_{\pi}$, and $2p_{\sigma}$ orbitals, respectively. Energy positions mentioned are for the highest intensity vibrational feature within a set of vibration features. The overall shape of the spectrum is governed by the equilibrium geometry between the initial and final state of the ionized molecule. Therefore, three different shape features can be seen in Figure 5.1b. All these transitions give the distinct fine structures that can be used for identifying the orbital. Feature at 7.5 eV is arising because of electron ejection from the $2p_{\pi*}$ antibonding orbitals. The removal of an electron from the antibonding orbital results an increase in the bond strength and leads to a decrease in interatomic distance in O_2 molecule. The an-harmonic oscillator potential well also became narrower and deeper and shifted to higher BE than the neutral molecule. The average energy gap between two successive vibrational features is around 0.23 eV which is equal to 1855 cm^{-1}. This frequency is significantly higher in energy from the fundamental rotational-vibrational Raman peak (Q line J = 0 pure vibrational excitation peak) for a neutral molecule which appears at 1556.2 cm^{-1}.[26] An increment in the vibrational frequency observed is apparently an indication for its relation with antibonding orbital. The second feature is observed at 12 eV. The shape of this feature is very similar to the hydrogen spectrum in Figure 5.1a. This spectrum is observed because of the electron ejection from the $2p_{\pi}$ bonding orbital. It is a known fact that when an electron is ejected from the bonding orbital, it leads to a decrease in the bond order and an increase in the interatomic distance. Because of the ejection of an electron from the bonding orbital, the potential well became broader and shallower and BE shifts towards the lower energy side, compared to vibration from a neutral molecule. This also can be confirmed by the energy gap between two successive vibrational features which is observed around 0.11 eV, which corresponds to 887.1 cm^{-1}. The third feature observed at 13.7 eV which arises due to the $2p_{\sigma}$

bond transitions. Here again, the electron is ejected from the bonding orbital which leads to a decrease in the bond order and associated increase in the interatomic distance and also responsible for narrow potential well. Indeed the narrow and broader potential well observed for $2p_\sigma$ and $2p_\pi$ is characteristic of σ and π bonds, respectively. The energy gap for these two successive vibrational features is 0.14 eV which corresponds to 1129.2 cm^{-1}. In this case, also the frequency is lower than the neutral molecule which indicates that this feature arises because of electron ejection from the bonding orbital which leads to weakening the bond strength.

Figure 5.1c shows the NAPPES for molecular nitrogen. The spectrum at 11.27 eV is corresponding to the $2p_\sigma$ orbital. The additional low-intensity features are related to the other vibrational state. Here, the energy gap between two vibrational lines is around 2091cm^{-1}. The second feature is also observed at 12.4 eV, which is corresponding to $2p_\pi$ bonding orbital. Here, also the energy gap between two successive vibrational lines in the spectrum is similar to $2p_\sigma$ orbital, which is 0.24 eV and corresponding to 1935 cm^{-1}. Both $2p_\sigma$ and $2p_\pi$ are bonding orbital but the vibrational energy difference in both peaks indicates the difference in bond strength. It is known that the bond length of neutral molecular nitrogen is 1.09769 Å; while the same changes for $2p_\sigma$ and $2p_\pi$ orbital final states in UVPES to 1.11642 and 1.1749 Å,[27] respectively. UVPES results and bond length changes are in full agreement with each other. Expectedly, the σ bond is stronger than the π bond, and σ bond features appear at higher energy/frequency than the π bond.

Figure 5.1d shows the UVPES spectrum for the first shallow level of Argon. Argon consists of the single atom with fully filled [Ne] $3s^2$ $3p^6$ configuration to give the simplest photoelectron spectrum. Expectedly there is no hybridization with another Ar atom and hence no vibration features. Ar spectrum arises because of electron ejection from the 3p orbital. This spectrum gives two lines due to spin-orbit splitting to $3p_{3/2}$ and $3p_{1/2}$ at 11.53 and 11.75 eV, respectively, with a full width at half maximum of 0.05 eV. In fact, the resolving power of electron energy analyzer can be studied with gas-phase Argon atoms; this particular analysis demonstrates the highest resolving power of R3000HP analyzer at NAP conditions, which is unique among several such spectrometers available. The coupling constant "J"

determines the intensity ratio of these two lines." Therefore the ideal intensity ratio for $3p_{3/2}$ and $3p_{1/2}$ is equal to two. The experimentally determined ratio is also equal to two. The energy difference between these two lines gives the spin-orbit interactions.

5.4 Effect of Pressure on Binding Energy of Vibrational Spectrum

Figure 5.2 (a), (b), (c) and (d) shows the NAPUPS spectra of H_2, N_2, Ar, and O_2 gases as a function of partial pressure between $1x10^{-3}$ and 0.3 mbar at 298 K. BE changes observed are shown in the corresponding a1-d1 panels. Below $1x10^{-3}$ mbar pressure, the spectral intensity is not observed or insignificant in intensity. Only Ar shows decent intensity at $1x10^{-4}$ mbar. It is challenging to get decent quality spectrum above 0.3 mbar due to limitations; high pressure limits the attenuation of photoelectrons reaching the detector due to large inelastic scattering. Hence the minimum and maximum gas pressures are limited between $1x10^{-3}$ to 0.3 mbar in our studies. In this region, we have observed that with increasing pressure from $1x10^{-3}$ to 0.3 mbar the vibrational features also shift towards higher BE side and this is the common observation for all four gases (diatomic and monoatomic). A breakpoint occurs at or around 0.1 mbar for all gases underscoring the change in nature of flow from molecular to viscous regime. However, the extent of BE shift is different for different gases. The shift in BE for H_2, N_2, Ar, and O_2 are 0.4, 0.7, 0.7 and 0.55 eV, respectively. Incidentally, inert N_2 and Ar shows the large increase in BE change (0.7 eV), while reactive H_2 and O_2 shows a relatively small increase in BE change (0.4-0.55 eV). The most probable reason for this BE shift is the change in the molecular flow to viscous flow during the change in pressure.[28] It is to be mentioned that the gas manifold is connected to the capillary gas doser via a z-axis manipulator in the analysis chamber.[23] The capillary of the gas doser inside the analysis chamber can be extended very close to the entrance slit/aperture or near the sample holder. It is earlier reported by Guevremont et al.[28] that in the pressure regime analyzed in the present work lead to a viscous flow of gases to certain distance (from the entry point of molecular beam doser) and until the expansion occurs. It is to be underscored that the molecular beam method employed by Guevremont et al[28] and in the present work are similar and gas expansion is expected. At the point of gas expansion from the capillary doser, the input gas behaves as a

condensed liquid and this is expected to lead to a change in the BE. However, at high pressures, this trend reverses, and present work also shows a reversal at the highest pressure employed (0.3 mbar).[29]

In Figure 5.2 it has been observed that with increasing pressure the gas phase spectrum shifts from their original position to the higher BE side. To understand this effect on solid surfaces another set of experiments is carried out and the results are shown in Figure 5.3. In this experiment, N_2 and Ar gas phase spectrum is recorded on Ag and Si surface while varying the pressure from 0.1 to 0.3 mbar. Reference gas-phase spectrum recorded at 0.3 mbar is shown in red traces. An interesting observation is made with the results shown in Figure 5.3. When the spectra are recorded (Figure 5.3a, b and c) on the metal (Ag) and semiconductor (Si) surfaces, surprisingly, there is no BE shift observed for both gas-phase atom/molecule at increasing pressure between 0.1 and 0.3 mbar. Several other interesting observations are made and they are listed below: (a) Both N_2 and Ar features appears at lower BE in the presence of solid surface compared to the reference spectrum given in red color. (b) N_2 on Ag shows more shift to lower BE (by 1.42 eV) than that of on Si-surface (0.67 eV). (c) Ar on Si surface shows lower BE shift (0.67 eV) compared to reference Ar spectrum. (d) Interestingly, vibration features of nitrogen molecules are maintained on Si and Ag surface at all pressure values; while spin-orbit splitting of Ar disappears and a broad feature appears on Si-surface. This is attributed to a possible weak adsorption of Ar on Si surface at such high pressures and hence the observation of line broadening. Indeed the VB of Si-features are high in intensity in the presence of N_2, while it is low in the presence of Ar, supporting a possible Ar-adsorption. It is well known in the literature that Xe adsorbs on catalyst surfaces and used as probe molecules.[30-32] (e) N_2 and Ar shows similar shift on Si indicating the possibility of reliable work function measurement by using them as probe molecules. Indeed, we suggest nitrogen could be employed due to its non-interacting and non-accumulating nature on surfaces and in pores; however, Ar and N_2 may be used to probe different sites.

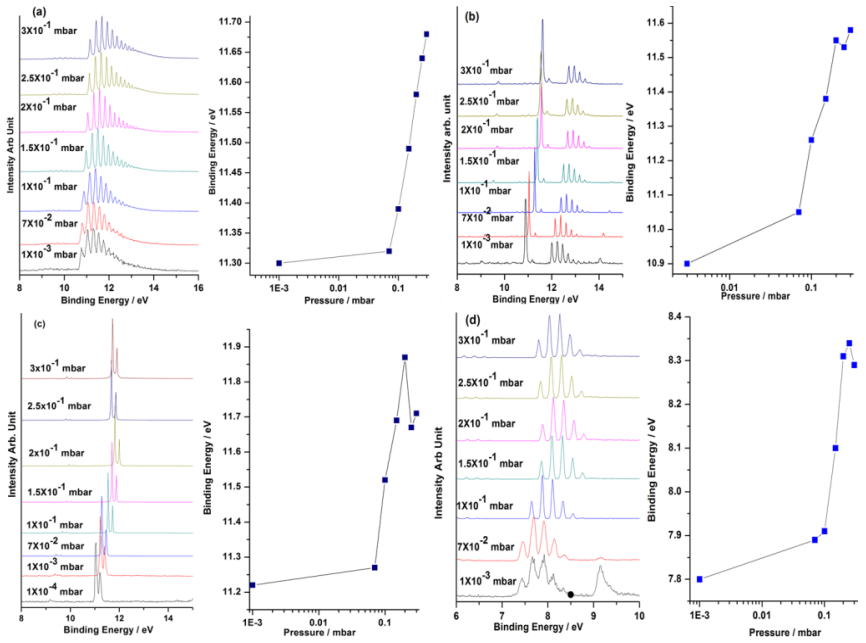

Figure 5.2: Pressure dependent gas phase vibrational spectra of (a) H_2, (b) N_2, (c) Ar, and (d) O_2. Binding energy changes observed for the highest intensity feature is plotted in a1 to d1 panels. All spectra are recorded at 298 K.

An important difference between Figure 5.2 and 5.3 is that there is no change in BE value of gas-phase features at increasing pressure in the presence of solid surfaces in the latter (N_2) case. This is attributed to the heat-sink nature of solid surfaces. Intermolecular or interatomic interaction increases in the viscous state, which should lead to a possible increase in temperature in the viscous state. However, this is totally avoided in the presence of a solid surface, due to effective heat dissipation in the bulk solids. In other words, Joule-Thompson effect occurs in the presence of a solid surface. Our efforts to measure the temperature change did not show any change. This is attributed to the bulk nature of solid and hence ultra-sophisticated temperature measuring device, particularly on the top-surface, is required. With our current sample holders, the temperature changes are measured from the bottom surface and it is not expected to show any significant change. It is also to be noted that the VB of Ag or Si decreases with increasing pressure; at 0.4 mbar and above, no VB feature of solid surfaces are observed. This is attributed to the increasing inelastic scattering of photoelectrons with gas-phase molecules, and hence attenuation in intensity was observed. This factor limits the maximum pressure that can be employed to detect low energy electrons with He I

photons. Another factor is the difference in work function of silver (4.26-4.74 eV) compared to silicon (4.60-4.85 eV). The difference in the energy of the vibrational feature of nitrogen on silver and silicon surface is in decent correlation with that of difference in the work function between them. Even though N_2 and Ar was used in Figure 5.3b and 5.3c, but they show the same shift on Si entirely reflect the work function of Si surface.

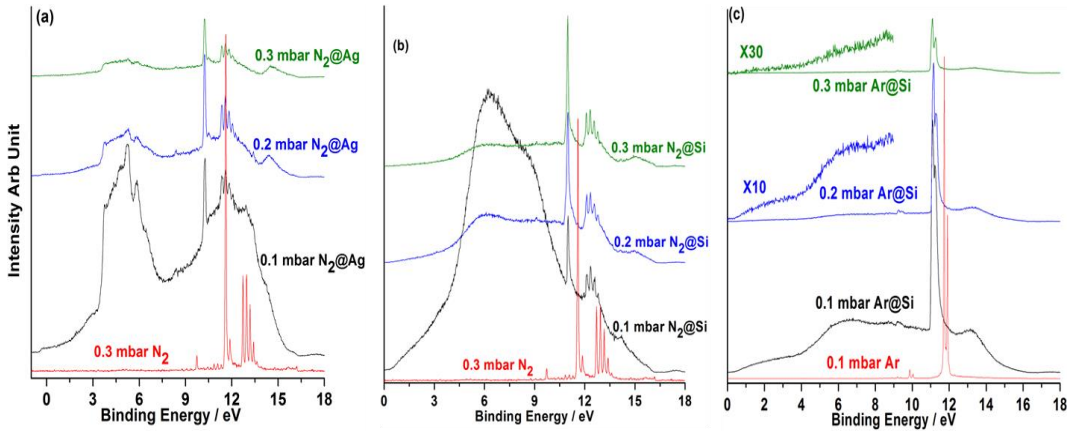

Figure 5.3: (a) and (b) N_2 spectrum with varying the pressure from 0.1 mbar to 0.3 mbar at room temperature on Ag and Si surface, respectively. (c) Ar spectrum recorded on Si at increasing pressure from 0.1 to 0.3 mbar at room temperature. Due to Ar accumulation on surface layers, Si-features intensity was observed to be low at high pressures and multiplied spectra are shown. Reference spectrum of N_2 and Ar is given in red color at the bottom of the panels.

5.5 Effect of metal Surface Nature on the Binding Energy of Gas Phase Spectrum

Adsorption of N_2 and Ar on Co, Ni, Si, Au and Ag surfaces has been evaluated by the NAP-UPS at 0.1 mbar gas pressure at 298 K. Figure 5.4 (a) shows the N_2 gas phase spectra on Co metal and *in-situ* generated Co_3O_4 oxide surfaces. The wine red color spectrum in Figure 5.4 (a) represents the valence band spectrum of Co metal recorded at ultra high vacuum.[33] Gas-phase spectrum of nitrogen at 0.1 mbar (red trace) is given for reference. There is a small shift in the BE from 11.30 to 11.15 eV of the gas phase spectrum of N_2 on Co metal surface (blue color) compared to pure N_2 gas phase spectrum (red color). The FWHM of N_2 feature increased from 0.04 in reference gas-phase spectrum to 0.11 eV on Co metal surface. N_2 is an inert gas with very low sticking coefficient and expected to have very poor interaction with Co; however, while dosing N_2 gas on Co metal surface, a huge decrease in the Fermi level

density of states of Co metal (while retaining the feature around 6 eV in both spectra), shift in the BE of the gas phase features, and increase in the FWHM of N_2 features indicates that there is, indeed, interaction between N_2 molecules and the Co-metal surface. It is already explained in section 1 that when the electron is added into the antibonding orbital, there will be a negative shift in the BE of the gas phase spectrum. A huge decrease in the ratio of E_F to 6 eV feature while dosing N_2 on Co-metal, compared to virgin Co, underscores the charge transfer from Co-metal to nitrogen molecules. It is well known that N_2 is the most stable homonuclear diatomic molecule with the bonding orbitals fully filled with a bond order of 3 (see Figure 5.1c), and antibonding orbitals are empty. Charge transfer from Co to N_2 molecules resulting in the negative shift in the BE of the spectra as well as an increase in the FWHM of all vibrational features of nitrogen molecules. This suggest a possibility of nitrogen activation on Co-metal surface and it is worth exploring further towards various reactions, including ammonia formation. Our efforts to identify the N-atoms on the surface did not yield any meaningful results, possibly due to low N-coverage and large probing depth of XPS. Careful experiments at higher pressures should be performed. It is also worth to note the literature report on nitrogen activation on molecular cobalt complexes.[34]

To understand the influence of solid surface work function on the BE of the vibrational features of N_2 was measured on Co_3O_4 surfaces. Initially, we have oxidized the Co foil in the presence of O_2 at 1 mbar at 500 K. Co metal foil surface gets completely converted into Co_3O_4. In Figure 5.4a olive green color spectrum represent the valence band spectrum of Co_3O_4.[35] When N_2 gas is dosed on the Co_3O_4 surface the BE of the N_2 gas is shifted towards a lower BE side by 0.85 eV compared to Co metal surface. BE changes in N_2 vibrational features on Co-metal and Co_3O_4 is almost similar to work function changes from Co to Co_3O_4 (4.8, 6.3 eV respectively), which is around 0.74 eV. The secondary electron cut-off measures the change in work function in Figure 5.4 (a), which is in good correlation with the above changes. Unlike poorly resolved features of N_2 on Co, N_2 on Co_3O_4 shows well-resolved vibrational features, even though it is broadened. This indicates the gas-solid (N_2-Co_3O_4) interaction is poor under the present experimental conditions. We have also recorded the Ar gas features (Figure 5.4b) on the pure Co metal and Co_3O_4 surfaces. The photoionisation cross

section (σ) of Ar 3p, Co 3d and O 2p are 38.1, 4.3 and 10.63 Mb, respectively.[36] σ of Ar 3p is nearly an order of magnitude higher than Co. Expectedly, the intensity of Co and Co_3O_4 valence band intensity in Figure 5.4b is very low due to low σ of Co 3d. Due to significantly high σ of O 2p in Co_3O_4 valence band intensity is relatively high than pure Co. For comparison purposes, Co and Co_3O_4 spectra are multiplied 5 times. Very small shift (0.07 eV) is observed with the BE of Ar 3p spin-orbit doublet for Ar on Co-metal compared to reference gas-phase spectrum. However, when the gas spectrum is recorded on Co_3O_4, there is 0.6 eV shift is observed on the lower BE side. The shift in the Ar spectrum is lower than the N_2 gas due to the stronger interaction of N_2 than argon on Co metal surface. Another interesting observation is the decrease in the intensity ratio for Ar $3p_{3/2}$ to $3p_{1/2}$ features on Co-metal (2.05) and Co_3O_4 (1.71) surfaces. Like in the N_2-case, although E_F intensity decreases in the presence of 0.1 mbar Ar on Co, no charge transfer is possible from Co E_F level to the unoccupied orbitals of Ar 3d or Ar 4s, since they are very high in energy. However, the reason for increasing Ar $3p_{1/2}$ intensity on Co_3O_4-surface is not known. Further, FWHM of Ar features remains the same in reference spectrum and on Co and Co_3O_4, highlighting that there is hardly any chemical interaction between them. This is on the expected lines.

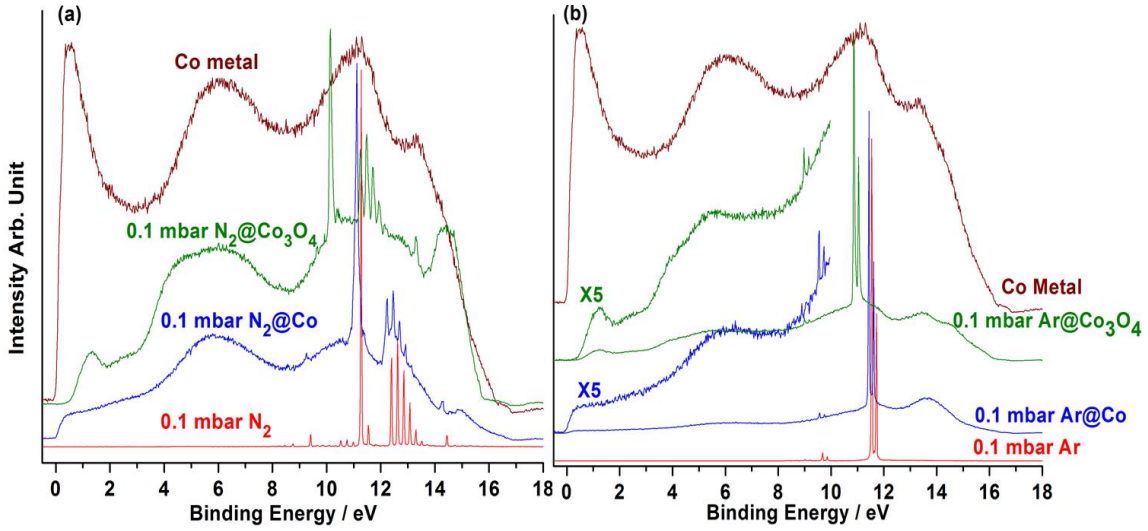

Figure 5.4: (a) N_2 gas phase spectra of pure N_2 (red color), on Co metal (blue color) and oxidized metal surface (Co_3O_4) are shown. (b) Ar gas phase spectrum recorded for pure argon (red color), on Co metal (blue color) and oxidized metal surface (Co_3O_4 olive color). Co valence band (wine red color) spectrum recorded at UHV is shown for reference in both panels.

Figure 5.5a and b show the Ar and N_2 spectrum recorded on Ni metal and NiO surfaces at 0.1 mbar pressure. Among the first row transition metals, many of them have high relevance to heterogeneous catalysis. As a representative of them, Ni and NiO are chosen for this particular study. How effectively the gas-solid interaction occurs between Ni and NiO solid surfaces and inert Ar and N_2 gases is the purpose of the present study. Figure 5.5a shows the spectrum recorded while dosing N_2 gas at 0.1 mbar pressure on Ni metal surface (blue color trace).[37] The red color trace shows the pure N_2 gas phase spectrum employed as reference and the valence band features of Ni-metal recorded at UHV is shown in wine red trace. When 0.1 mbar N_2 gas is dosed on the Ni metal surface, the N_2 spectrum shift towards lower BE side compared to reference N_2 spectrum from 11.25 to 10.80 eV as well as the FWHM also increased from 0.041 to 0.065 eV, respectively. Interestingly, for cobalt (Figure 5.4a) and nickel metals the BE shift of N_2 features, compared to pure N_2 gas, shift by 0.15 and 0.45 eV, respectively. Significantly large shift observed on Ni surface indicating that N_2 gas interacts with Ni stronger than the Co surface. However, well-resolved N_2 vibration features

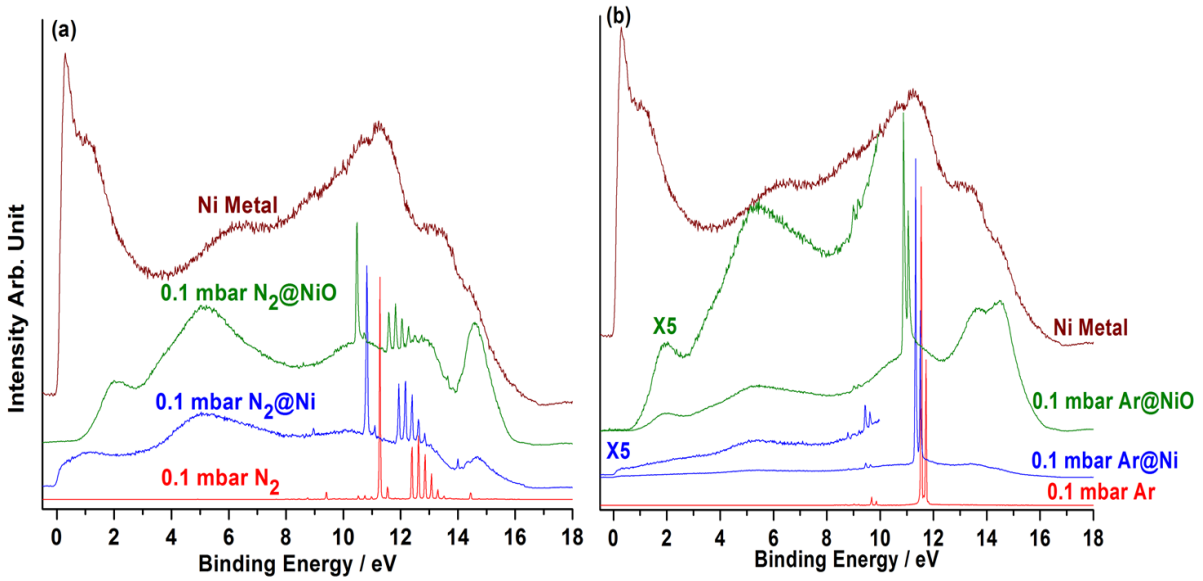

Figure 5.5: (a) The nitrogen gas phase spectrum of pure nitrogen (red color), on Ni metal (blue color) and oxidized metal surface (NiO olive color). (b) The argon gas phase spectrum of pure argon (red color), on metallic Ni (blue color) andoxidized metal surface (NiO olive color). Ni valence band (wine red color) spectrum recorded at UHV is given for reference in both panels in wine red color.

suggesting that there is no heterogeneity on the Ni- surface due to any N_2-dissociation. No report on nitrogen activation on Ni-compounds are found in the literature. N_2 is isoelectronic with CO molecule and interaction of CO with Ni metal has been studied in detail in the literature.[38] Therefore, the probable reason for the shift in the BE of the vibrational spectrum on the metal surface is likely due to charge transfer from metal to N_2 gas. Like Co-metal, Ni also shows large DOS at E_F, and the same decreases in the presence of N_2 again highlighting the charge transfer from Ni to N_2 molecules. Because Co and Ni have a different probability of charge transfer to N_2 molecules, the shift in vibrational spectra is also different. N_2 vibration spectrum shows a further shift towards lower BE side (olive color spectra in Fig 5.5a) on the NiO surface. The shift in the vibrational spectrum is around 0.3 eV which is similar to the change in ϕ when Ni metal is oxidized to NiO, which is also around 0.3 eV.

Figure 5.5b shows the spectra recorded while Ar gas was dosed on Ni and NiO surfaces. In this also the σ of Ar 3p and Ni 3d are 38.1 and 3.8 Mb,[36] respectively, and Ar exhibits an order of magnitude higher σ than Ni. Therefor the intensity of Ni and Ni valence band intensity in Figure 5.5b is very low. For comparision, five times multiplied spectra of Ni and NiO is shown. The Ar 3p atomic orbital features show the same trend as N_2 in shifting the BE position. Ar 3p levels shift towards lower BE side by 0.15 and 0.4 eV on Ni and NiO surfaces, respectively, compared to the reference Ar spectrum recorded for Ar at 0.1 mbar on Ni metal surface. The shift observed on Ni and NiO is in good correspondence with the change in ϕ (of Ni and NiO) around 0.4 eV. These results indicate that the shift in the BE of the gas phase features predominantly depends on the change in the ϕ of the material.

Figure 5.6a shows the spectra recorded while N_2 was dosed on the Si and SiO_2 surfaces. The wine red color trace shows the valence band of Si reference spectrum recorded at UHV, and the red color trace shows pure N_2 gas phase spectrum. When 0.1 mbar N_2 was dosed on the clean Si surface, a BE shift by 0.25 eV was observed on the lower BE side for N_2 features. It has been explained that this shift is observed due to interaction between Si and N_2. BE of N_2 features on Co, Ni and Si are observed to be 0.15, 0.45 and 0.25 eV, respectively. The dangling bond features intensity observed on virgin Si-surface (1-3.5 eV)[15] decreases in intensity while dosing N_2. This is clearly indicating the possibility of saturating

the dangling bonds by possible physisorption of nitrogen molecule on those sites. Any N_2 dissociation or chemisorption and N-atoms are ruled out, based on the sharp feature of gas-phase nitrogen observed on Si. Gold is considered as inactive and we explored for any possible weak interaction between gold surface and the most stable N_2 molecules.[39] We have recorded the N_2 gas phase spectrum on the Au surface (Figure 5.6b). While gold valence band features remain observed at the same BE, a BE shift of 0.5 eV was observed for N_2 features, compared to the reference N_2 spectrum. FWHM of N_2 vibrational features also remains the same as that of reference N_2 spectrum. This indicate that the shift in vibrational features depends on the nature of the surface. No change observed either with N_2 or Au features reiterates that the gold surface is totally inactive. Further, this also lends support to the different observations made in earlier results (Figures. 5.1-5.6a) for gas-solid interaction between reactive or not-so-reactive gas-phase molecules and different surfaces. To understand

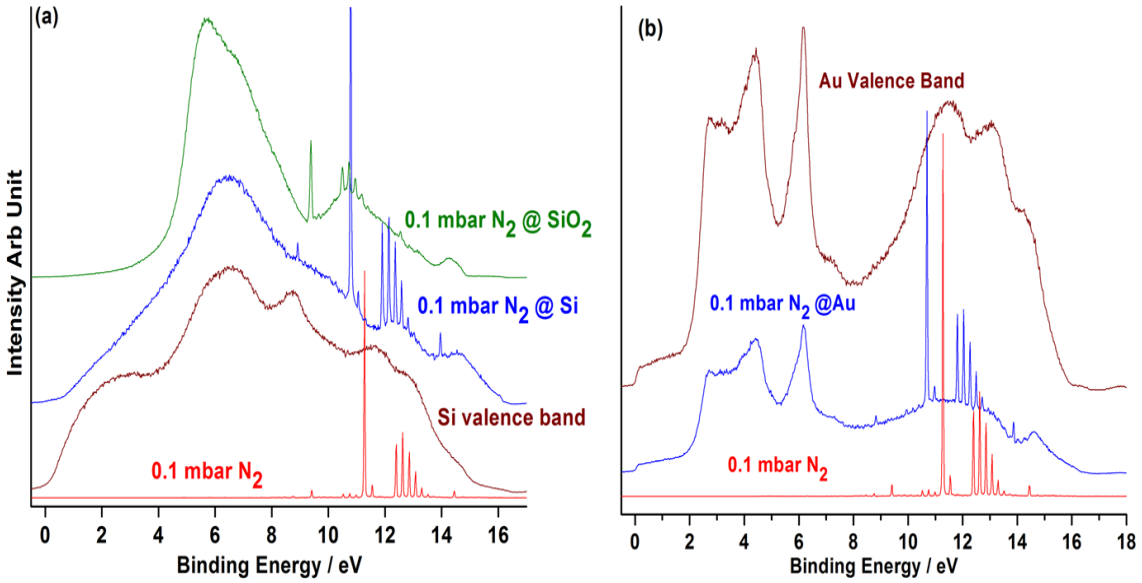

Figure 5.6: (a) The gas phase spectrum of pure nitrogen (red color), Si valence band (wine red color), N_2 on Si (blue color), and N_2 on SiO_2 surface (green). When Si was oxidized to SiO_2 the gas phase N_2 features also shift towards lower BE side by 1.4 eV which is equal to the change in work function. (b) The gas phase spectrum of pure nitrogen (red color), N_2 on Au metal (blue color), and Au valence band (wine red; recorded at UHV).

the effect of ϕ on the vibrational spectrum we have employed the silica surface (Si oxidized in situ to SiO_2; Figure 5.6a) and dosed the N_2 gas. It is observed that the N_2 vibrational feature

shifts to 9.35 eV from 10.75 eV. This shift is similar to the change in ϕ, when Si is oxidized to SiO_2. The ϕ change by 1.4 eV which is equal to the shift in the vibrational spectra observed by 1.43 eV. All these results indicate that the change in the energy position of vibrational features mainly depends on the ϕ changes of material.

We also studied the Ar interaction with silver as well as the gold surfaces, and the results are shown in Figure 5.7a and 5.7b, respectively. When 0.1 mbar Ar was dosed on Ag and Au (blue color spectra) surfaces, the gas phase Ar features shifted to lower BE side, as observed on other metal surfaces; however, the shift observed for Ni (0.15 eV) and Co (0.07 eV) (Figures. 5.4b and 5.5b) is smaller than that observed on Ag (0.88 eV) and Au (0.43 eV) surfaces. Surprisingly the FWHM of Ar 3p levels increased on both silver and gold surfaces. There was no significant increase in the FWHM of Ar 3p features on Ni and Co surfaces. The intensity ratio of $3p_{3/2}$ and $3p_{1/2}$ peak for Ar gas is also decreased on Au and Ag metal surfaces. However, a careful analysis of the data reveals that the splitting between spin-orbit components of Ar is still observed for both metal surfaces. This indicates the surface may have a significant amount of defect sites and argon on those sites appears at marginally different BEs. Deconvolution of Ar 3p features shown in the inset reveals several such features clearly. It is well known in the literature that Xe adsorbs on catalyst surfaces and Xe was used as probe atom to explore those defect sites.[30-32] Another important point to be noted is the insignificant change in the E_F and valence band features of Au and Ag in the presence of 0.1 mbar Ar, which is in contrast to Ni and Co. Although the E_F and VB feature decreased overall in intensity at 0.1 mbar Ar, which is attributed to high pressure, and the ratio of E_F to main VB remains the same. This reiterates that there is no possible charge transfer from Ag or Au surface to Ar atoms and the gas-solid surface interaction between them seems to be minimum or negligible.

In the next experiment, the silver surface is oxidized at 0.3 mbar O_2 pressure at 450 K; however, the complete oxidation of Ag to Ag_2O is not observed. In our earlier work on exploring the reasons for superior catalytic activity of silver surfaces for epoxidation, $Ag+O_2$ interaction was found to be critical. Between 390 and 450 K, $Ag+O_2$ shows different nature and the same surface is reproduced (O_2 on Ag at 450 K) and evaluated for modified silver

surfaces due to oxygen diffusion into the subsurfaces of silver. The modified Ag surface has a different character with contributions from electrophilic and nucleophilic oxygen sites along with subsurface coverage of oxygen. More details about the surface preparation is available in ref. 22. When the argon is dosed on the mildly oxidized silver surface (olive green color; Figure 5.7a) the Ar 3p levels shifts towards lower BE side by 0.5 eV which is equal to the change in the work function of Ag and AgO, which is also around 0.5 eV. However, surprisingly the intensity of $3p_{1/2}$ increased and appeared to be more than that of $3p_{3/2}$ peak intensity. It is to be underscored that the mildly oxidized Ag surface still retains a large amount of metallic silver and difficult to oxidize completely to AgO under the operative conditions of NAPPES. Likely that there are Ag and oxidized Ag[22] islands are present on the surface, and they lead to two sets of spin-orbit doublets of Ar. In addition weakly adsorbed Ar on silver surface also broadens the Ar 3p shallow levels. Deconvolution procedure applied shows four sets of Ar present on the surface.

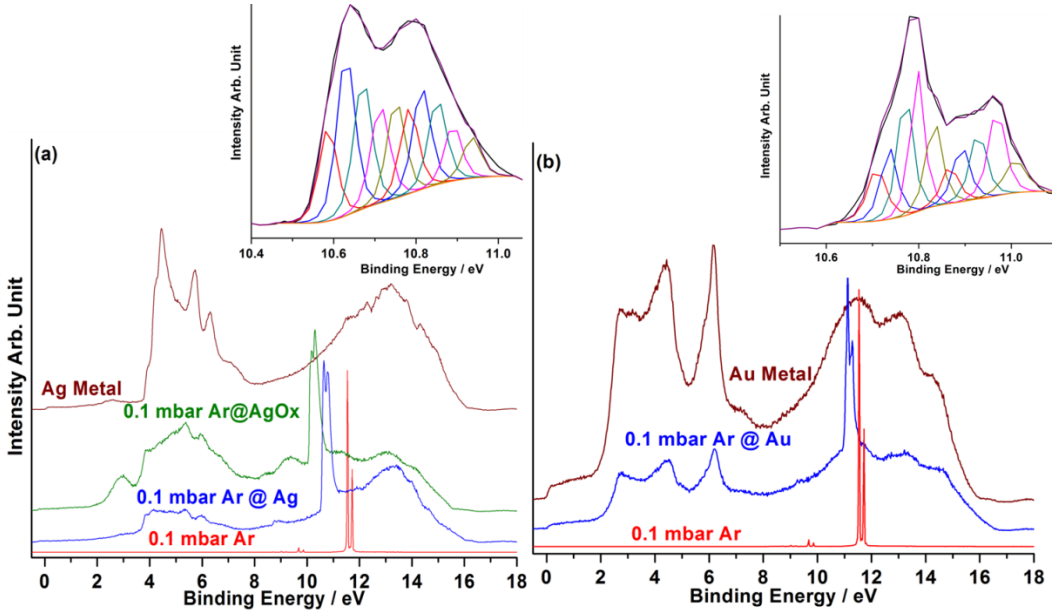

Figure 5.7: (a) The gas phase spectrum pure argon (red color), Ag VB recorded at UHV, Ar on Ag metal (blue color) and Ar on mildly oxidized Ag surfaces(olive color) (b) The gas phase spectrum of pure argon (red color), Au valence band recorded at UHV (wine color) and Ar on Au metal (blue color). Inset shows the deconvolution of Ar 3p observed on Ag and Au surfaces.

To confirm the influence of the surface and surface potential on the BE of gas phase spectra, we deliberately applied a bias on the silver surface in the presence of 0.1 mbar N_2 gas and recorded the NAPUPS spectra. The data is shown in Figure 5.8. The black color trace shown is for the N_2 (0.1 mbar) on Ag surface at zero bias. When -1 V is applied to the silver surface, expectedly, Ag valence band was observed to be shifted by 1 eV on the lower BE energy side. The gas phase N_2 spectrum is also shifted 1 eV towards lower BE side, even though N_2 molecules are present in the gas phase. This demonstrates the surface potential fully influences the gas-phase molecules that are in proximity to the Ag surface. An important advantage of UVPES is its high resolution, compared to the core level XPS; even a minor change in the nature of surface by 20 meV can be detected easily with the gas-phase features.

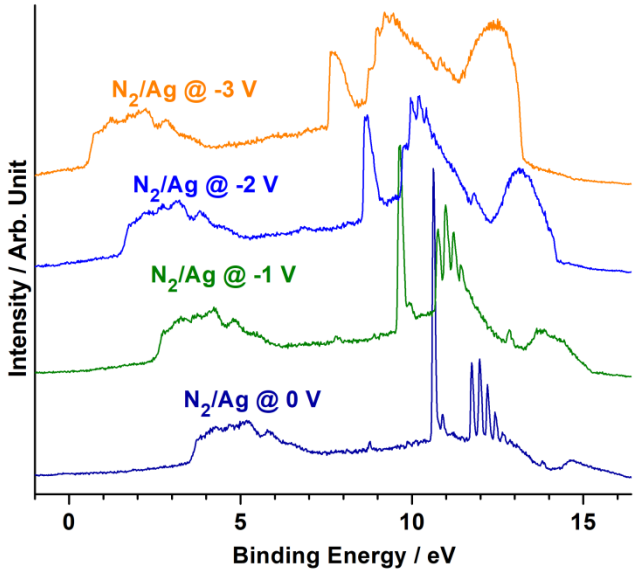

Figure 5.8: Effect of externally applied bias on the N_2 gas phase spectrum on the Ag surface. The black color spectrum shows without applying bias. Whereas the red, green and purple traces are recorded at -1, -2 and -3 volts, respectively. The observed shift in the spectrum is equal to the applied bias.

Any changes that occur on the surface due to gas-solid interaction can be detected and profiled under reaction conditions; this aspect has been documented by our earlier works.[15,19-23] -2 and -3 V was applied on the Ag surface and recorded the spectrum; in this case also Ag valence band and N_2 gas phase features are shifted by 2 and 3 eV on the lower BE side. These findings reiterate that the gas phase vibrational features can be employed to detect the change

in surface potential of any solid surfaces. One more point observed is that with increasing applied voltage, the FWHM of gas-phase features is also increasing, while solid surface features are retained without any change in FWHM. A careful analysis of the spectral features of N_2 reveals a steep rise in the intensity and a large peak asymmetry observed on the higher BE side. This hints a possibility of N_2 molecules experiencing a graded potential with increasing distance from the surface. This finding needs to be verified with other corroborating measurements.

5.6 Conclusion

An attempt has been made to understand the gas phase vibrational spectra and their electronic configuration by the UV photoelectron spectroscopy under the near ambient pressure conditions. Viscous state associated with gas-phase molecules around 0.1 mbar was established and a definite change in the BE trend was observed. Irrespective of the nature of reactive, not-so-reactive or noble gas, BE trend with pressure remains the same, hinting the intermolecular or interatomic interactions increases in the viscous state. Vibrational features associated with gas-phase molecules are sensitive enough to probe even the minor changes occurring on the solid surfaces. The interaction between reactive and not-so-reactive gas molecules/atoms with different solid surfaces are explored with NAPUPS. Several interesting conclusions were derived and some of them potentially interesting and worth studying further. N_2 on Co-surface shows significant charge transfer from Co to nitrogen molecules at room temperature and possible N_2 dissociation is expected. However, the same is not true with Ni and Co_3O_4 surfaces. Molecular nitrogen adsorbed on surface dangling bonds on silicon surfaces. Diffusion of oxygen into the subsurfaces of silver was identified through Ar-Ag interaction in NAPUPS. Some of these interactions are very minor in terms of energy/nature; however, they can be identified by the shift in vibrational features of probing molecules due to the high sensitivy of NAPUPS. In general, the present set of experiments indicate that the BE position of these gas phase vibrational spectra depends on the electronic nature of the surface and the gas-solid interaction. These results reveal that, not only the surface is influenced by the interacting gas molecule, in turn the gas molecules senses the changes and reflects the same in the resulting spectra. The ϕ is the key electronic property of a surface

which mainly depends on the geometry and electronic nature of the surface. It is necessary to measure the ϕ under realistic conditions or close to that; NAPUPS is expected to play a major role in such studies and can help to map out the changes in ϕ as a function of reaction conditions. The NAPUPS can also be helpful to overcome the limitation of traditional methods employing high vacuum, for the ϕ determination. Present studies are very relevant to the surface dependent application like sensors, heterogenous catalysis, semiconductor, etc. Even though inert gases are employed for the present investigations, however, surprisingly they are also affected by the surface nature which is quite interesting. Understanding of the effect of surface nature on the interacting molecule can be quite intersting phenomena which can lead to developing to revolutionary material for the surface relevant application.

5.7 References

1. Bogumil, K.; Orphal, J.; Homann, T.; Voigt, S.; Spietz, P.; Fleischmann, O.; Vogel, A.; Hartmann, M.; Kromminga, H.; Bovensmann, H., Measurements of molecular absorption spectra with the SCIAMACHY pre-flight model: instrument characterization and reference data for atmospheric remote-sensing in the 230–2380 nm region. *J. Photochem. Photobio.* **2003,** *157,* 167-184
2. Carnovale, F.; Peel, J. B.; Rothwell, R. G., Photoelectron spectroscopy of the oxygen dimer and clusters. *J. Mass Spectrom.* **1991,** *26,* 201-207.
3. Imbihl, R.; Ertl, G., Oscillatory kinetics in heterogeneous catalysis. *Chem. Rev.* **1995,** *95,* 697-733.
4. Gopinath, C. S.; Roy, K.; Nagarajan, S., Can We Shift and/or Broaden the Catalysis Regime towards Ambient Temperature ? *ChemCatChem* **2015**, *7*, 588-594.
5. Velu, S.; Suzuki, K.; Vijayaraj, M.; Barman, S.; Gopinath, C. S., In situ XPS investigations of $Cu_{1-x}Ni_xZnAl$-mixed metal oxide catalysts used in the oxidative steam reforming of bio-ethanol. *Appl. Catal. B* **2005,** *55,* 287-299.
6. Mathew, T.; Vijayaraj, M.; Pai, S.; Tope, B. B.; Hegde, S. G.; Rao, B.; Gopinath, C. S., A mechanistic approach to phenol methylation on $Cu_{1-x}Co_xFe_2O_4$: FTIR study. *J. Catal.* **2004,** *227,* 175-185.
7. Roy, K.; Jain, R.; Gopinath, C. S., Sustainable and Near Ambient DeNOx Under Lean Burn Conditions: A Revisit to NO Reduction on Virgin and Modified Pd (111) Surfaces. *ACS Catal.* **2014**, *4*, 1801-1811.

8. Eichelbaum, M.; Hävecker, M.; Heine, C.; Wernbacher, A. M.; Rosowski, F.; Trunschke, A.; Schlögl, R., The electronic factor in alkane oxidation catalysis. *Angew. Chem. Inter. Ed.* 2015, 54, 2922-2926

9. Haber, J.; Witko, M., Oxidation catalysis—electronic theory revisited. *J. Catal.* **2003,** *216*, 416-424.

10. Vol′kenshteĭn, F. F., *The electronic theory of catalysis on semiconductors*. Macmillan: **1963**

11. Wittstock, A.; Zielasek, V.; Biener, J.; Friend, C.; Bäumer, M., Nanoporous gold catalysts for selective gas-phase oxidative coupling of methanol at low temperature. *Science* **2010,** *327*, 319-322.

12. Melvin, A. A.; Illath, K.; Das, T.; Raja, T.; Bhattacharyya, S.; Gopinath, C. S., M–Au/TiO2 (M= Ag, Pd, and Pt) nanophotocatalyst for overall solar water splitting: role of interfaces. *Nanoscale* 2015, 7, 13477-13488

13. Scharber, M. C.; Mühlbacher, D.; Koppe, M.; Denk, P.; Waldauf, C.; Heeger, A. J.; Brabec, C. J., Design rules for donors in bulk-heterojunction solar cells—Towards 10% energy-conversion efficiency. *Adv. Mater.* **2006,** *18*, 789-794.

14. Grubbs, M. E.; Deal, M.; Nishi, Y.; Clemens, B. M., The effect of oxygen on the work function of tungsten gate electrodes in MOS devices. *IEEE. Electr. Device. L.* **2009,** *30*, 925-927.

15. Ghosalya, M. K.; Jain, R.; Reddy, K. P.; Gopinath, C. S., Silicon Oxidation by NAPPES: From Dangling Bonds to Oxygen Islands to 2D SiOx Layer to the Onset of Bulk SiO_2 Formation. *J. Phys. Chem. C* **2018,** *122*, 4331-4338.

16. Kumar, A.; Jaiswal, M.; Kanjilal, D.; Joshi, R. K.; Mohanty, T., Fermi level shifting of TiO_2 nanostructures during dense electronic excitation. *Appl. Phys. Lett.* **2011**, *99*, 013109

17. Filleter, T.; Emtsev, K.; Seyller, T.; Bennewitz, R., Local work function measurements of epitaxial graphene. *Appl. Phys. Lett.* **2008,** *93*, 133117

18. Kolekar, S. K.; Dubey, A.; Date, K. S.; Datar, S.; Gopinath, C. S., An attempt to correlate surface physics with chemical properties: molecular beam and Kelvin probe investigations of $Ce_{1-x}Zr_xO_2$ thin films. *Phys. Chem. Chem. Phys.* **2016,** *18*, 27594-27602.

19. Jain, R.; Dubey, A.; Ghosalya, M. K.; Gopinath, C. S., Gas–solid interaction of H_2–$Ce_{0.95}Zr_{0.05}O_2$: new insights into surface participation in heterogeneous catalysis. *Catal. Sci. Tech.* **2016**, *6*, 1746-1756

20. Jain, R.; Gnanakumar, E. S.; Gopinath, C. S., Mechanistic Aspects of Wet and Dry CO Oxidation on Co_3O_4 Nanorod Surfaces: A NAP-UPS Study. *ACS Omega* **2017**, *2*, 828-834.

21. Roy, K.; Gopinath, C. S., UV photoelectron spectroscopy at near ambient pressures: Mapping valence band electronic structure changes from Cu to CuO. *Anal. Chem.* **2014**, *86*, 3683-3687

22. Ghosalya, M. K.; Reddy, K. P.; Jain, R.; Roy, K.; Gopinath, C. S., Subtle interaction between Ag and O_2 : a near ambient pressure UV photoelectron spectroscopy (NAP-UPS) investigations. *J. Chem. Sci.* **2018**, *130*, Art. No. 30.

23. Roy, K.; Vinod, C.; Gopinath, C. S., Design and performance aspects of a custom-built ambient pressure photoelectron spectrometer toward bridging the pressure gap: Oxidation of Cu, Ag, and Au surfaces at 1 mbar O_2 pressure. *J. Phys. Chem. C* **2013,** *117*, 4717-4726.

24. Banwell, C. N.; McCash, E. M., *Fundamentals of molecular spectroscopy*. McGraw-Hill New York: **1994**; *851*

25. Murakami, K.; Fukata, N.; Sasaki, S.; Ishioka, K.; Kitajima, M.; Fujimura, S.; Kikuchi, J.; Haneda, H., Hydrogen molecules in crystalline silicon treated with atomic hydrogen. *Phys. Rev. Lett.* **1996,** *77*, 3161.

26. Weber, A.; McGinnis, E. A., the Raman spectrum of gaseous oxygen. *J. Mol. Spectrosc.* **1960,** *4*, 195-200.

27. Chaquin, P.; Canac, Y.; Lepetit, C.; Zargarian, D.; Chauvin, R., Estimating local bonding/antibonding character of canonical molecular orbitals from their energy derivatives. The case of coordinating lone pair orbitals. *Int. J. Quantum Chem.* **2016**, *116*, 1285-1295.

28. Guevremont, J. M.; Sheldon, S.; Zaera, F., Design and characterization of collimated effusive gas beam sources: Effect of source dimensions and backing pressure on total flow and beam profile. *Rev. Sci. Instrum.* **2000,** *71*, 3869-3881.

29. Lesiak, B.; Kosinski, A.; Jablonski, A.; Sulyok, A.; Gergely, G.; Tóth, J.; Varga, D., Influence of recoil effect and surface excitations on the inelastic mean free paths of electrons in polymers. *Acta Phys. Pol. A* **2006,** *109*, 789-800.

30. Guevremont, J.; Strongin, D.; Schoonen, M., Photoemission of adsorbed Xenon, X-ray photoelectron spectroscopy, and temperature-programmed desorption studies of H_2O on FeS_2 (100). *Langmuir* **1998,** *14*, 1361-1366.

31. Guo, H.; Zaera, F., Xenon as a probe for minority sites on solid surfaces. *Nat. Mater.* **2006,** *5*, 489.

32. Ito, T.; Fraissard, J., ^{129}Xe NMR study of xenon adsorbed on Y zeolites, *J. Chem. Phys.* **1998**, *76*, 5225-5229.

33. Reddy, K. P.; Jain, R.; Ghosalya, M. K.; Gopinath, C. S., Metallic Cobalt to Spinel Co_3O_4 Electronic Structure Evolution by Near-Ambient Pressure Photoelectron Spectroscopy. *J. Phys. Chem. C* **2017,** *121*, 21472-21481.

34. Del Castillo, T. J.; Thompson, N. B.; Suess, D. L.; Ung, G.; Peters, J. C., Evaluating molecular cobalt complexes for the conversion of N_2 to NH_3. *Inorg. Chem.* **2015**, *54*, 9256-9262.

35. Jain, R.; Reddy, K. P.; Ghosalya, M. K.; Gopinath, C. S., Water-Mediated Deactivation of Co_3O_4 Naonrods Catalyst for CO Oxidation and Resumption of Activity at and Above 373 K: Electronic Structural Aspects by NAPPES. *J. Phys. Chem. C* **2017,** *121*, 20296-20305.

36. Yeh, J. J.; Lindau, I., Atomic subshell photoionization cross sections and asymmetry parameters: 1< Z<103. *Atom. Data Nucl. Data. Tables* **1985**, *32*, 1-155.

37. Mårtensson, H.; Nilsson, P., Investigation of the electronic structure of Ni by angle-resolved uv photoelectron spectroscopy. *Phys. Rev. B* **1984,** *30*, 3047.

38. Hüfner, S., *Photoelectron spectroscopy: principles and applications*. Springer Verlag, Berlin, 3rd Ed., **2003,** 210-345.

39. A. C. Sunilsekhar, K. Sivaranjani, C. S. Gopinath, C. P. Vinod, A simple one pot synthesis of nano gold – mesoporous silica and its oxidation catalysis, *Catal. Today*, **2012**, *198*, 92-97.

Chapter 6

Conclusion and Future Outlook

In this dissertation, we have studied the gas-solid interaction under operando condition by using NAPPES. The gas-solid interaction is complex in nature; however, these interactions play pivotal roles in various applications like, heterogeneous catalysis, sensors, electrochemistry, and semiconductor. Often there is no straight correlation between reactivity, selectivity and structure of catalyst; however, reactivity and selectivity also controlled by other parameter like, changes in electronic nature of catalyst surface under the operando condition, the surface restructuring due to the adsorption of reactant, the competitive adsorption between various adsorbing reactants etc. Hence, there are various factors which are needed to be explored under operating conditions. To understand the gas-solid interactions, several surface characterization techniques have been successfully developed. Among them NAPPES is comparatively new and rapidly growing technique which has lot of potential to explore the electronic nature of material under operando conditions. This technique can be operated at elevated pressures and temperatures. In this thesis work, all experiments were carried out in lab-based NAPPES available at CSIR-National Chemical Laboratory, Pune, India. The detail of this system is explained in chapter 2.

In chapter 3a we attempted to address a fundamental question of ethylene epoxidation. Why only silver shows high activity and selectivity for epoxidation product in a particular temperature (420 to 500 K) window? Ag-O_2 interaction is studied by NAP-XPS and NAP-UPS under technically relevant conditions. Three different types of silver-oxygen interaction regimes have been identified between 300 and 500 K, namely, (a) 300-390 K, oxygen chemisorption on Ag surface; (b) between 390 and 450 K, O-diffusion into the subsurface layers occurs and lead to subtle surface modification; and (c) >450 K for metastable oxide formation; the later two regimes are dynamic in nature. A significant change in the ϕ of Ag in the presence of O_2 was observed between 390 and 450 K. The diffusion of O- atom in subsurface region is the key step for high selectivity for ethylene epoxidation rather than combustion. Subsurface oxygen makes the Ag surface to be marginally electron deficient, which alters the initially repulsive interaction to an attractive one between ethylene and Ag surface. The oxygen present on the electron deficient Ag surface may act as electrophilic and

it can get inserted into ethylene to epoxide. Further increasing the temperature more than 450 K the leads to increase in ϕ and oxygen coverage (θo). The high coverage and more positive charge on surface are responsible for the complete combustion of ethylene to CO_2. What is important in this work is the observation of silver remains in the metallic state, in spite of oxygen interaction with it. Although a large change in ϕ of Ag surface was observed under NAPPES conditions, large metallic character reiterates that the gas-solid O_2-Ag interaction is subtle, and that too it occurs under operando conditions. Generation of space charge layer alters the activity favorably towards epoxidation. This emphasizes *in situ* and operando investigations are essential to understand the nature of active form of the catalyst. Indeed, it is worth investigating many such reactions to understand the active form of catalyst, which will help to develop more active catalyst. In chapter 3b, we have studied the active phase of Fe/Al_2O_3 for oxidative dehydrogenation (ODH) of butane to 1, 3- butadiene. It is important to develop the highly active and selective catalyst for the ODH of butane to 1, 3-butadiene reaction. We have synthesized the Fe_2O_3–based catalyst5% Fe_2O_3/ Al_2O_3 shows the highest selectivity between 723 to 773 K and 5% Fe_2O_3/ Nb_2O_5 shows the least activity and selectivity to 1,3-butadiene. The NAPPES studies of both catalysts indicate that there is no interaction between Fe catalyst and Nb_2O_5. Whereas, Fe is reduced to Fe^{+2} state on Al_2O_3 support, and there is a possibility of iron carbide formation is indicated. These result confirmed that Fe^{+2} is the active species for high selectivity for 1,3- butadiene which is stabilized by the Al_2O_3 support.

In chapter 4, we proposed a mechanistic model for Si oxidation from initial adsorption of molecular oxygen on Si surface towards the bulk SiO_2 formation. The Si-O_2 interactions are important in semiconductor as well as in catalysis. For Si semiconductor, controlling the thickness and fabrication of defect free homogeneous SiO_2 layer on Si substrate is still a challenging task. Therefore, a mechanistic understanding is required about the kinetics of Si oxidation from initial adsorbed oxygen to bulk SiO_2 formation. We have carried out the *in situ* Si oxidation up to 0.5 mbar from RT to 900 K and observed the changes in electronic structure. It has been observed that the initial molecular oxygen adsorption as well as dissociation to atomic oxygen takes place on the dangling bond site at 500 K. Up to 500 K,

the oxidation of Si surface is localized and limited to initial dissociation sites. When the temperature is increased up to 600 K the Si surface is homogeneously oxidized to 2D SiOx layer. This 2D layer acts as a protective layer for the inner Si-layers and prevents them from oxidation up to 800 K. However, more severe conditions, up to 900 K at 0.5 mbar O_2 pressure, initiate the onset of bulk oxidation. There is a surface gradation in the oxidized silicon species was observed from top to the bulk layers from highly oxidized to elemental silicon, respectively. More severe pressure and temperature are expected to increase the oxidation extent and follow the same trend reported in this thesis. The present studies show that initial few layer of Si is oxidized at comparatively low temperature and low pressure conditions but bulk Si oxidation requires harsh temperature and pressure conditions. This studies also suggest that the initial oxidation of Si surface, can be controlled by the controlling the number of dangling bond site on Si surface. Si ϕ very much influences the electronic state of gas-phase molecules. Changes observed in the ϕ of Si, due to chemical/ electronic interaction with gas phase molecules, in turn affects the electronic state of interacting gas molecules. To the best of our knowledge no such information has been obtained or published in the literature. Such dynamic changes are possible under catalysis conditions and it is worth exploring in detail for different systems.

Chapter 5 investigated the gas phase vibrational spectra of reactive (H_2 and O_2) and less reactive gases (N_2 and Ar) with different surfaces by NAPUPS up to 0.3 mbar at room temperature. In chapter 3 and 4 the effect of reactive gas on the surface has been studied; however, in this chapter we have studied the effect of catalyst surface on the electronic-vibrational spectra of gas molecule which are close to surface but not adsorbed. For this study N_2, this is considered as stable molecule and non-reactive noble Ar gas are chosen. Vibrational features associated with gas-phase molecules are sensitive enough to probe even the minor changes occurring on the solid surfaces. N_2 on Co-surface shows significant charge transfer from Co to nitrogen molecules at room temperature and possible N_2 dissociation is expected. However, the same is not true with Ni and Co_3O_4 surfaces. Molecular nitrogen adsorbed on surface dangling bonds on silicon surfaces. Diffusion of oxygen into the subsurfaces of silver was identified through Ar-Ag interaction in NAPUPS. Some of these

interactions are very minor in terms of energy/nature; however, they can be identified by the shift in vibrational features of probing molecules due to the high sensitivy of NAPUPS. In general, the present set of experiments indicate that the BE position of these gas phase vibrational spectra depends on the electronic nature of the surface and the gas-solid interaction. These results reveal that, not only the surface is influenced by the interacting gas molecule, in turn the gas molecules senses the changes and reflects the same in the resulting spectra. The ϕ is the key electronic property of a surface which mainly depends on the geometry and electronic nature of the surface. It is necessary to measure the ϕ under realistic conditions or close to that; NAPUPS is expected to play a major role in such studies and can help to map out the changes in ϕ as a function of reaction conditions.

In this thesis, we have demonstrated the direct relevance of NAPPES techniques to catalysis applications and electronic structure evolution of solid surface. Electronic structure evolution of solid surfaces as a function of reaction conditions is possible. This would help to identify the "real active phase" of catalyst under working conditions. Present studies are also relevant to many surface-dependent applications, such as heterogeneous catalysis, electrochemistry, nanomaterials, sensors. Particularly, 2D layered materials can be explored for change in work function, nature of charge transfer etc. Many demanding reactions, such as water splitting, nitrogen/CO_2/CH_4 activation could be explored in detail.